Liquid Water Dynamics in a Model Polymer Electrolyte Fuel Cell Flow Channel

by

Chris Miller
Bachelors of Engineering, University of Victoria, 2007

A Thesis Submitted in Partial Fulfillment
of the Requirements for the Degree of

MASC

in the Department of Mechanical Engineering

© Chris Miller, 2009
University of Victoria

All rights reserved. This thesis may not be reproduced in whole or in part, by photocopy or other means, without the permission of the author.

Supervisory Committee

Liquid Water Dynamics in a Model Polymer Electrolyte Fuel Cell Flow Channel

by

Chris Miller
Bachelors of Engineering, University of Victoria, 2007

Supervisory Committee

Dr. Ned Djilali, Department of Mechanical Engineering
Supervisor

Dr. Peter Oshkai, Department of Mechanical Engineering
Departmental Member

Dr. Sadik Dost, Department of Mechanical Engineering
Departmental Member

Abstract

Supervisory Committee

Dr. Ned Djilali, Department of Mechanical Engineering
Supervisor

Dr. Peter Oshkai, Department of Mechanical Engineering
Departmental Member

Dr. Sadik Dost, Department of Mechanical Engineering
Departmental Member

Water management in a polymer electrolyte fuel cell is a critical issue in ensuring high cell performance. The water production, due to both electro-osmotic drag and the chemical reaction, in the cathode side of the fuel cell leads to liquid water formation in the gas diffusion layer and the reactant flow channel. If this water is allowed to accumulate in the fuel cell, the transport of reactants to the membrane assembly will be inhibited and cell performance will suffer. In order to maximize the potential performance of a fuel cell, understanding of the liquid water dynamics is required, and a two-phase flow numerical model has been for this purpose. If an accurate numerical model can be created the development cycle for new flow channel designs can be accelerated.

The methodology adopted for the numerical simulation of dynamic two-phase flow is the volume of fluid (VOF) method. The major drawback of current VOF models is in the implementation of the three phase contact line. Current models use a constant static contact angle, which does not take into account real dynamics. This results in non-physical phenomena such as spherical and suspended droplets, instead of the

experimentally observed attached semi-spherical droplets with the trailing edge of the droplet forming a tail.

To remedy this shortcoming, the implementation of a dynamic contact angle relation is required. The relations used in the current work follows the Hoffman formulation where the dynamic contact angle is obtained as θ_D. A function of the capillary number, based on the contact line velocity, and of the equilibrium contact angle. The function was implemented within the commercial CFD framework of Fluent using user defined functions.

The dynamic contact angle models were able to better predict the droplet dynamics, providing elongated droplet profiles. The dynamic contact angle model was also able to provide more realistic pressure profiles down the channel length. Parametric studies show the dramatic effects that air speed and static contact angle have upon the droplet dynamics. It was also observed that water injection velocity had a relatively small effect on the model. The dynamic contact angle model was found to be consistent with experimental work conducted in our laboratory in which the spinning motion of the fluid within the water droplet was observed [7].

The improved physical representation achieved with the new model results in more reliable simulations and provides a good foundation for the numerical modeling of fuel cell flow channels.

Table of Contents

Nomenclature

Ca	Capillary number $Ca = \frac{(Vel)\mu}{\sigma}$
CFD	Computational fluid dynamics
GDL	Gas diffusion layer (provides the interface between the flow channel and the membrane/electrode assembly)
Hydrophobic	A surface that displays a contact angle of greater than 90˚
Hydrophilic	A surface that displays a contact angle of less than 90˚
PTFE	Polytetrafluoroethylene (produced by DuPont as Teflon)
RANS	Reynolds averaged Navier Stokes
Three phase contact line	The line where solid, liquid, and gas come into contact
U	The air velocity
V	The water injection velocity
VOF	Volume of fluid
θ_s	Static contact angle
θ_A	Advancing contact angle
θ_R	Receding contact angle
θ_D	Dynamic contact angle
α_q	Phase content variable (of phase q)
σ	Surface tension variable

List of Tables

List of Figures

Acknowledgements

The author wishes to acknowledge the diligent efforts of Dr. Ned Djilali during the development of the work presented in this thesis.

1 Introduction and Past Works

Water management in a polymer electrolyte fuel cell is a critical issue in ensuring high cell performance, and is coupled to a number of transport processes taking place during cell operation and reviewed in detail Djilali and Sui [1]:

- ionic and water transport, including electro-osmotic drag (EOD), in the polymer electrolyte membrane;
- heat, mass and charged species transfer coupled with reaction kinetics;
- multicomponent, two-phase flow with phase change in both porous electrodes and gas distribution microchannels.

Water transport and production, due to the combination of electro-osmotic drag, diffusion and the electro-chemical reaction, often lead to liquid water formation in the gas diffusion layer in the cathode side of the fuel cell. This is particularly the case at higher currents and/or relative humidity, when condensation and the resulting liquid water propagate from the GDL to the gas microchannels of the fuel cell [1], where discrete lumps of water can form as illustrated in figure 1. The resulting two-phase flow in the microchannels can result in transient pressure surges, non-uniform flow and current distributions, and an overall drop in performance.. This build up of excess water is referred to as flooding. The opposing design constraint comes from the performance characteristics of the membrane. The membrane electrode assembly is designed to operate within an optimal water saturation region. If the membrane has less than the optimal water saturation, its ionic conductivity decreases causing a loss in performance. To balance these competing requirements a system must be designed to remove just the excess liquid water, leaving enough water to hydrate the membrane assembly.

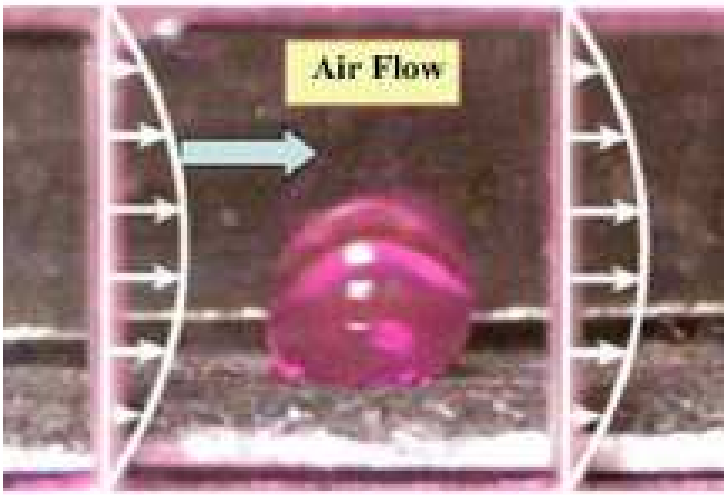

Figure 1: Water droplet in flow channel subjected to air flow [2]

Excess water presents itself in the flow channel on the porous gas diffusion layer. The volume of excess water flows through pores in the gas diffusion layer to form small droplets on the fibers of the gas diffusion layer at the preferential pore endpoints [3]. If these droplets are removed before they are able to grow and coalesce with neighboring droplets, then the flow channel runs a much lower risk of flooding.

Many strategies have been created to promote the removal of liquid water from the flow channels. The contact angle is the angle that the phase boundary makes in relation to the solid surface, and it plays a vital role in water dynamics. The use of hydrophobic coatings consisting of PTFE provides a higher contact angle on the water droplet, decreasing the area of the droplet at the diffusion media surface. This reduction in contact area on the gas diffusion layer leads to lower surface tension, which is the force that resists the droplet removal. The drawback of including PTFE coatings is the decrease in pore size in the gas diffusion layer, which inhibits reactant flow in the GDL, and an increase in the electrical contact resistance between the bipolar plates and the gas diffusion layer. Another strategy for increasing the removal of the water droplets comes

from adjusting the flow channel dimensions to optimize the droplet removal. The most commonly used methods for determining the optimal solution are based on increasing the flow velocity or reducing the channel height. These methods typically produce larger drag forces on the droplet and higher pressure drops in the channel. These methods of modifying water management performance are based mostly on experimental testing. Models for estimating the droplet dynamics using computational fluid dynamics are limited by their ability to resolve the physics seen in experimental set-ups. The main stumbling point in the CFD framework is in the application of the boundary conditions. The three-phase contact line presents an interesting numerical problem of a singularity arising from the no-slip boundary condition imposed at the moving contact line. The boundary condition results in an infinite tangential stress imposed by the fluid onto the solid surface due to the moving fluid and the stationary boundary condition. Another issue posed at the contact line is the tracking of the dynamic contact angle, which is dependant on the flow conditions around the droplet as well as the contact line motion.

One method of dealing with the singularity is to impose a slip condition at the boundary. For a review of the models used and their shortcoming refer to Shikhmurzaev 1993 [4]. A brief overview is given in table 1.

Table 1: Slip models examined by Shikhmurzaev

Name of the Author(s)	Year published	Model Basis	Drawbacks
Huh & Mason	1997	Physical model of the liquid-gas interface motion	Does not display the rolling motion described by Dussan(1979). Leads to integrable singularity at the solid boundary.
Durbin	1988	Slip due to limitation of the maximum shear stress density	Fair but not exact agreement with experiements
Baiocchi & Pukhhanchev	1990	Relative-velocity profile to minimize the entropy production	Fair but not exact agreement with experiements

In recent works modeling has followed two different avenues. The first avenue of research has been performed using commercial CFD simulations. One such work is that of Zhu et al [5,6]. In both papers they modeled a fuel cell flow channel in which water was introduced through discrete pores, and used an unsteady laminar volume of fluid (VOF) method with a continuum surface force to model the droplet dynamics. The contact angles were assumed to be 140 degrees on the substrate and 45 degrees on the surrounding three walls. The model used an 1x0.25mm flow area with an air velocity and water velocity of U=10m/s and V=1 m/s respectively. A film flow was observed; however, the large water injection rate is not representative of typical operating conditions in a fuel cell. It was found in the modeling that water emerging from a pore behaves very differently from water that impacts a surface, due to pinning of the droplet at the pore. They note that the carbon fibers are 5 to 10 microns in diameter and would have a significant effect on pore geometry [5]. It was also observed that coalescence of the droplets speeds up film formation [5]. They determined that a hydrophobic surface results in a saddle shaped flow, where the bulk of the flow is down the channel walls. Neutral hydrophobicity (a contact angle of 90 degrees) resulted in necking and then water droplet detachment. For hydrophobic cases with detachment, the droplet as it was being removed became spherical and occasionally lifted from the surface [6], this behavior is non-physical and requires accounting of the contact line motion to avoid these effects (as will be discussed later). They determined that a hydrophobicity greater than 140 degrees holds no functional benefit, and more hydrophobic channels result in higher flow losses due to pores being minimized in the coating process. It was predicted that water coverage, detachment diameter and friction factor are lower for higher air velocities.

Minor et al performed an experimental study using particle image velocimetry to shed light on the motion of the fluid particles within the droplet [7]. A channel of dimensions 3mm wide by 1mm high and approximately 13mm long was constructed on a glass slide. The 3mm wide surface was comprised of a PDMS layer covered at the channel surface by carbon cloth. A droplet was seeded at the GDL surface. The experimental data clearly showed a vortical motion within the droplet when it was subjected to airflow. This rotating flow effect will likely be affected by the enforcement in CFD simulations of the no-slip boundary condition at the contact line.

An interesting modeling study was performed by Jaio and Zhou [8] to observe the effects of gas diffusion layer (GDL) geometry. They used square and trapezoidal elements to imitate the pore structure of a GDL, producing three different scenarios. It was determined that the trapezoids with their minimum area facing the flow channel produced the best water removal [8]. They also determined that GDL shape and porosity have a profound effect on the water removal characteristics of a flow channel [8].

Another work of interest is that of Theodorakakos et al [9]. They used a Reynolds Averaged Navier Stokes (RANS) flow solver in conjunction with a custom CFD VOF method to determine the static and dynamic contact angles of various materials. The code used an unstructured grid with local refinement around the interface. A second order Crank-Nicholson method was used based on a global Courant number below 0.3. Convective and normal diffusion terms were modeled using a bounded second order upwind scheme; with cross-diffusion and second order derivatives discretized using a central difference scheme. The equations were solved using a conjugate gradient method solver. The contact angles they found are listed in Table 2 [9]:

Table 2: Contact angles for various materials [9]

	Contact Angle (Degrees)			
	Numerical			Experimental
Material	Static	Advancing	Receding	Static
Carbon Paper 1	125	140	50	120
Carbon Paper 2	130	140	70	140
Carbon Cloth	145	150	90	140
Graphite plate	90	110	70	

It was determined through the model that gravity and the feed water rates had little effect on the observed contact angles. It was also determined that temperature had a significant effect on the separation velocity of the droplet [9].

The second avenue of research has been in semi-empirical formulations to predict the droplet shedding characteristics. One such work is that of Kumbur and Mench [2], who proposes a droplet model based on a force balance of the droplet. A similar model was proposed almost concurrently by Chen et al [10].

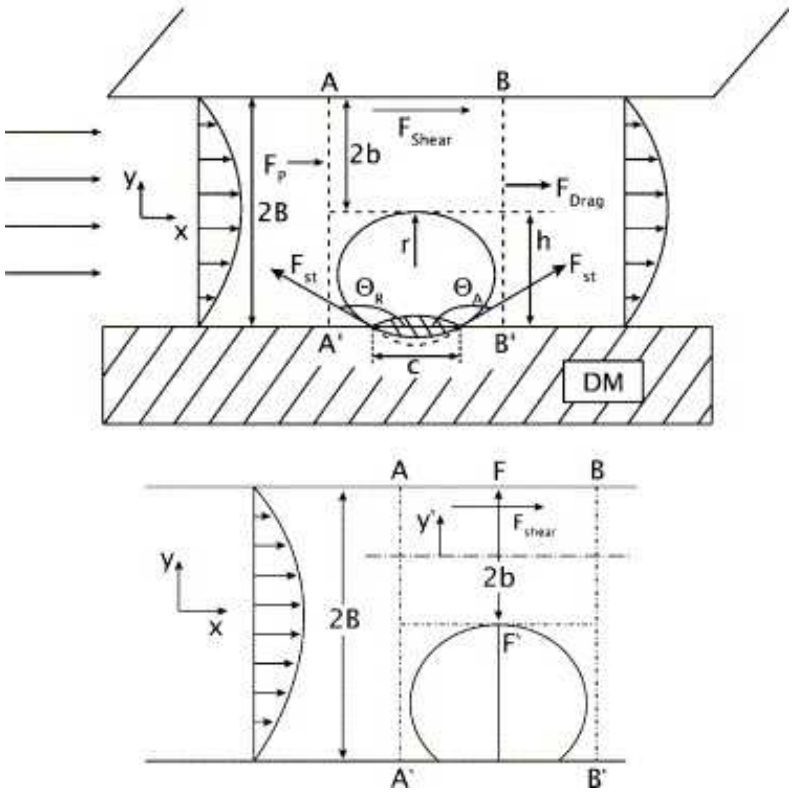

Figure 2: Kumbur model, top diagram shows the droplet with all the applicable forces acting on the domain and model parameters used in the calculation of the model. The bottom diagram shows the simplified version of the model domain and parameters used in the model [2]

The velocity in the drop section is assumed to be [2]:

$$u(y') = \frac{3u'}{2}\left(1-\left(\frac{y'}{b}\right)^2\right) \tag{1}$$

This flow field is not very accurate as it is a two dimensional representation that neglects the width of the channel as well as the adverse pressure gradient that results in an inflection point and eventual backflow (separation) on the rear portion of the droplet. The pressure drop is also calculated assuming a rectangular channel area.

The force associated with the surface tension is given as [2]:

$$F_{st} = \gamma_{lv} c \frac{\pi}{2} \left[\frac{\left[\sin(\Delta - \theta_A) - \sin(\theta_A) \right]}{\Delta - \pi} + \frac{\left[\sin(\Delta - \theta_A) - \sin(\theta_A) \right]}{\Delta + \pi} \right] \quad (2)$$

The force associated with the pressure change across the droplet [2]:

$$F_{Px} = \frac{24 \mu B U h^2}{\left(B - \frac{h}{2} \right)^3 (1 - \cos\theta_A)^2} \quad (3)$$

The force associated with the shear stress is [2]:

$$F_{Shear} = \frac{12 \mu B U h^2}{\left(B - \frac{h}{2} \right)^2 (1 - \cos\theta_A)^2} \quad (4)$$

The drag force is assumed to be equal and opposite to the surface tension force. The final equation is given as:

$$F_{Px} + F_{Shear} - F_{ST} = 0 \quad (5)$$

Chen et al's model [10] uses both a cylindrical droplet and a spherical droplet shape. The difference between the advancing and receding contact angle, known as the contact angle hysteresis, was analyzed. The data is only able to predict the experimental data for a surface simulating a GDL up to about 7 degrees of contact angle hysteresis; beyond this threshold value the experiments and model predictions diverge. An improved force balance model was developed in the early stages of research and can be seen in Appendix C.

Some methods have merged the two avenues by using semi-empirical relations in conjunction with CFD models to better approximate the flow dynamics of a droplet in a channel. One such work is that of Fang et al [11]. They point out the inability for current commercial software to account for the contact line history. As the contact angle is

dependant upon the direction and the speed of the contact line motion. They suggest the following models to predict the contact angle:

$$\sigma_{LG}\cos\theta_S = \sigma_{NET} \tag{6}$$

$$\frac{\cos\theta_{adv} - \cos\theta_{drop}}{\cos\theta_{adv} + 1} = \tanh\left(4.96Ca^{0.702}\right) \tag{7}$$

Where Ca is the capillary number (based on the contact line velocity), to determine the advancing angle and

$$\theta_{rec}{}^3 - \theta_{drop}{}^3 = C_t Ca \tag{8}$$

Where Ct is a constant, to determine the receding angle. They used a VOF method in conjunction with the Marker and Cell finite difference methods to formulate the solution [11]. They used an algebraic multi-grid solver and piecewise linear interface construction to determine the droplet shape. A Taylor series expansion was used in conjunction with Heaviside functions to ensure the contact angle is bounded between the advancing and receding angles. This method allows the contact line to remain stationary as the angle changes from the receding to the advancing angle, but moves when either angle is exceeded. The following contact angle information, in Table 3, was found:

Table 3: Contact angles for various GDL configurations [11]

Angle (deg)	Coated silicon	+/-	GDL 0% teflon	+/-	GDL 5% teflon	+/-	GDL 10% teflon	+/-
Advancing	105	1.1	124.6	0.9	144	1.1	149.6	0.8
Receding	65	1.2	36.8	0.9	91	1.3	116.2	1.5

Before addition of the contact angle hysteresis model the droplet would display separation to the point of suspended droplets as well as quasi-spherical droplets [11]. These phenomena are non-physical and were remedied once the hysteresis model was instituted, resulting in elongated droplets that were attached to the surface.

A paper by Chen [12] uses both analytical modeling and 3D flow dynamics software to estimate droplet detachment. By balancing the drag force against the surface tension it was found that:

$$U_c = \left[\frac{H_c}{\rho\mu}\right]^{1/3}\left[\frac{4\pi\gamma\sin^2\theta_s\sin\frac{1}{2}(\theta_a-\theta_r)}{15d(\theta_s-\sin\theta_s\cos\theta_s)}\right]^{2/3} \quad (9)$$

H_c - channel height
θ_s - static contact angle
θ_a - advancing contact angle
θ_r - receding contact angle

Various static contact angles and hysteresis values were chosen for a variety of materials to provide agreement with the simulation data.

Sikalo et al. [13] provide a good overview of the current models used to account for the dynamic contact angle using semi-empirical means. Most of the models assume Young's equation is valid throughout the dynamic process and the solid-liquid and the solid-vapor surface tensions vary with the flow field dynamics. Young's equation relates the interfacial tensions and the contact angle by performing a force balance at the three phase contact line.

$$\sigma\cos\theta_{equilibrium} = \sigma_{solid-liquid} - \sigma_{solid-vapour} \quad (10)$$

The paper presents the Cox formulation [13]:

$$Ca = \left(\ln\left(\varepsilon^{-1}\right) - \frac{Q_1}{f(\theta_D)} + \frac{Q_2}{f(\theta_e)}\right)^{-1}\left[g(\theta_D) - g(\theta_e)\right] + O\left(\frac{1}{\ln\left(\varepsilon^{-1}\right)}\right)^3 \quad (11)$$

Where ε is a dimensionless parameter based on the static contact angle mechanics. Q_1 and Q_2 are parameters based on the outer flow field and the slip conditions on the wall respectively. The functions f and g are dependent on the dynamic and equilibrium contact angles. Another popular contact angle formula is the Hoffman-Voinov-Tanner law [13]:

$$\theta_D^{\,3} - \theta_e^{\,3} = C_t Ca \text{ with } C_t \approx 72 \tag{12}$$

This formula again assumes that the capillary number is based upon the contact line velocity and using the standard formulation [13]:

$$Ca = \frac{(Vel)\mu}{\sigma} \tag{13}$$

A more recent formulation with potentially broader applicability is based on the Hoffman functions [13]:

$$\theta_D = f_{Hoff}\left[Ca + f_{Hoff}^{-1}(\theta_e)\right] \tag{14}$$

$$f_{Hoff}(x) = \arccos\left\{1 - 2\tanh\left[5.16\left(\frac{x}{1+1.31x^{0.99}}\right)^{0.706}\right]\right\} \tag{15}$$

This provides one of the best fits to experimental data and will be adapted for use in Fluent in the current work.

The major weakness in most of the models is in the stress singularity modeling. This issue can be resolved by using the Shikhmurzaev model to model the contact line dynamics. By using non-equilibrium thermodynamics he proposed the following model for the dynamic contact angle [14]:

$$\cos\theta_s - \cos\theta_D = \frac{2V\left(\rho_{2e}^{s*} + \rho_{1e}^{s*}u_o\right)}{\left(1-\rho_{1e}^{s*}\right)\left[\left(\rho_{2e}^{s*}+V^2\right)^{1/2}+V\right]} \qquad \rho_{ie}^{s*} = \frac{\rho_{ie}^{s}}{\rho_o^{s}} \tag{16}$$

In the formula V is the dimensionless contact line velocity, and the non-dimensionalized local densities are defined for each phase in reference to their equilibrium values where index 1 refers to the free surface and index 2 refers to the liquid-solid interface. The dimensionless contact line velocity is given by [14]:

$$V = U\sqrt{\frac{\tau\beta}{\rho_0^s\gamma\left(1+4\alpha\beta\right)}} \tag{17}$$

The parameter u_o is defined in the following way [14]:

$$u_o = \frac{\sin\theta_d - \theta_d\cos\theta_d}{\sin\theta_d\cos\theta_d - \theta_d} \tag{18}$$

The other variables found in the equation are phenomenological co-efficients given as:

$\alpha =$ Effect of suface tension gradient on the velocity distribution $\left(\alpha \propto \frac{h}{\mu}\right)$

$\beta =$ Effect of shear stress on the velocity distribution $\left(\beta \propto \frac{\mu}{h}\right)$

$\tau =$ Suface tension relaxation time $\left(\tau = \frac{5Sc^2h\mu}{\sigma_{1e}\left(1-\rho_{1e}^{s*}\right)}\right)$

This series of equations describe the dynamic contact angle behavior based on theoretical formulations and are comprised of material and flow field properties.

Each model has it own strengths and weaknesses. Some models are easily implemented but suffer from lower accuracy, while other models are complex to implement and potentially unstable from a numerical viewpoint, but are based on fundamental fluid dynamic considerations. In the current work the author has chosen to use the Hoffman functions to describe the dynamic contact angle due to the relatively simple implementation combined with a high level of agreement with experimental data.

2 Scope and Objectives

As noted in [1], two-phase flow regimes in PEMFC flow channels differ from more classical two-phase flow problems in that they occur in microchannels at low Reynolds numbers, and are characterized by large void fractions (low saturation) and important surface tension effects. The objective of this thesis is to examine the water droplet dynamics in a flow channel of relevance to a fuel cell. This will be accomplished by two different methods. The first method uses simplified analytical relations to determine droplet stability, and the second method utilizes a modified computational fluid dynamics module to provide a tool for fuel cell flow channel modeling.

The analytical model will expand on the previous work of Kumbar and Mench to provide better agreement with the experimental data obtained. A more physically realistic model is proposed to improve the predictive capabilities of the simplified analytical models.

The computation fluid dynamics module will implement a dynamic contact angle function into the commercially available Fluent software. This addition will allow the numerical models to better predict the characteristics of the water droplet as it evolves within the flow channel.

3 Problem Set-up

After selecting the Hoffman functions to describe the dynamic contact angle the model was implemented within the Fluent's user defined function framework. Fluent was chosen due to its widespread industry adoption and the well tested volume of fluid (VOF) multiphase models. These models are able to track two or more phases, providing a complete resolution of the flow field and interface dynamics.

3.1 Volume of Fluid Methods

The volume of fluid model tracks the content of each phase in each cell by using the volume fraction [15].

$\alpha_q = 0$ The cell is empty of phase q
$\alpha_q = 1$ The cell is full of phase q (19)
$0 < \alpha_q < 1$ The cell has an interface containing phase q

The addition of all the phase content variables is equal to one in order to ensure mass conservation [15].

$$\sum_{q=1}^{n} \alpha_q = 1 \quad \text{(for n phases)} \tag{20}$$

The addition of a phase volume fraction variable requires the solution of a saturation transport equation in addition to the set of fluid dynamics equations [15]:

$$\frac{\partial \alpha_q}{\partial t} + V \cdot \nabla \alpha_q = 0 \tag{21}$$

The equation is discretized using an explicit Euler scheme. The volume fraction at the current time step is calculated using the data from the previous time step, making the method non-iterative [15].

$$\frac{\alpha_q^{n+1}-\alpha_q^n}{\Delta t}+\frac{\Delta\left(U_f^n\alpha_{qf}^n\right)}{V}=0 \tag{22}$$

n = previous time step
$n+1$ = current time step
α_{qf} = face value of volume fraction (by second-order upwind scheme)
V = volume of the cell
U_f = volume flux through face f

To determine the fluid properties of each cell, the properties are averaged for the various phase components. This average is achieved with a weighted average using the phase composition variable [15].

$$B=\sum_{q=1}^{n}\alpha_q B_q \tag{23}$$

Where B is a fluid property such as density or viscosity. This provides the entire set of fluid properties in any given cell, based on the phases that are present in that cell. These averaged properties are used in a single momentum equation in order to solve the flow velocity field [15].

$$\frac{\partial}{\partial t}\rho u_j+\frac{\partial}{\partial x_i}\rho u_i u_j=-\frac{\partial P}{\partial x_j}+\frac{\partial}{\partial x_i}\mu\left(\frac{\partial u_i}{\partial x_j}+\frac{\partial u_j}{\partial x_i}\right)+\rho g_j+F_j \tag{24}$$

In the case of the micro-channel, the body forces are assumed to be negligibly small. This is due to the relatively small mass being acted on by the body forces when compared to the relatively strong surface tension forces. For a flow channel, with droplet dimensions in the order of less than 0.5mm and a water velocity less than 0.04m/s, the Webber number[16] is:

$$We = \frac{\rho U^2 L}{\gamma} \qquad \frac{\text{Inertia}}{\text{Surface Tension}}$$
$$We = \frac{(998)\left(0.04^2\right)(0.0005)}{0.0728} \approx 0.011 \tag{25}$$

Therefore, even at the extreme operating conditions the surface tension forces are approximately 100 times the strength of the inertia forces. As the water injection velocity is minimized and the droplets form small droplets this ratio just increases.

The interface is reconstructed based upon the volume fraction of the phases in surrounding cells. The method of reconstruction is a piecewise linear interpolation of the phase boundaries. This is accomplished by creating a planar face (or a line in two-dimensional simulations) within each cell, allowing for easy calculation of the flow through the interface.

Surface tension is modeled using the continuum surface force model, which is based on a pressure jump across the interface boundary [15].

$$\Delta P_{1-2} = \sigma\left(\frac{1}{R_2} + \frac{1}{R_1}\right) \tag{26}$$

With R_1 and R_2 the curvature of the interface along the orthogonal slice planes with the intersection of the two planes along the normal of the interface. Fluent uses the curvature formulation using the phase composition gradients. The surface normal is calculated from the secondary phase composition gradient [15].

$$n = \nabla \alpha_2 \tag{27}$$

The curvature of the interface is given by the divergence of the interface unit normal [15].

$$\kappa = \nabla \cdot \hat{n} = \left[\left(\frac{n}{|n|} \cdot \nabla\right) - \frac{1}{|n|}(\nabla \cdot n)\right] \tag{28}$$

This curvature is used to integrate the surface tension force into the numerical framework. The surface tension force term is added to the secondary phase momentum equation only, in the following form [15]:

$$F_{vol} = 2\sigma\kappa\alpha_2\nabla\alpha_2 \tag{29}$$

In order to accommodate a wall contact angle boundary condition, the normal of the interface at the cells in contact with the wall are adjusted to the prescribed contact angle [15].

$$\hat{n} = \hat{n}_w \cos\theta_{con} + \hat{t}_w \sin\theta_{con} \tag{30}$$

$\hat{n}_w$ = unit vector normal to the wall

$\hat{t}_w$ = unit vector tangential to the wall

θ_{con} = contact angle

This normal is then used in conjunction with the normal calculated in the usual fashion for the surrounding cells to provide the curvature at the interface.

3.2 Implementation of the Dynamic Contact Angle

The Hoffman formulation for the dynamic contact angle was implemented into Fluent through a set of new User Defined Functions (UDF) written in two parts. The first part of the code determines the unit normal for the phase boundary. The second part of the code determines the local capillary number and evaluates the Hoffman function to provide the main program with a local contact angle. The UDF code written in C is given in appendix A, and a flowchart is given in appendix B.

3.2.1 Determining the unit normal

To maximize the computational performance of the code, the gradients and other phase information evaluated during the calculation of the phase composition is released from memory as soon as the equation is solved. In order to access the VOF equations, and

associated data, within the user defined function, a phantom source term user defined function (DEFINE_SOURCE) must be created. In order to allocate the required memory locations an additional function (DEFINE_ADJUST) is required to set the system variables.

The solver calls this phantom source term code every time the VOF equations are solved. When the code is called it collects the phase gradients (C_VOF_G) for the boundary and stores them in a user-defined function (C_UDMI). The code then returns a source term of zero to the equations. This side steps the elimination of the VOF gradient data making it accessible to the main contact angle code when the boundary conditions are imposed.

3.2.2 Evaluating the dynamic angle

To set the dynamic contact angle a boundary condition user defined function (DEFINE_PROFILE) is required. The main purpose of the code is to determine the Hoffman function. The Hoffman function requires evaluation of the inverse Hoffman function based on the static contact angle.

$$\theta_D = f_{Hoff}\left[Ca + f_{Hoff}^{-1}(\theta_e)\right] \tag{14}$$

The code first evaluates the inverse function by means of a simple zero finding function. This provides the inverse Hoffman function for the prescribed static contact angle.

The code then accesses the phase gradients from the user-defined location saved in the first stage of the code. These phase gradients are brought into the code, and then normalized. This provides a unit vector in the direction of the interface normal to be used for determining the contact line velocity.

The contact line velocity is found by determining the flow field velocity (C_U, C_V, C_W) for the mixture then taking the dot product along the unit normal vector

(NV_DOT). This gives a velocity normal to the phase interface to be used in the capillary number calculation.

$$Ca = \frac{V\mu}{\sigma} \tag{13}$$

The capillary number is calculated and then the Hoffman function is evaluated. The dynamic contact angle is returned to the main program at each location and the next iteration begins.

3.3 The Computational Model

A three-dimensional, laminar flow, isothermal model is used to simulate the physical processes of interest. It uses the two-phase VOF model as described above with an unsteady flow formulation. The model includes wall adhesion and a surface tension coefficient of 0.0728 N/m, as this is the surface tension of water and air at 20 degrees Celsius [16]. The pressure term is evaluated using a body-force weighted scheme and the momentum equation is solved using a second order upwind scheme. The interface is reconstructed using the geo-reconstruction method as described above. This provides the basic case set-up for the model.

3.4 The Model Domain and Boundary conditions

The model domain selected for evaluation was a 250 micrometers square channel extending for 1.5 millimeters as shown in figure 3. A pore of size 50 micrometers square was located 350 micrometers from the entrance to the flow channel to eliminate entrance effects. The pore was modeled with a height of 20 micrometers to eliminate the possibility for entrance effects on the water emergence from the pore. The size and shape of the channel was chosen based on an average size fuel cell flow channel. A square pore shape was chosen as it is representative of the on average of the pores forming due to the superposition and intersection of the fibers that form the gas diffusion layer. The dimensions, as well as the flow conditions, correspond to the concurrent experiments conducted in the ESTP lab at the University of Victoria. The air flow velocities span the range of velocities seen in current fuel cell designs. The water injection velocities correlate to the water production and transportation seen within a fuel cell when

operating under both normal and high load conditions. The simulations are performed with the following boundary conditions:

Inlet: Prescribed air velocity of U (varied).

Outlet: Convective outflow condition.

Bottom wall: No slip condition with dynamic contact angle θ_D (obtained by modifying the static contact angle using the UDF).

Side walls: No slip condition with constant static contact angle θ_s (varied).

Top wall: No slip condition with constant static contact angle θ_s (varied).

Water inlet: Prescribed water injection velocity V (varied)

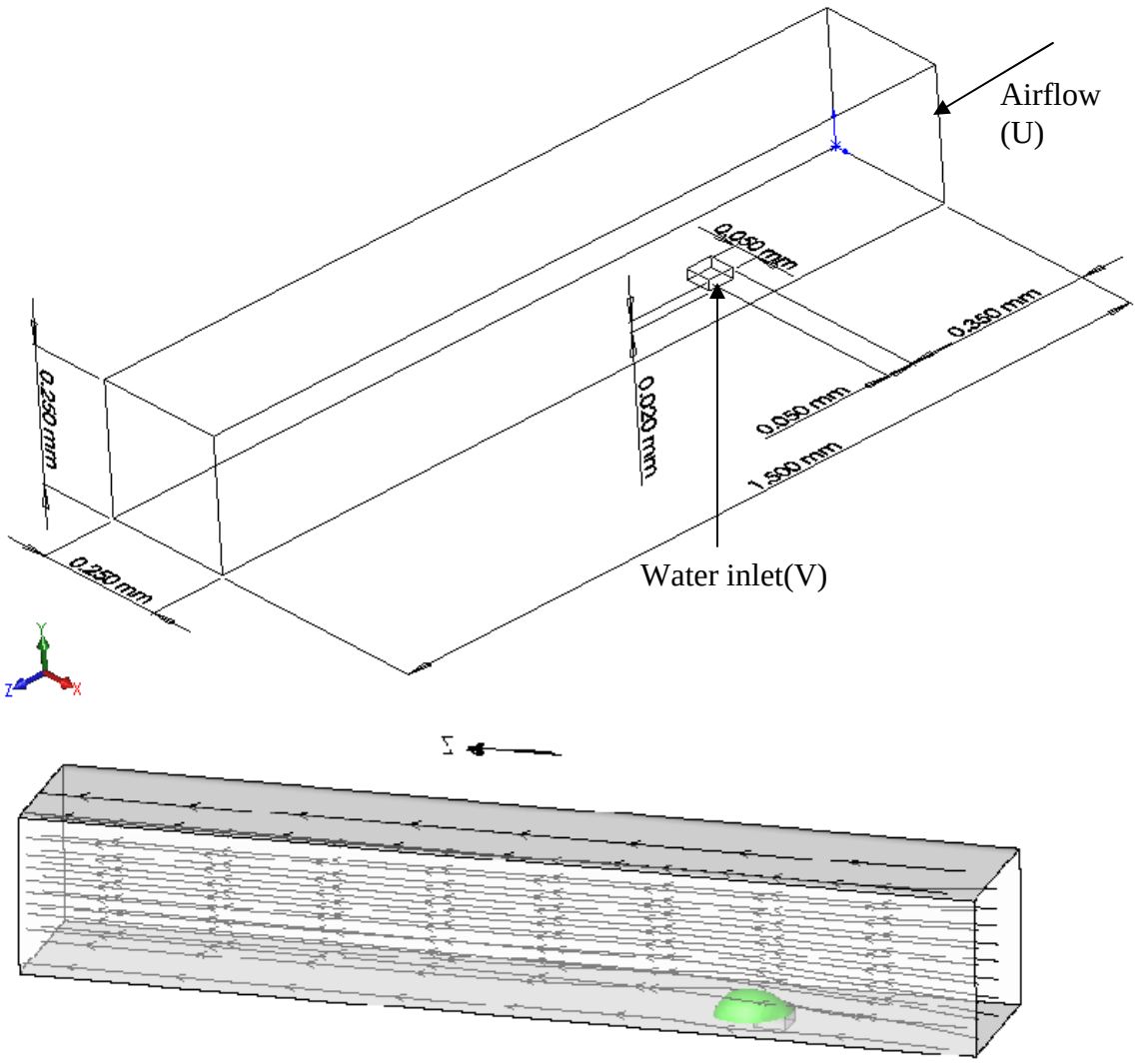

Figure 3: Model domain with air flowing from right to left and water being injected from below through a square pore

The mesh is a quadrilateral mesh with approximately uniform mesh sizing resulting in approximately one hundred thousand cells.

4 Results

The user-defined function was tested in a number of cases with various boundary conditions. Cases were also examined to determine the effects of changing the system input variables. The parametric study included variation of the air speed U, the water injection velocity V, and the static contact angle θ_s. However, the first step was a mesh independence study and a validation of the dynamic contact angle code.

4.1 Mesh Independence study

The first step in the model validation is a mesh independence study to verify that the solution is not influenced by the mesh size. To verify the mesh independence the mesh size was reduced from the size used in the rest of the investigation from 10 micrometers to 7.5 micrometers. The case chosen for comparison has an air speed of 10 m/s and a water injection velocity of 2 cm/s. The static contact angle is assumed to be 110 degrees. The two plots are compared in figures 4 and 5.

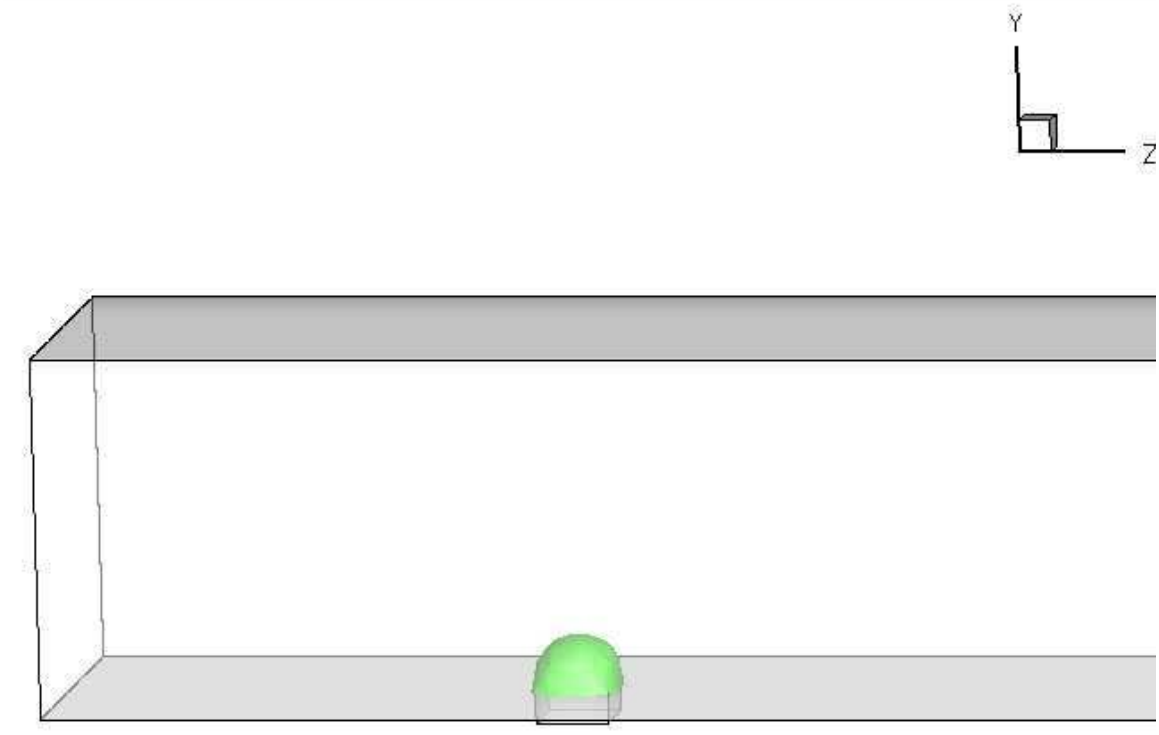

Figure 4: Phase Boundary Plot, 10 micron mesh size 2ms, water droplet emerging from a pore

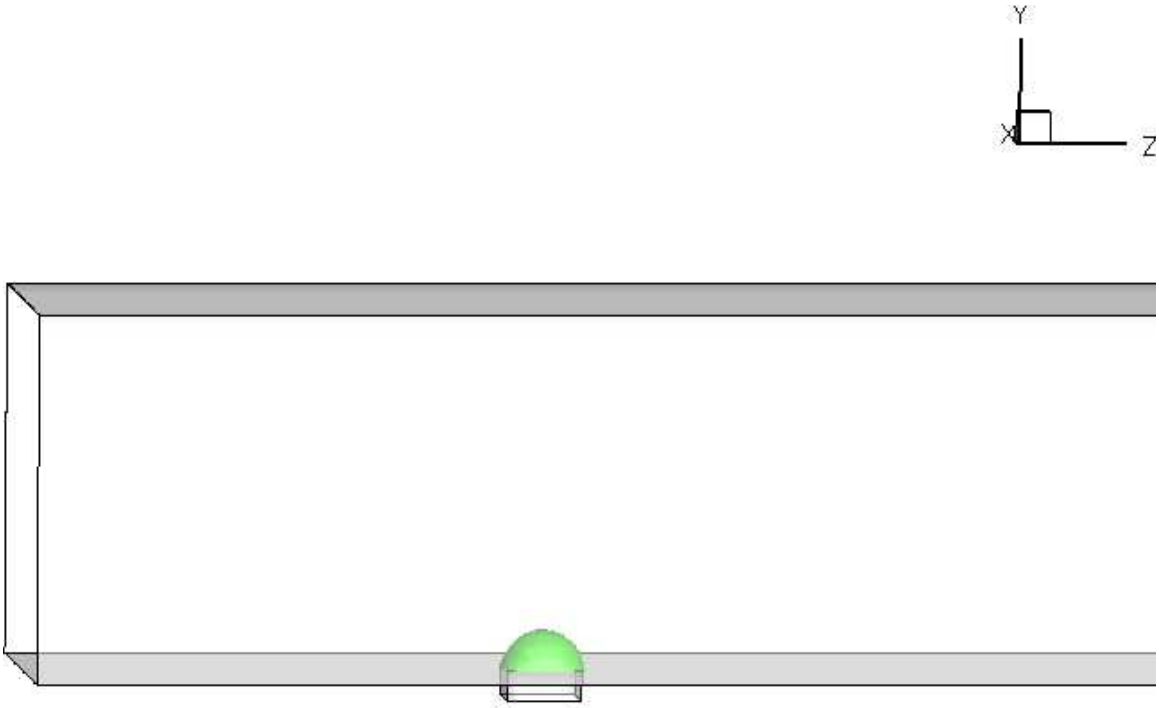

Figure 5: Phase Boundary Plot, 7.5 micron mesh size 2ms, water droplet emerging from a pore

Similar profiles can be seen in both plots. At a time step of two milliseconds, the droplet is growing out of the pore and beginning to take shape. This continues as time progresses. A later time step can be seen in figures 6 and 7.

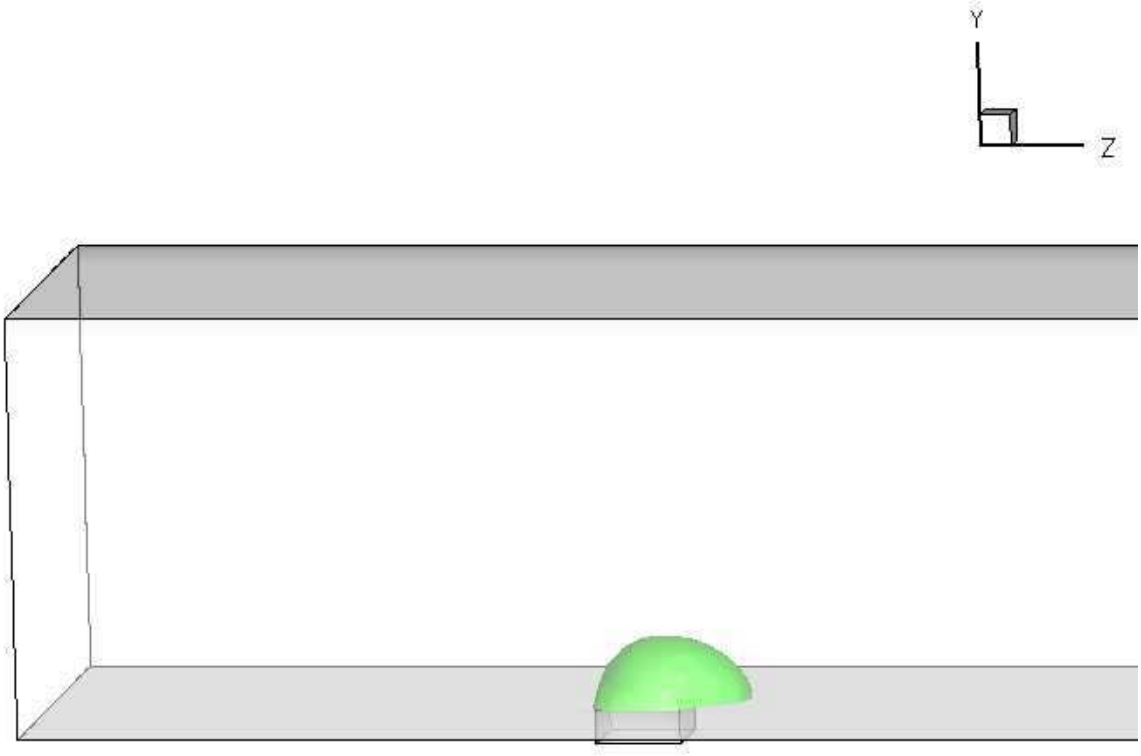

Figure 6: Phase Boundary Plot, 10 micron mesh size 7 ms, water droplet emerging from a pore

Note how the droplet is growing downstream with the trailing edge still connected to the pore. This profile is prevalent throughout the study when the dynamic contact angle formulation is used.

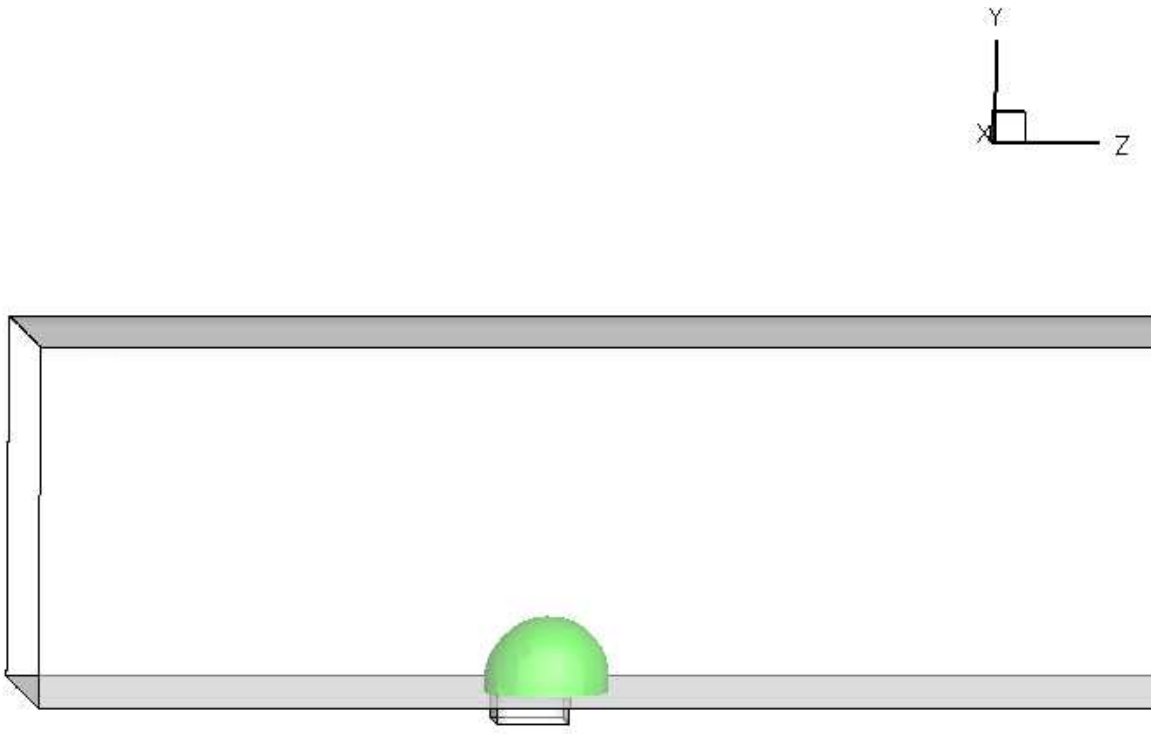

Figure 7: Phase Boundary Plot, 7.5 micron mesh size 7ms, water droplet emerging from a pore

It can be seen in figures 6 and 7 that the droplet is growing in the same manner from the pore. Next the pressure profiles will be compared for the two cases. The pressure plots can be seen in figures 8 and 9, in terms of the non dimensional pressure coefficient:

$$C_p = \frac{\left(P - P_{ref}\right)}{\frac{1}{2}\rho_{Air} U^2_{\text{Air inlet velocity}}} \tag{31}$$

The reference pressure is taken at x=0.150mm. The two lines correspond to the maximum and minimum pressure in the sectional slice

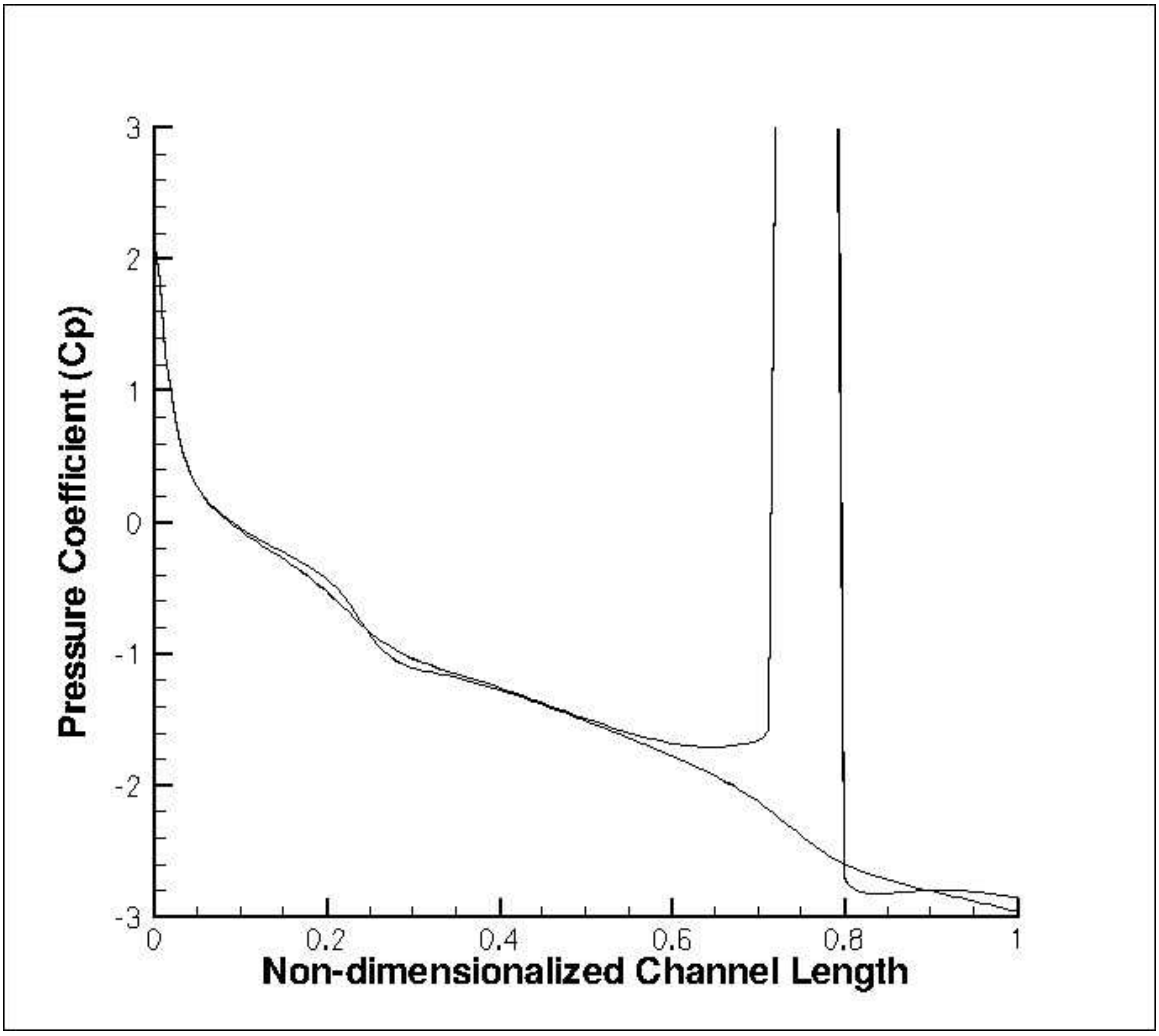

Figure 8: Non-dimensionalized Pressure Curve, 10 micron mesh size, 12 ms, the pressure spike represents a droplet in the channel. The two curves represent the max and min values.

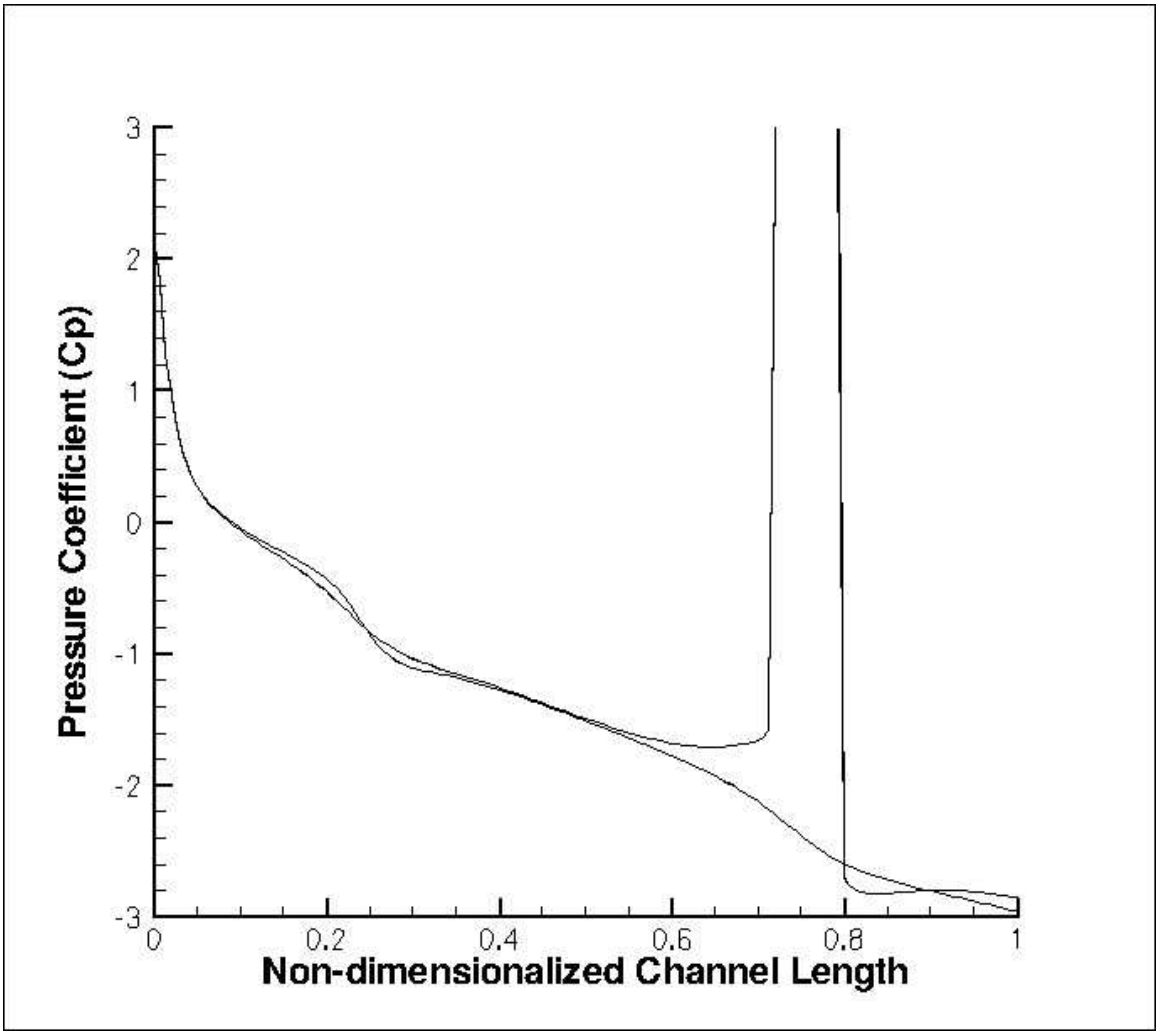

Figure 9: Pressure Curve, 7.5 micron mesh size, 12ms, the pressure spike represents a droplet in the channel. The two curves represent the max and min values.

By comparing figures 8 and 9 the similarities in the solution are apparent. They both have the same slight pressure disturbance at the pore where the new pore is emerging, and have a large pressure spike located at the droplet. The pressure spike is slightly narrower in figure 9 as a result of the increased resolution; however the trends remain the same. It can be concluded that the mesh size at the mesh scales present in the study have a minimal effect on the solution and therefore the mesh size of 10 microns will be used in the remainder of the study.

4.2 Validation of the Dynamic Contact Angle Model and Base Case Simulations

Prior to performing the simulations, the dynamic contact angle code is validated against a well documented two-phase problem. The case selected is a water droplet impacting a horizontal surface. After validating the use of a dynamic contact angle model, simulations corresponding to three "Base case" scenarios relevant to fuel cells will be presented. Three different boundary condition cases were examined in order to verify the validity of using the dynamic contact angle code as compared to the standard static contact angle formulation currently being used by the commercially available codes. The static contact angle in each of the cases was held constant at 110 degrees. The air speed and the water injection velocity were altered to achieve a variety of test conditions.

4.2.1 Droplet Impacting a Horizontal Surface

The validation case of a water droplet impacting a horizontal surface was chosen because it is a well documented two-phase case. The work of Sikalo and Ganic [17] documents droplets impacting horizontal and inclined surfaces. The case of interest for validating the droplet impact dynamics is the impact of a water droplet onto a horizontal wax surface. The simulation was run using the standard static contact angle code as well as the dynamic contact angle code. These simulations are compared against the high speed camera images of Sikalo and Ganic. The images used for comparison are shown in figure 10.

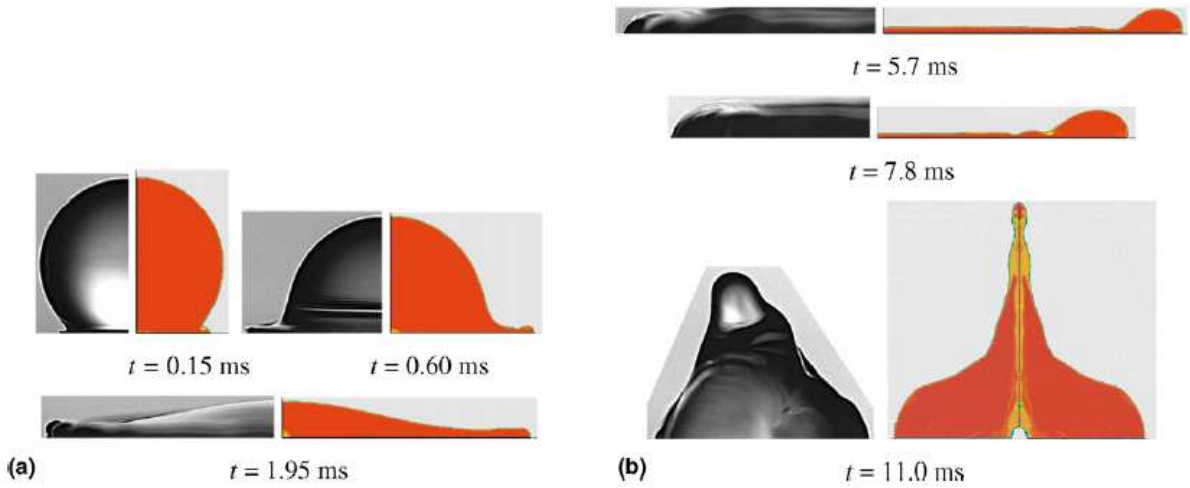

Figure 10: Water droplet impacting a wax surface experimental (camera) and simulation (red) [17]

The numerical simulation was first run using the standard static contact angle model. Then the case was run using the user defined function providing a dynamic contact angle. First the static and dynamic contact angle models are compared, and then the dynamic contact angle model is compared with the camera images shown in figure 10. It should be noted that the photographs do not provide an accurate view of the droplet cross-section. The blurred regions, most prevalent in time steps 1.95, 5.7 and 7.8ms, are introduced due to the depth of the image field. Only the sharp edges should be considered in evaluating the droplet profile, as the irregular nature of the droplets leading edge and the various depths in the cameras field of vision.

The droplet model used for comparison uses the same conditions as those present in the camera images. The droplet size is 2.7mm and the Webber number is 90, which results in a droplet velocity of approximately 1.57m/s. Figures 11 and 12 show the dynamic and the static contact angle models respectively.

4.2.1.1 Dynamic and Static Contact angle comparison

The numerical model was two dimensional with an axis-symmetric boundary condition along the x axis. The droplet is initialized at the point of the droplet impacting the surface. The velocity of the droplet was chosen to achieve a Webber number of 90, with a droplet diameter of 2.7mm. The plots are shown in figures 11 through 22.

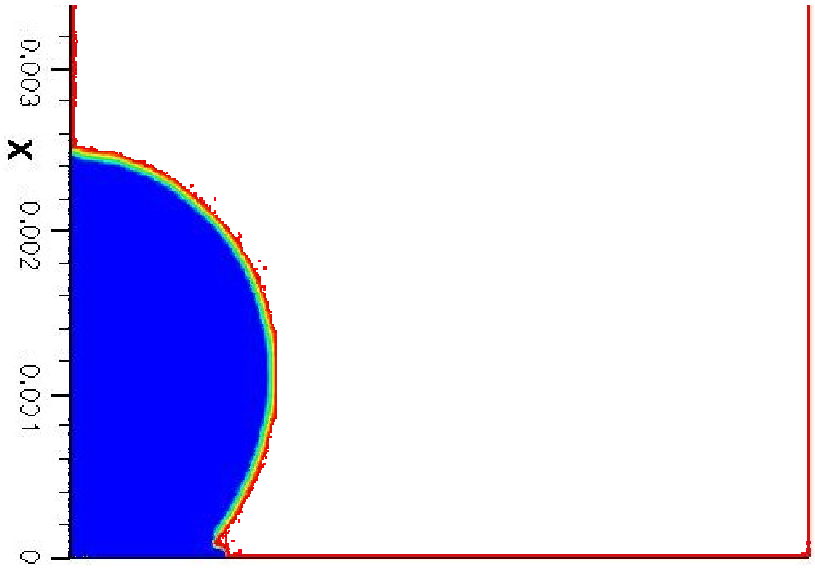

Figure 11: Droplet impact, dynamic contact angle, 0.15ms (length in m)

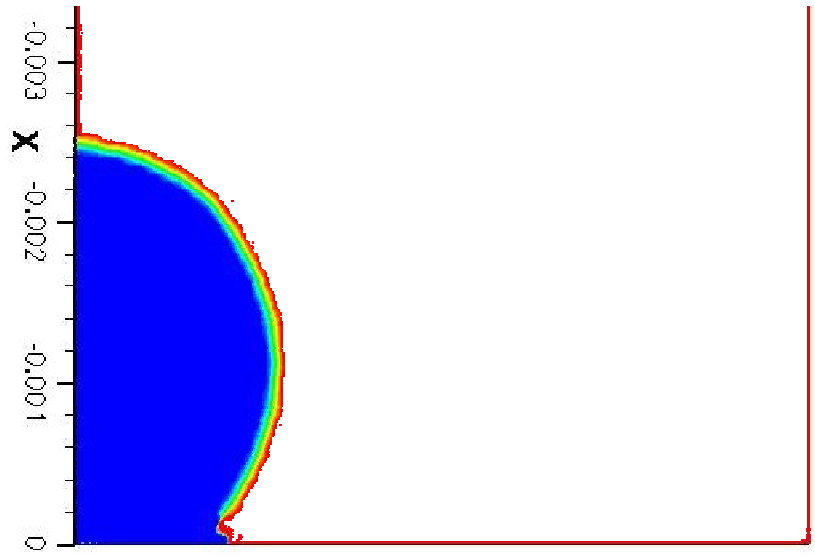

Figure 12: Droplet impact, static contact angle, 0.15ms (length in m)

Figures 11 and 12 show little difference at this early time step between the static and dynamic contact angle simulations. The blue region is fully saturated with the water phase and the white region is air only. The droplet has just hit the surface and is spreading along the surface as the droplet impacts. The high velocity of the droplet at the time of impact results in the spreading of the droplet. The static case shows a taller droplet edge emerging at the bottom of the droplet. We would expect that bulge to be smaller as the surface is a wetting surface.

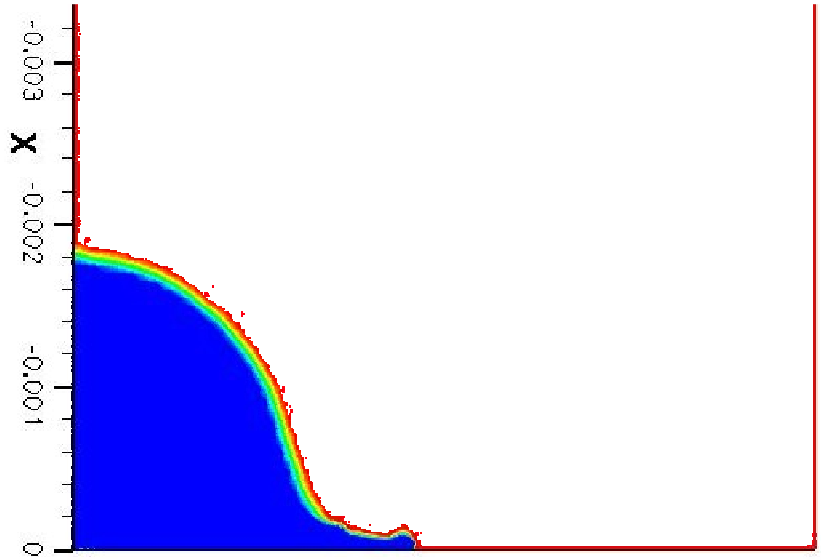

Figure 13: Droplet impact, dynamic contact angle, 0.6ms (length in m)

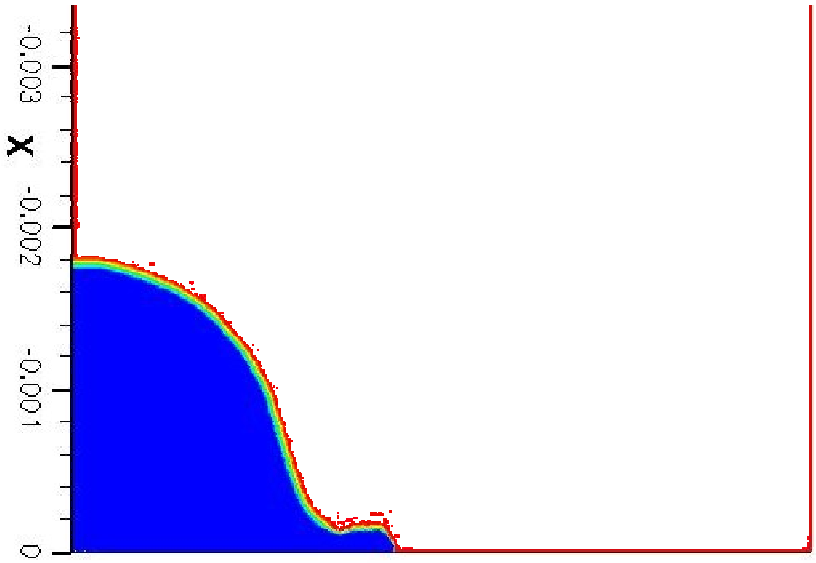

Figure 14: Droplet impact, static contact angle, 0.6ms (length in m)

Figures 13 and 14 show the droplet as it has evolved to the later time step of 0.6ms. Again the droplet shows faster spreading with the dynamic contact angle, as compared to the static contact angle model. The droplet is quickly spreading out with a smaller leading edge droplet profile. This is to be expected as the dynamic contact angle produces a higher contact angle when the three-phase contact line is in forward motion.

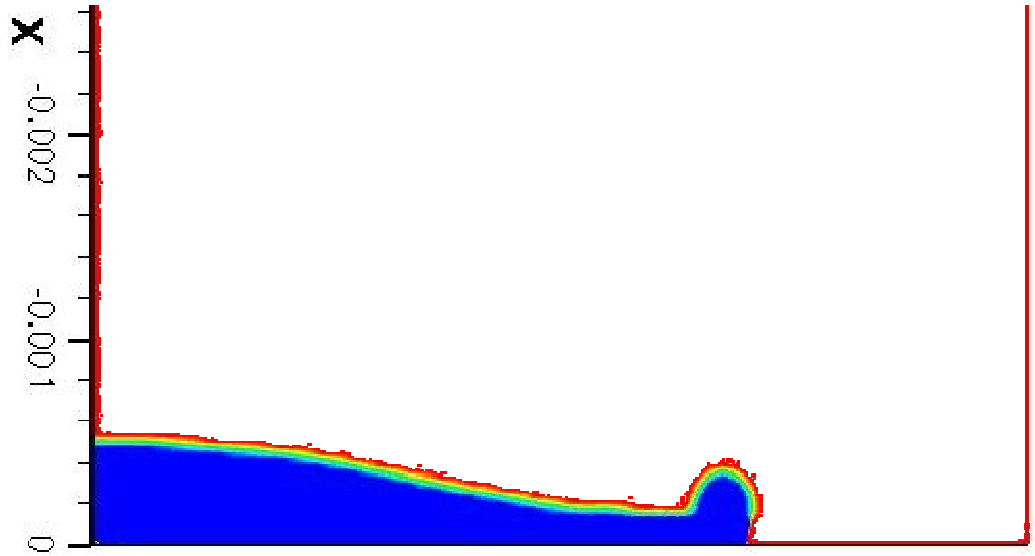

Figure 15: Droplet impact, dynamic contact angle, 1.95ms (length in m)

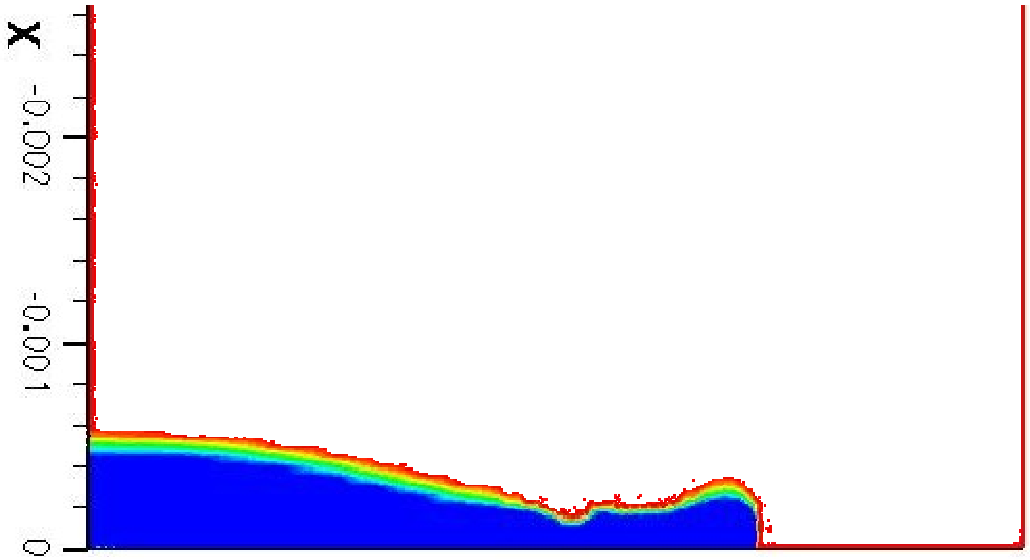

Figure 16: Droplet impact, static contact angle, 1.95ms (length in m)

Figures 15 and 16 show the droplet as it starts to reach its largest size at a time of 1.95ms. The dynamic contact angle results in a thinner leading edge with a more distinct leading ridge. The static contact angle formulation results in an irregularly shaped profile with a square looking leading edge. This is not seen in real experiments.

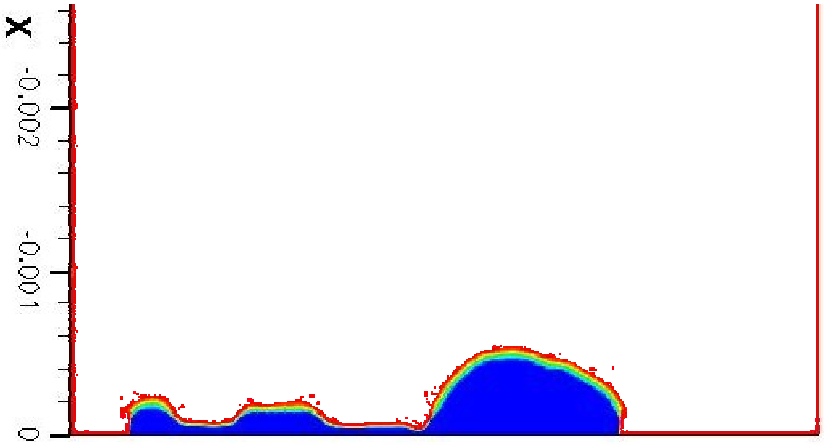

Figure 17: Droplet impact, dynamic contact angle, 5.7ms (length in m)

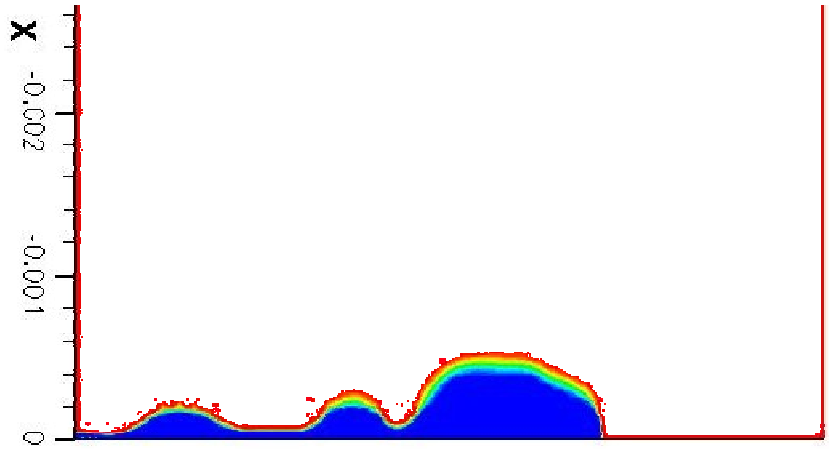

Figure 18: Droplet impact, static contact angle, 5.7ms (length in m)

Figures 17 and 18 show the simulations at their largest radius, just before the droplet contact line begins receding. Both static and dynamic simulations exhibit similar trends, with the droplet spreading out into multiple ridges. The dynamic contact angle model has a large leading edge ridge and smaller inner droplet ridges. The static contact angle model is similar, but with larger inner ridges.

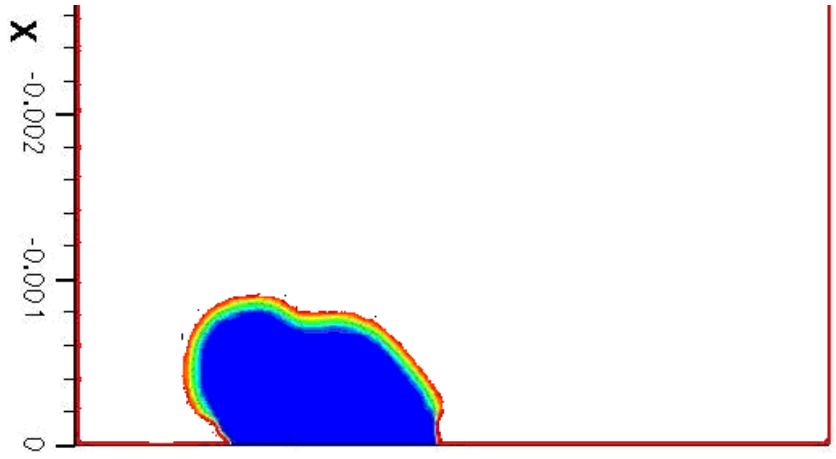

Figure 19: Droplet impact, dynamic contact angle, 7.8ms (length in m)

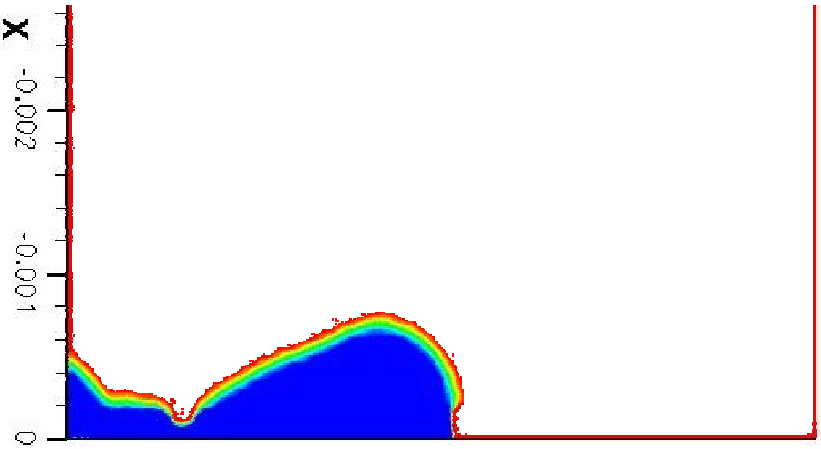

Figure 20: Droplet impact, static contact angle, 7.8ms (length in m)

At a time of 7.8ms, the droplets are now retreating into a shape closer to the equilibrium shape. The dynamic contact angle shows the droplet moving back towards the center with the droplet sloped towards the center axis. The static contact angle model shows an almost flat outer face.

The final time step, at 11 milliseconds, is shown in figures 21 and 22.

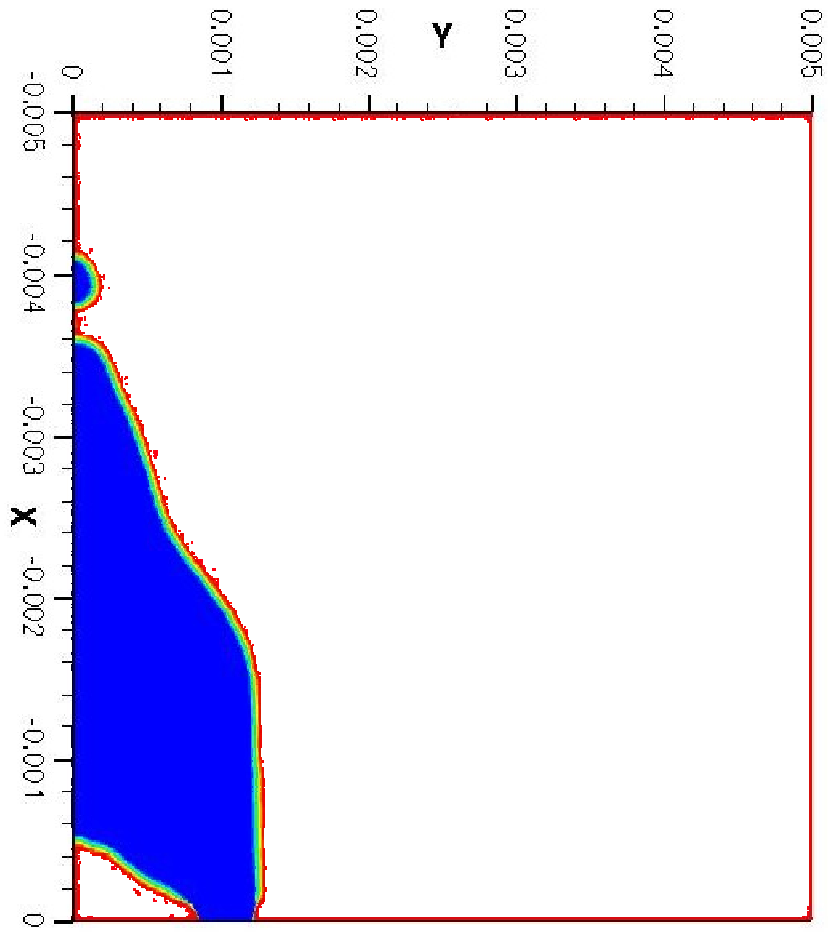

Figure 21: Droplet impact, dynamic contact angle, 11ms (length in m)

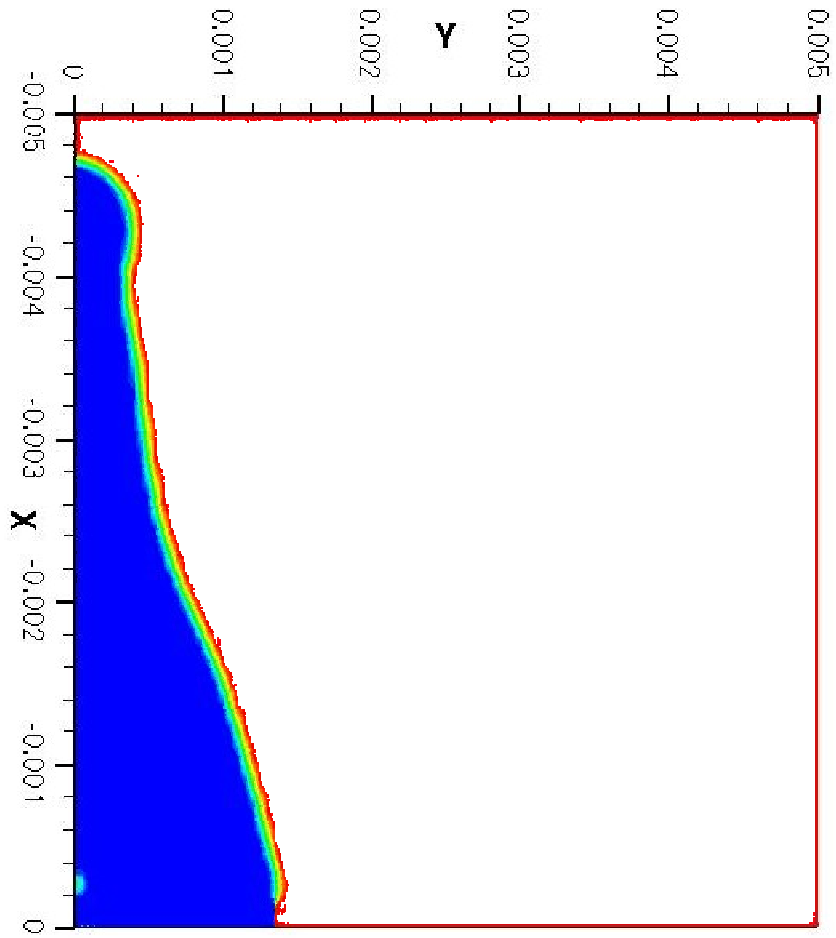

Figure 22: Droplet impact, static contact angle, 11ms (length in m)

Comparing the two plots at the final time step we see a similar trend; however, the static contact angle model results in a cone shaped droplet, whereas the dynamic contact angle model produces a more irregular shape. The dynamic contact angle model results in a lower rebound height and droplet separation. The dynamic contact angle model does appear to model the dynamics of the water motion more accurately.

4.2.1.2 Comparison with Experimental Images

The dynamic contact angle model is compared with the experimental images in figures 23 through 28.

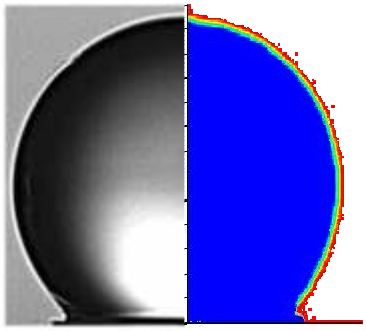

Figure 23: Droplet comparison of experiments (left) and numerical droplet shape at t=0.15ms

Figure 23 shows the droplet just after impact. Experiments show the edge of the droplet contact line has a small bulb shape. This is reproduced in the numerical and experimental images, with a near spherical droplet shape in the bulk of the droplet and a small leading edge lip at the contact point.

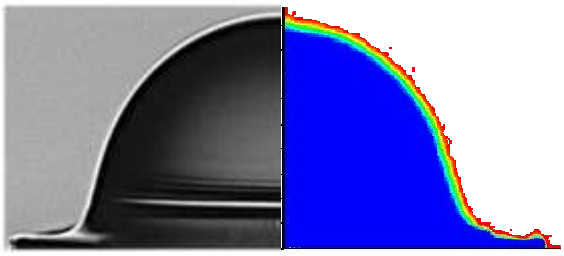

Figure 24: Droplet comparison of experiments (left) and numerical droplet shape at t=0.6ms

Figure 24 shows the droplet as it is approximately half impacted with the surface. The top portion of the droplet retains its near spherical shape, with the contact line edge spreading out in a radial direction. Again the experimental and numerical droplet profiles are very similar.

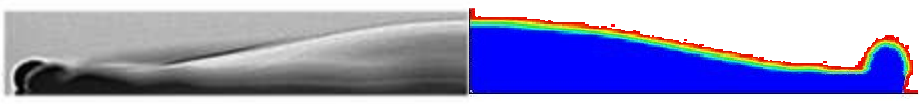

Figure 25: Droplet comparison of experiments (left) and numerical droplet shape at t=1.95ms. Blurred regions indicate out of plane droplet profiles obscuring the centerline plane profile.

Figure 25 shows the droplet spreading across the surface. The body of the droplet is humped, with a leading edge droplet ridge. The leading edge ridge in both images is very prominent, showing a similar profile.

Figure 26: Droplet comparison of experiments (left) and numerical droplet shape at t=5.7ms. Blurred regions indicate out of plane droplet profiles obscuring the centerline plane profile.

Figure 26 shows the droplet at its most extended shape. The profile in the image seems to show the droplet edge has already reached its largest radius. The contact line is beginning to change contact angle from its advancing to receding angle. The two images are very similar as they both show an uneven edge profile, with multiple ridges.

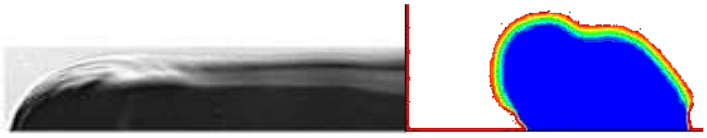

Figure 27: Droplet comparison of experiments (left) and numerical droplet shape at t=7.8ms. Blurred regions indicate out of plane droplet profiles obscuring the centerline plane profile.

Figure 27 shows the droplet as it is returning to a closer representation of the equilibrium profile. The simulation shows a higher rebound profile than the experimental image shows. The simulation clearly shows the advancing and receding contact angles. It is worth noting that the outer contact line angles are very similar. The experimental image also seems to show a profile supporting a droplet ring as compared to a disk shape. This is to be expected as the material is hydrophobic, with a contact angle larger than ninety degrees.

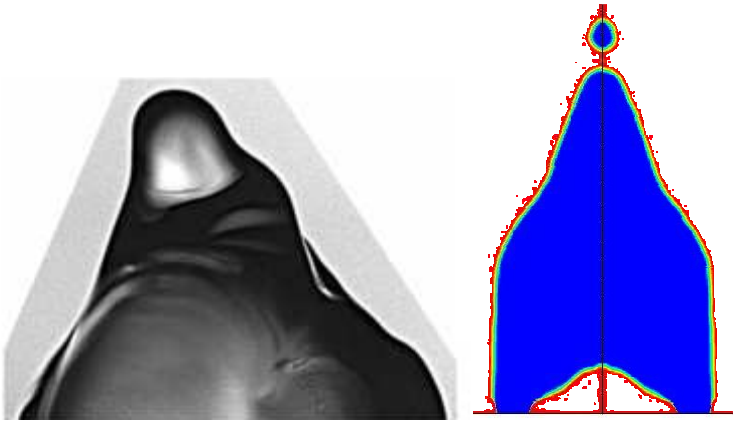

Figure 28: Droplet comparison of experiments (left) and numerical droplet shape at t=11ms

Figure 28 shows the droplet at its rebound shape. The images both show a rather random droplet profile, with the tip tending towards separation. The assumption of an axis-symmetric profile is not correct which leads to the discrepancies between the images. The series of figures show that the dynamic contact angle model is able to predict the droplet profiles with a relatively high degree of accuracy. Therefore, the dynamic contact angle model will be used in the simulations of the droplets in a flow channel. A number of validation cases will be presented representing a variety of different flow conditions in a fuel cell flow channel.

4.2.2 Flow Channel Base Case One

The first base case to be examined uses an air velocity of U=10m/sec, and a water injection rate U=0.04m/sec. These values are the highest air and water injection velocities that will be examined in this study. This discussion is made in light of some preliminary unpublished experimental data obtained in-house [18].

The static contact angle formulation provides interesting droplet growth characteristics. The droplet profile at two milliseconds is shown in figure 29.

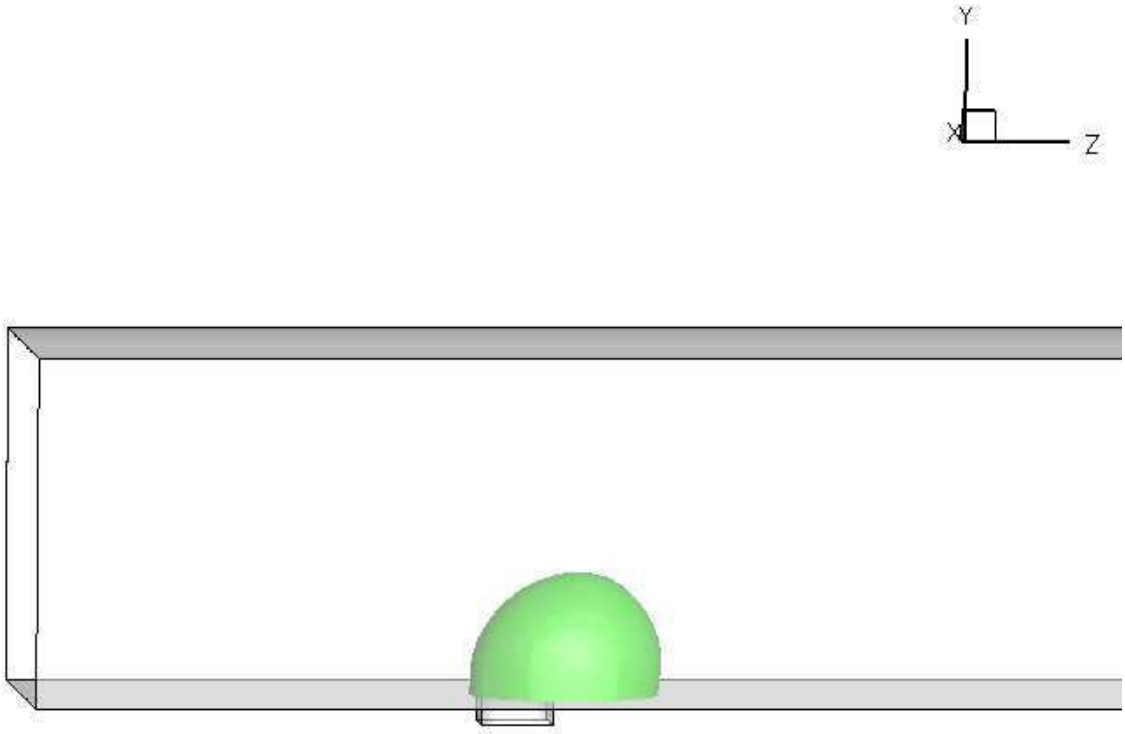

Figure 29: Phase boundary static contact angle, 4cm/s water injection, 10m/s air speed at a time of 2ms, water droplet emerging from a pore

It can be seen from figure three that the droplet grows in a near spherical shape out of the pore. This is an artifact of the static contact angle boundary condition, which forces the droplet into an unphysical shape. Figure 30 shows a plot of the pressure through the channel for the same time step.

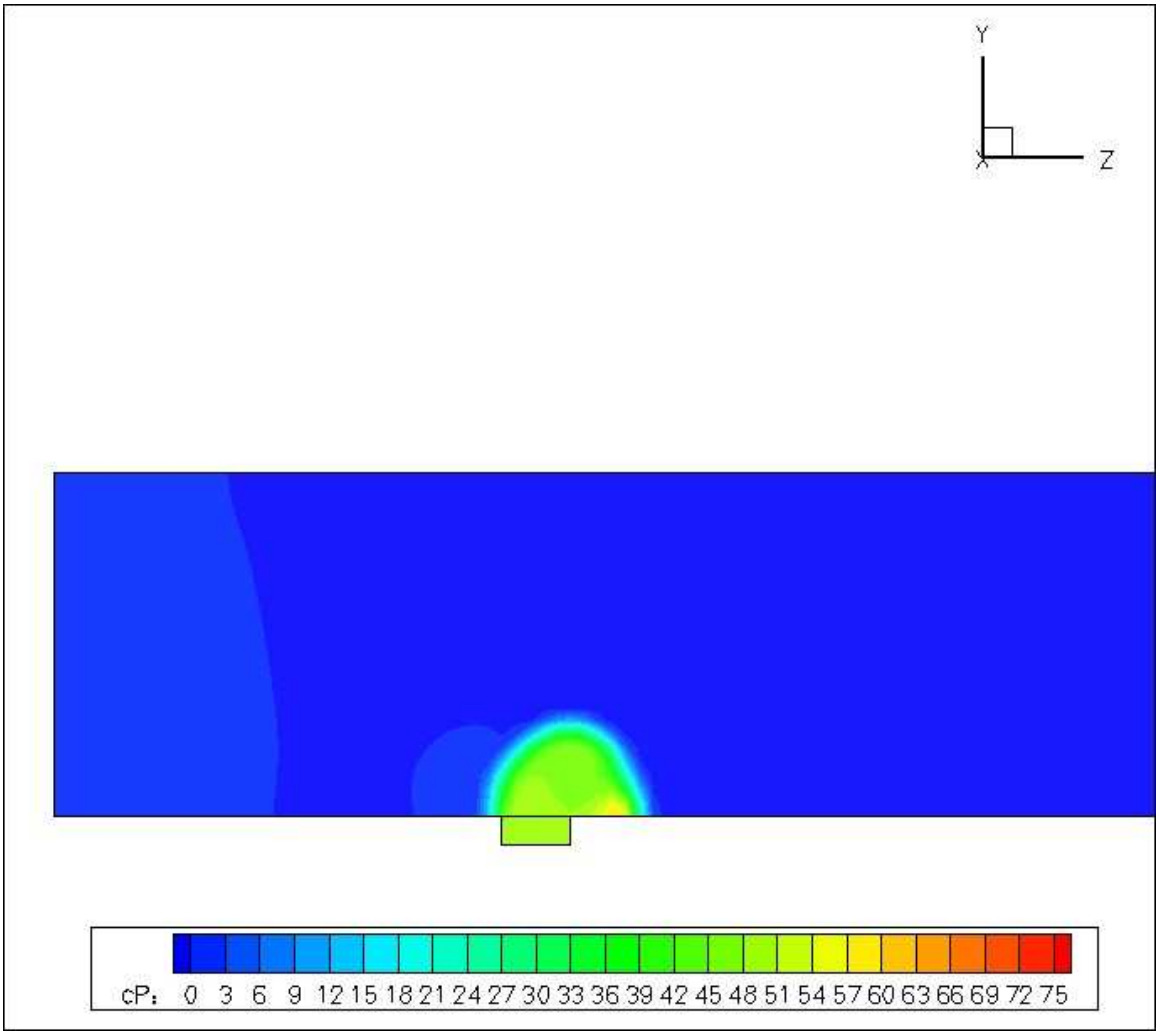

Figure 30: Pressure slice (in Pa) static contact angle, 4cm/s water injection, 10m/s air speed at a time of 2ms, water droplet emerging from a pore

Figure 30 illustrates the pressure distribution in and around the water droplet. There is a high-pressure region at the trailing edge of the droplet, and a high-pressure wave ahead of the droplet where the air contacts the large spherical droplet.

Comparing these plots to those produced by the dynamic contact angle at the same time step demonstrates the improved physics resulting from the dynamic contact angle

implementation. Figure 31 shows the phase boundary for the dynamic contact angle model.

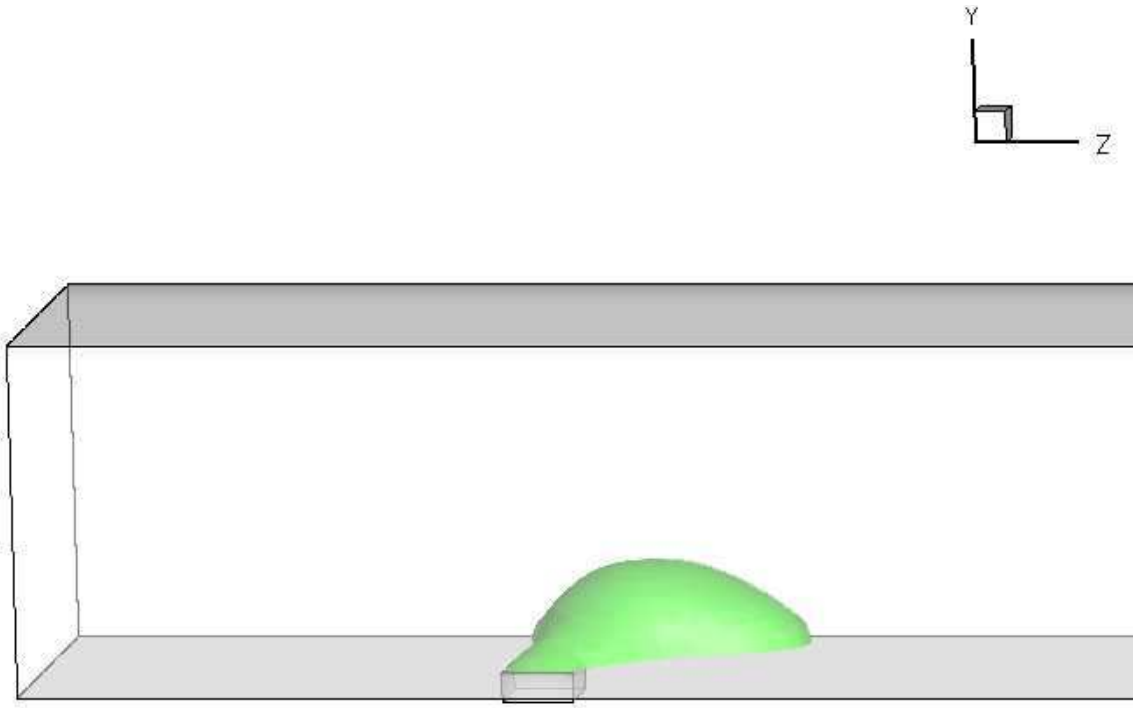

Figure 31: Phase boundary dynamic contact angle, 4cm/s water injection, 10m/s air speed at a time of 2ms, water droplet emerging from a pore

Note how the droplet forms an elongated shape extending from the pore. This elongated droplet profile is consistent with preliminary experimental data and highlights the necessity of accounting for the dynamic contact angle in the numerical solution. The pressure plot at this same time step is shown in figure 32.

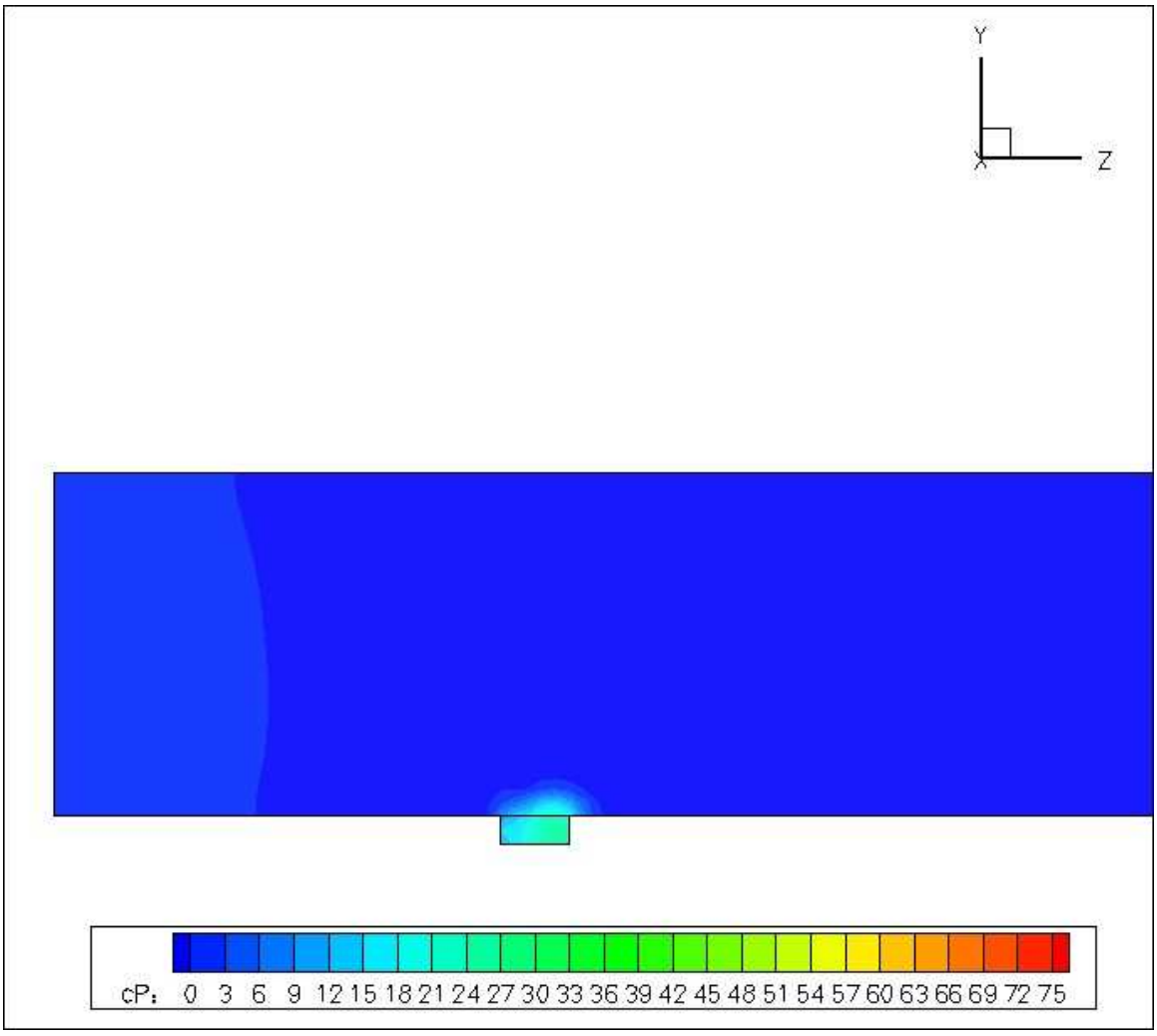

Figure 32: Pressure slice (in Pa) dynamic contact angle, 4cm/s water injection, 10m/s air speed at a time of 2ms, water droplet emerging from a pore

The pressure plot for the dynamic contact angle has a more realistic profile. The pressure within the droplet is higher than outside, but remains relatively uniform. There is no upstream pressure front as seen in the static case.

Next the same case is evaluated at a later time step. Figure 33 shows the phase boundary at three milliseconds.

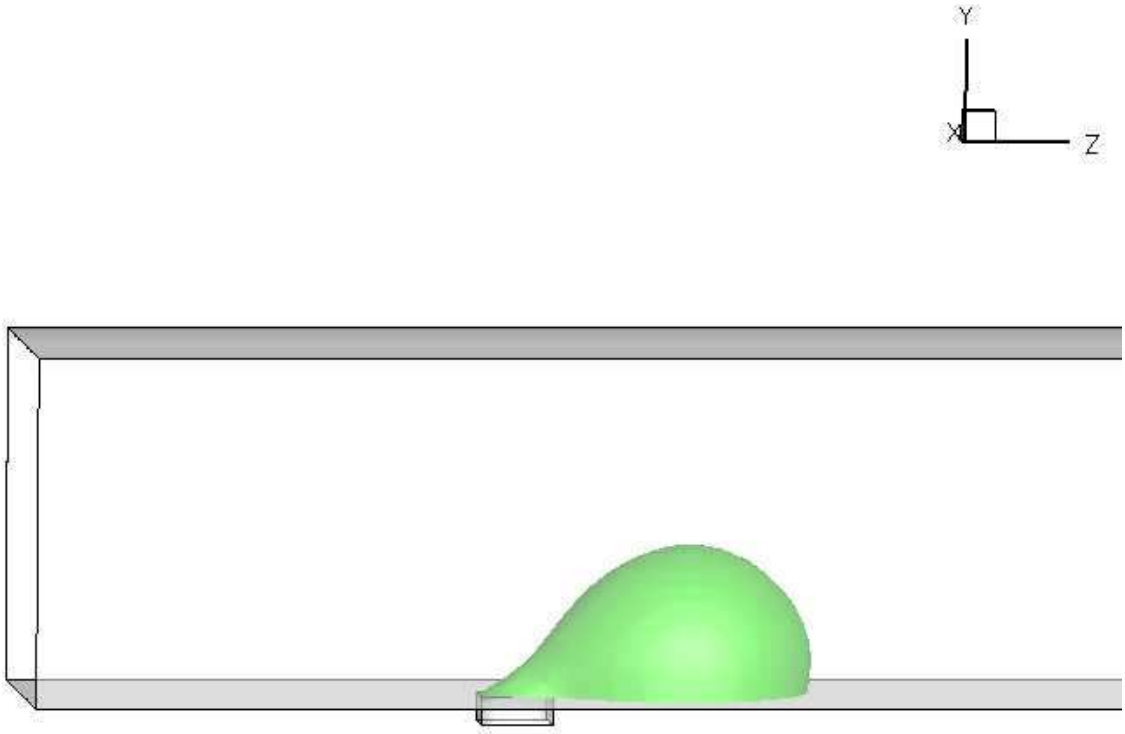

Figure 33: Phase boundary static contact angle, 4cm/s water injection, 10m/s air speed at a time of 3ms, water droplet emerging from a pore

The spherical shape of the droplet is very prevalent in figure 33. As time evolves the tail grows thinner and the droplet forms a nearly perfect spherical shape. The droplet continues downstream with the same spherical shape as the new droplet begins to form a spherical shaped head. The pressure plot at this same time-step is shown in figure 34.

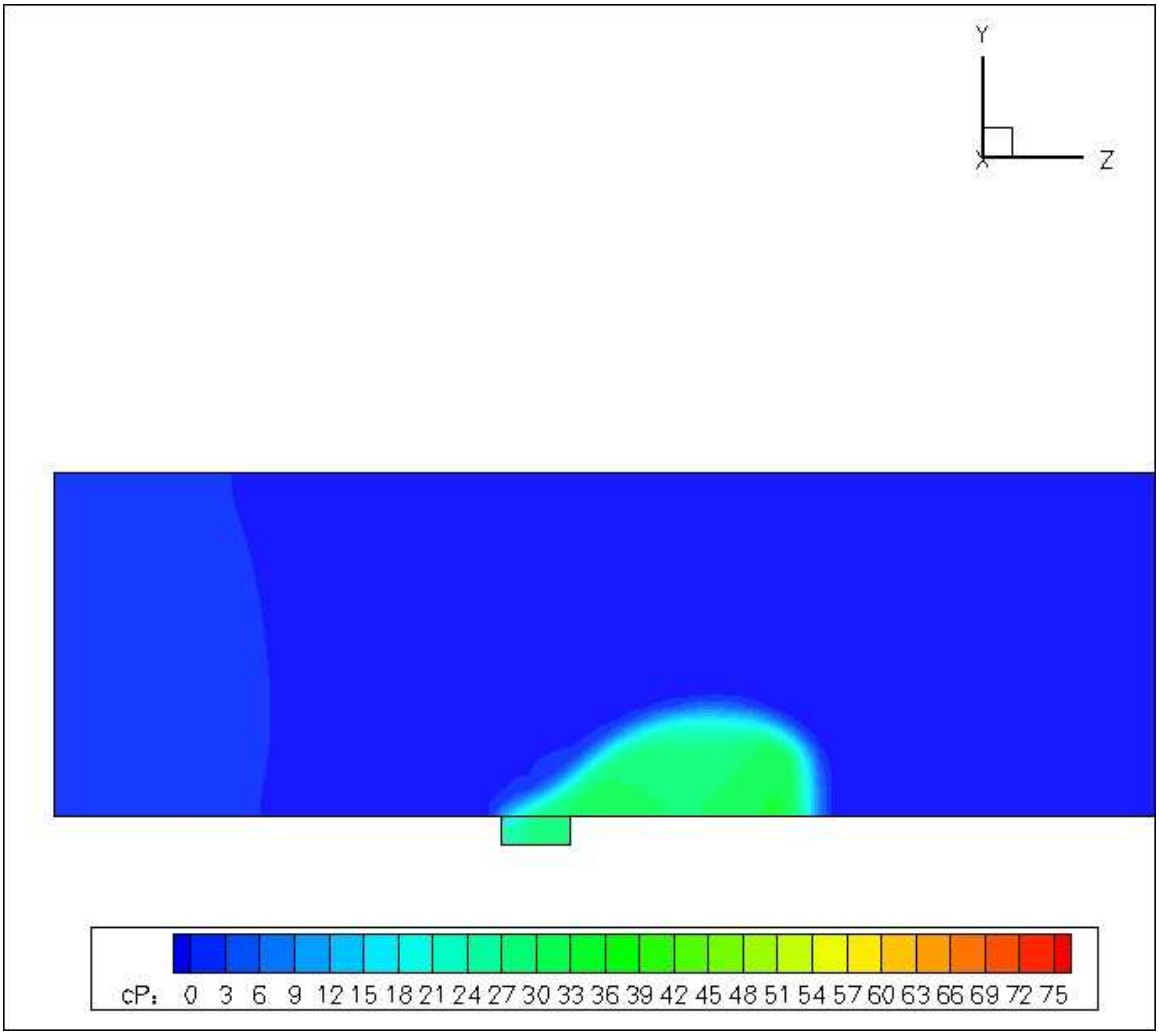

Figure 34: Pressure slice (in Pa) static contact angle, 4cm/s water injection, 10m/s air speed at a time of 3ms, water droplet emerging from a pore

The pressure plot in figure 34 shows the unbalanced pressure field around the detaching droplet. These pressure variations are not expected and are therefore non-physical defects of the static contact angle simulation. As the droplet detaches, the same pressure front remains at about a two thirds of the height of the droplet.

Figure 35 shows the phase boundary for the dynamic contact angle at the same time-step.

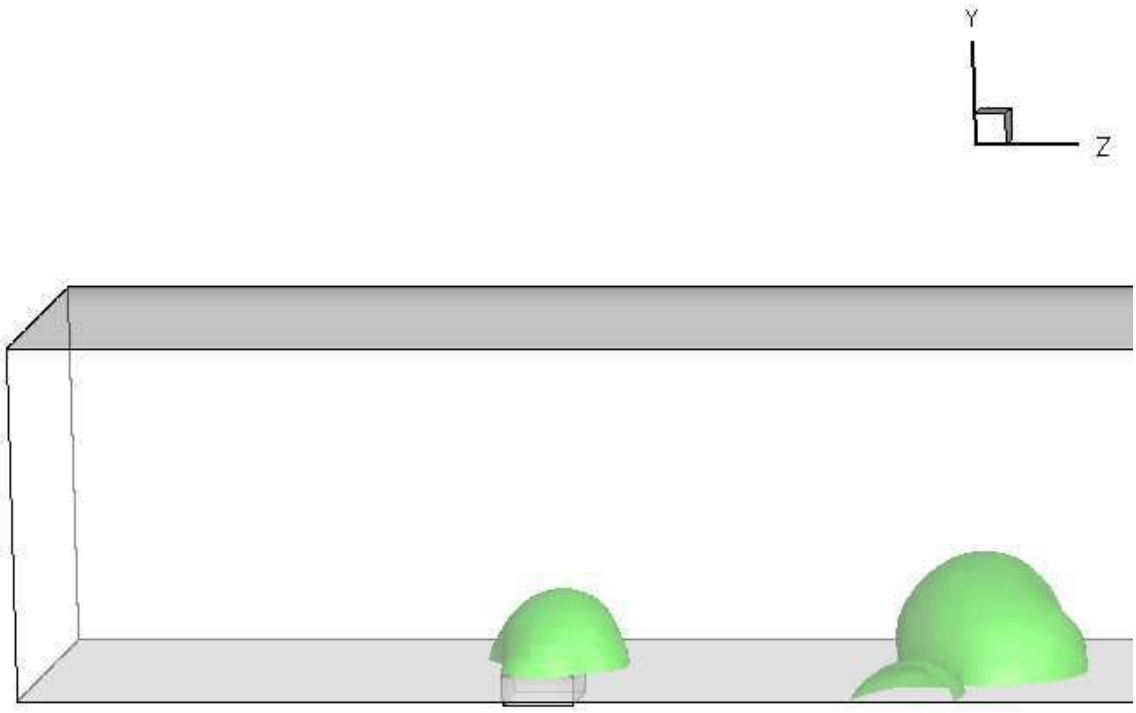

Figure 35: Phase boundary dynamic contact angle, 4cm/s water injection, 10m/s air speed at a time of 3 ms, water droplet emerging from a pore

The droplet has attached to the nearest side wall in figure 35. The different contact angles can still be seen between the leading and trailing edge. The droplet continues downstream moving with the erratic nature seen in the experiments. Figure 36 shows the pressure slice for the same conditions.

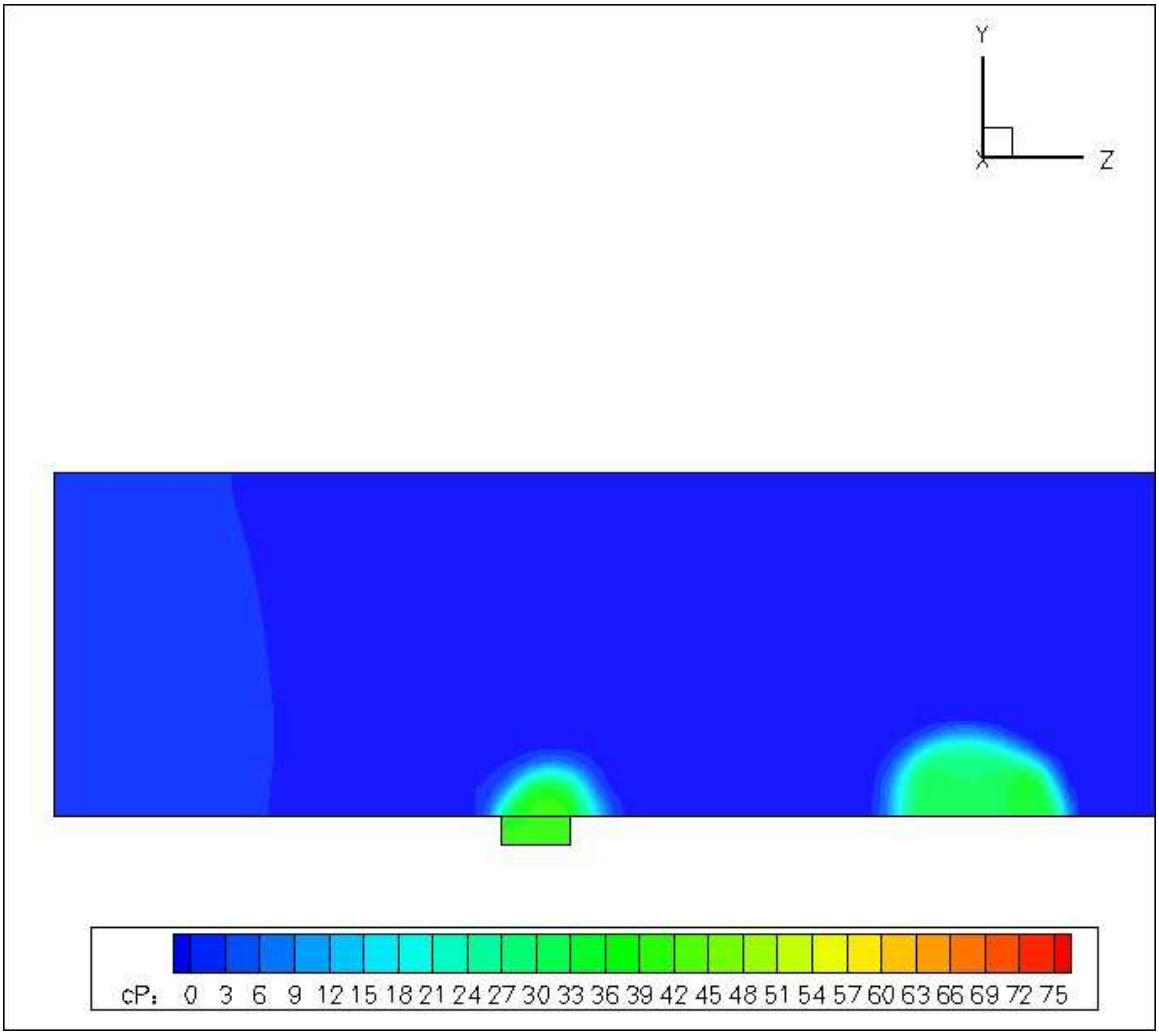

Figure 36: Pressure slice (in Pa) dynamic contact angle, 4cm/s water injection, 10m/s air speed a time of 3ms, water droplet emerging from a pore

The nearly constant pressure field within the droplet is clearly visible in figure 36. The pressure wave seen in the static case is not present in the plot.

The next step in comparing the static and dynamic contact angle is through pressure plotted along the centerline axis. The plane used for comparison runs down the channel length parallel with the sides of the flow channel. The plane is equidistant from both

sides of the channel and therefore runs down the center of the pore as well. The pressure plot for the static case is shown in figure 37.

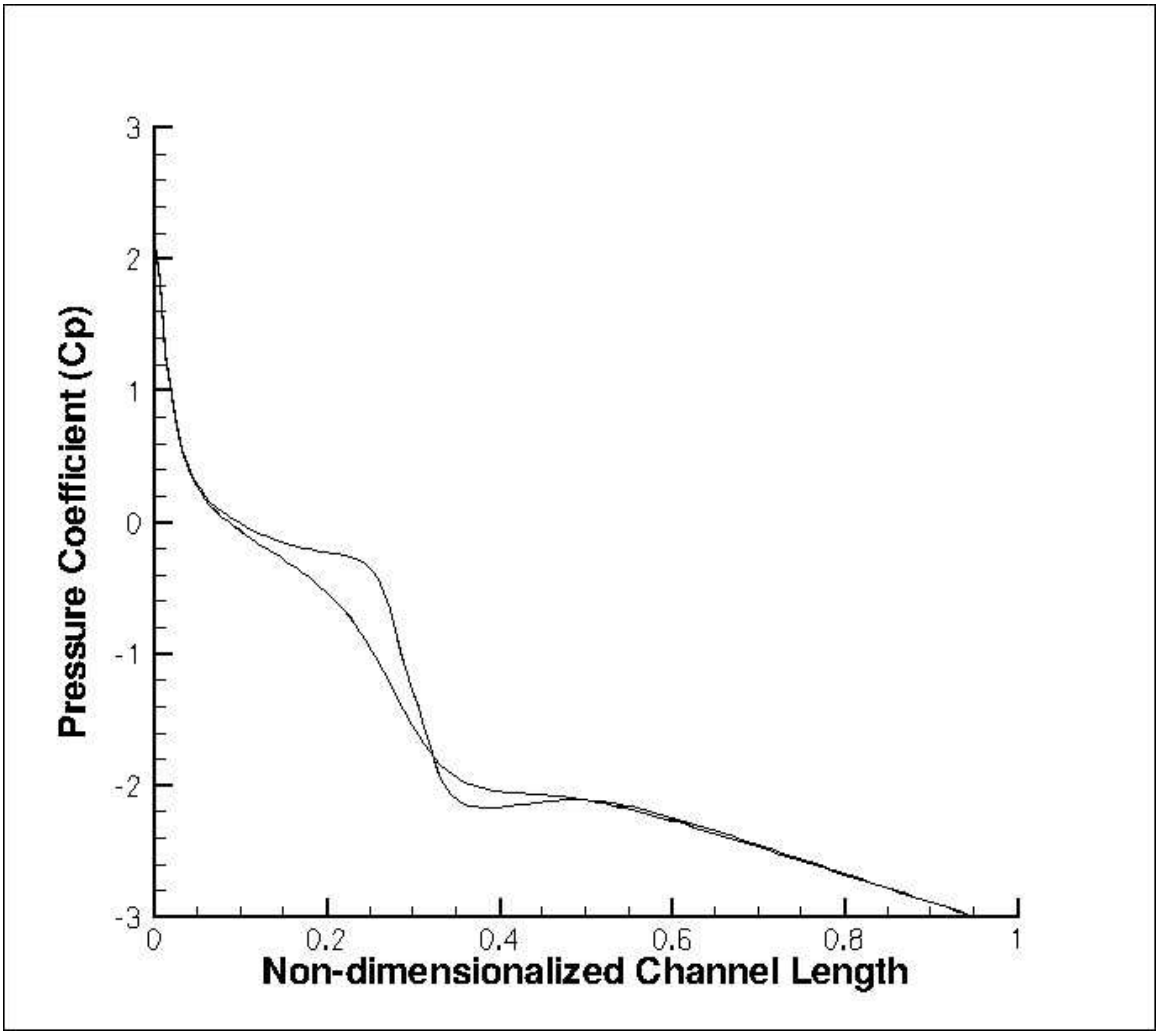

Figure 37: Pressure plot static contact angle, 4cm/s water injection, 10m/s air speed at a time of 3ms. The curves represent the max and min values.

The pressure plot is taken at three milliseconds, which corresponds to the droplet just being shed. The two lines in the pressure plot display the maximum and minimum value of the pressure in that slice. Note the s-bend shape in the pressure plot. This profile is not expected, as the pressure should jump substantially across the boundary of the

droplet. Figure 38 shows the pressure curve for the dynamic contact angle at the same boundary conditions.

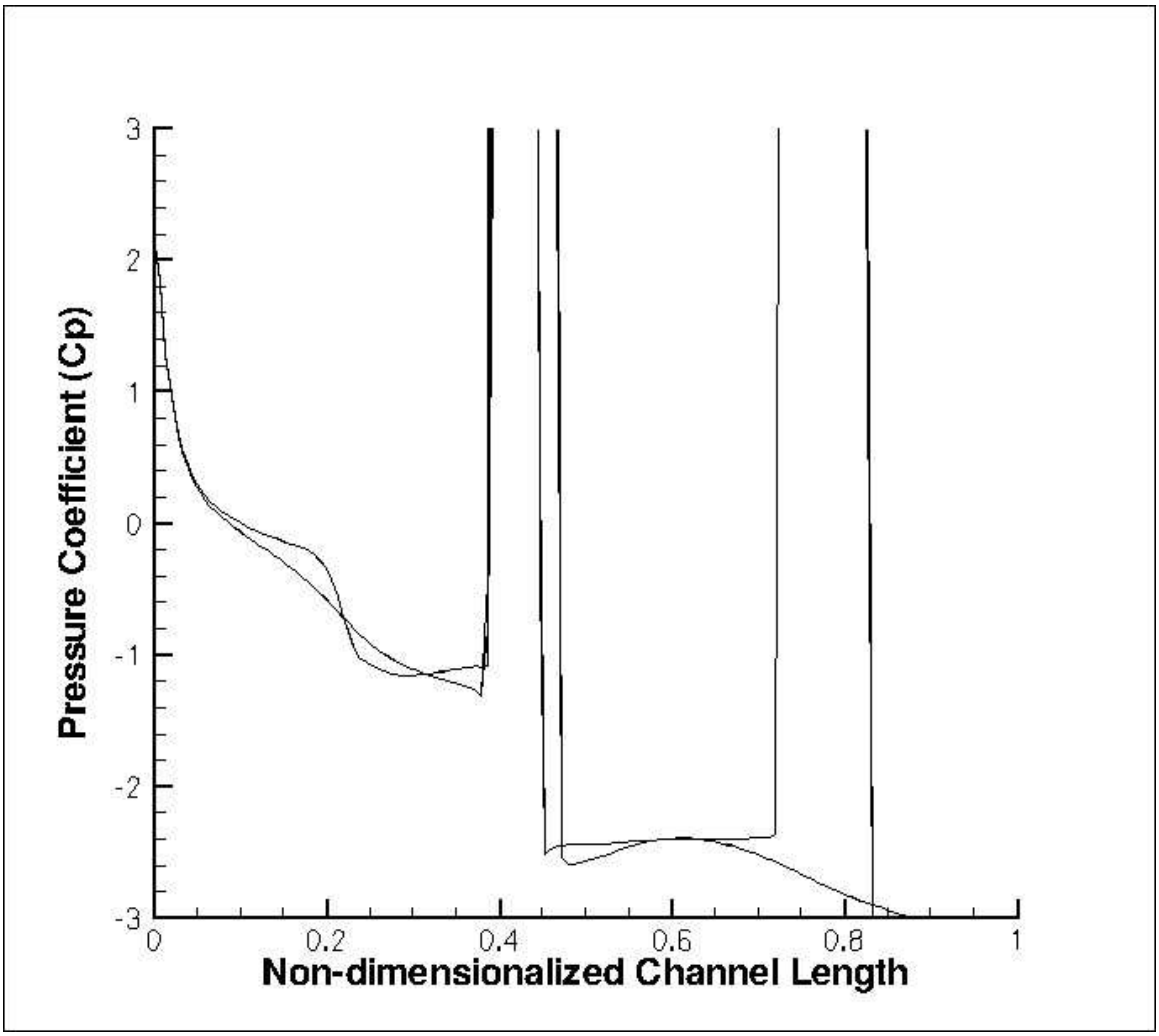

Figure 38: Pressure plot dynamic contact angle, 4cm/s water injection, 10m/s air speed at a time of 3ms. The two curves represent the max and min values.

The figure clearly shows the two pressure spikes expected. At three milliseconds the first droplet is moving downstream and the second droplet has emerged from the pore. This trend of large pressure variations at the droplets is more like the theory would suggest than the static contact angle plots. The dynamic contact angle model predicts a slightly

lower pressure drop of 330 Pa compared to the 350 Pa estimated by the static contact angle model. This lower pressure drop can be attributed to the more streamlined droplet shapes for the dynamic contact angle case.

The various plots show the advantages of the dynamic contact angle model as compared to the static contact angle for the first validation case.

4.2.3 Flow Channel Base Case Two

The second base case is similar to the first one, but has a slower water injection rate of V=0.02m/sec. The results are generally similar to those seen in the faster water injection rate. The static contact angle results in spherical droplet formation and shedding. The spherical growth can be seen in figure 39.

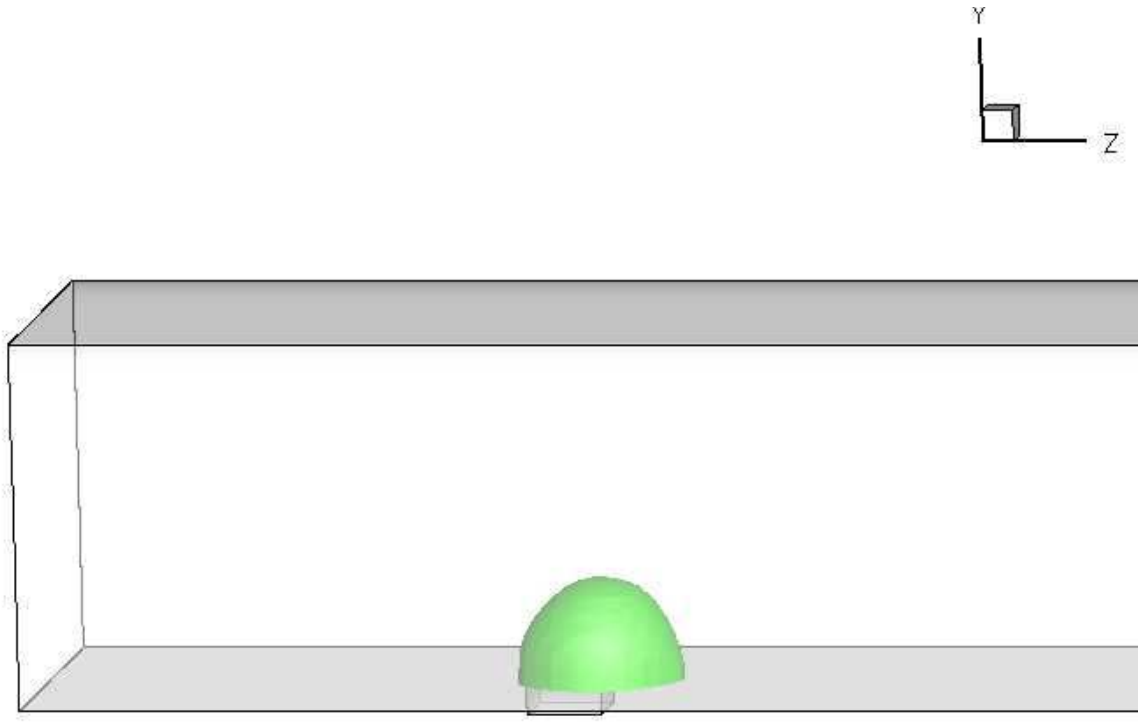

Figure 39: Phase boundary static contact angle, 2cm/s water injection, 10m/s air speed at a time of 2ms, water droplet emerging from a pore

It can be seen in figure 39 that the droplet grows up creating a near spherical shape despite the shear forces acting on the free surface of the droplet. The spherical shape is an artifact of the static contact angle as discussed in the previous section. The pressure plot for this same case is shown in figure 40.

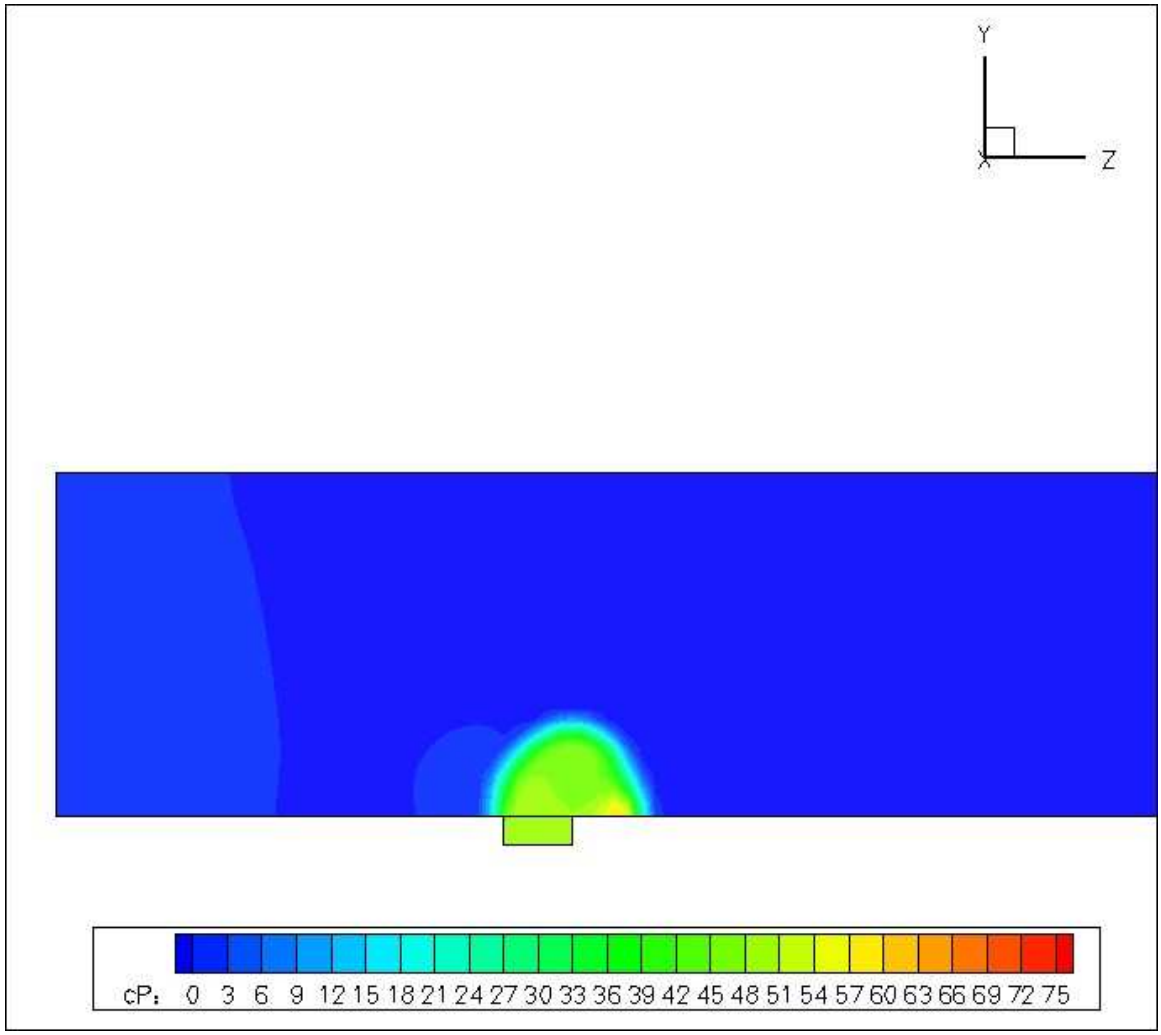

Figure 40: Pressure slice (in Pa) static contact angle, 2cm/s water injection, 10m/s air speed at a time of 2ms, water droplet emerging from a pore

The pressure irregularities within the droplet can be seen downstream of the pore. There is also a slight pressure wave upstream from the pore as the air contacts the growing

water droplet. Note also how the contact angle of the droplet is the same for the leading and trailing edge of the droplet.

The dynamic contact angle formulation results in a more realistic water droplet evolution. The phase boundary can be seen in figure 41.

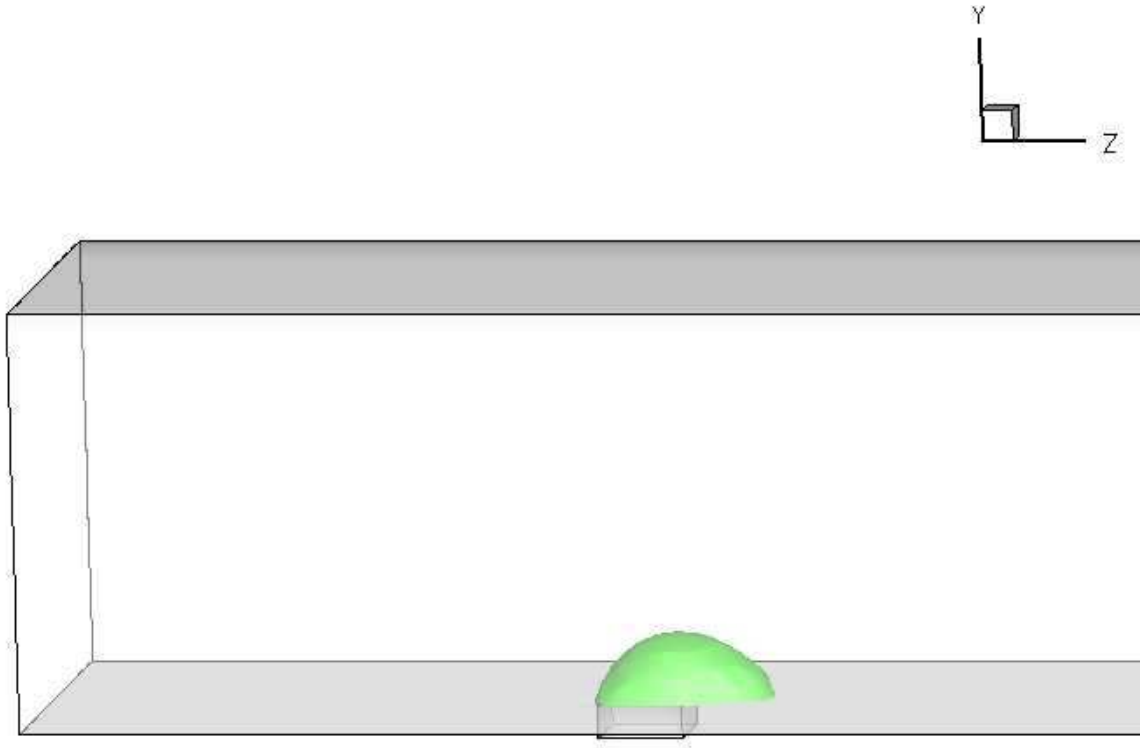

Figure 41: Phase boundary dynamic contact angle, 2cm/s water injection, 10m/s air speed at a time of 2ms, water droplet emerging from a pore

Comparing figures 39 and 41, the dynamic contact angle model produces a more elongated droplet that is evolving in the downstream direction. The leading edge sees a higher (advancing) contact angle as the contact line velocity increases, creating the more realistic droplet movement. The pressure plot for this same case is shown in figure 42.

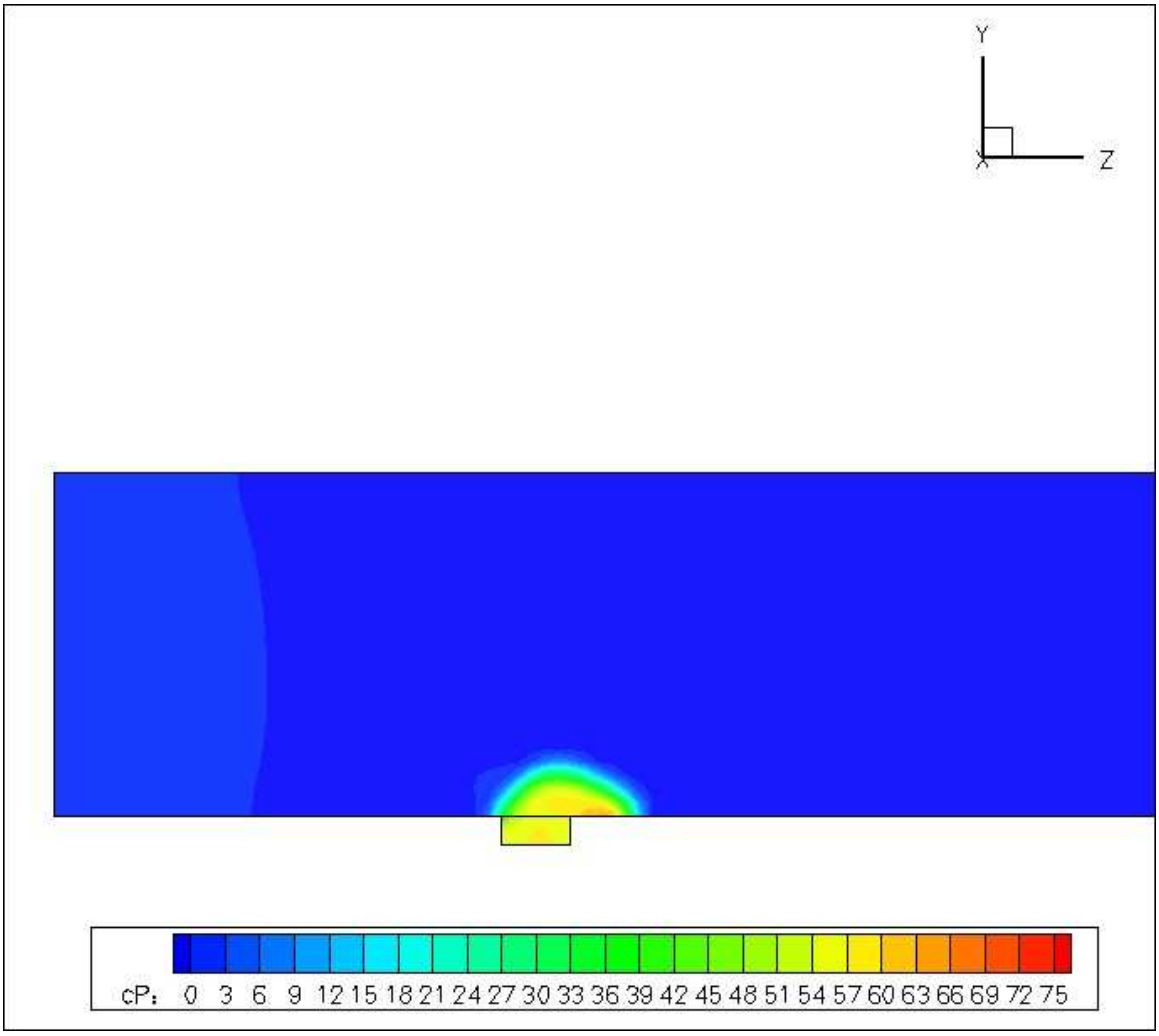

Figure 42: Pressure plot (in Pa) dynamic contact angle, 2cm/s water injection, 10m/s air speed a time of 2ms, water droplet emerging from a pore

Comparing figures 40 and 42 it can be observed that the pressure rise upstream of the droplet is smaller and the pressure distribution within the droplet is more uniform. The droplet shape is therefore closer to its equilibrium due to the more uniform pressure, consistent with a better droplet shape development.

These trends continue as the time evolves. The pressure plots will not be repeated for the following time steps because they show the same trends as the first time step as well as the first base case.

For further verification the droplets are analyzed at the point at which the droplet detaches from the pore and continues downstream. Figure 43 shows the phase boundary slightly after droplet detachment.

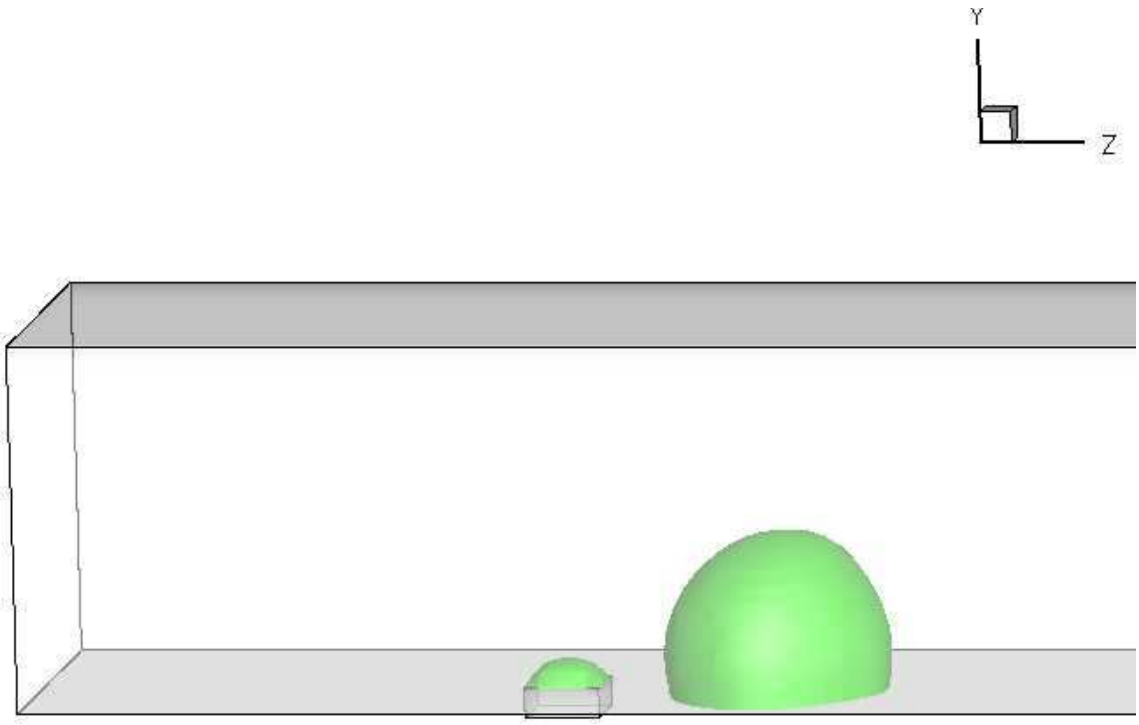

Figure 43: Phase boundary static contact angle, 2cm/s water injection, 10m/s air speed at a time of 3.2ms, water droplet emerging from a pore

Note how the droplet separates completely from the pore and flows downstream in a nearly spherical form. Figure 44 shows the dynamic contact angle model at the same time step.

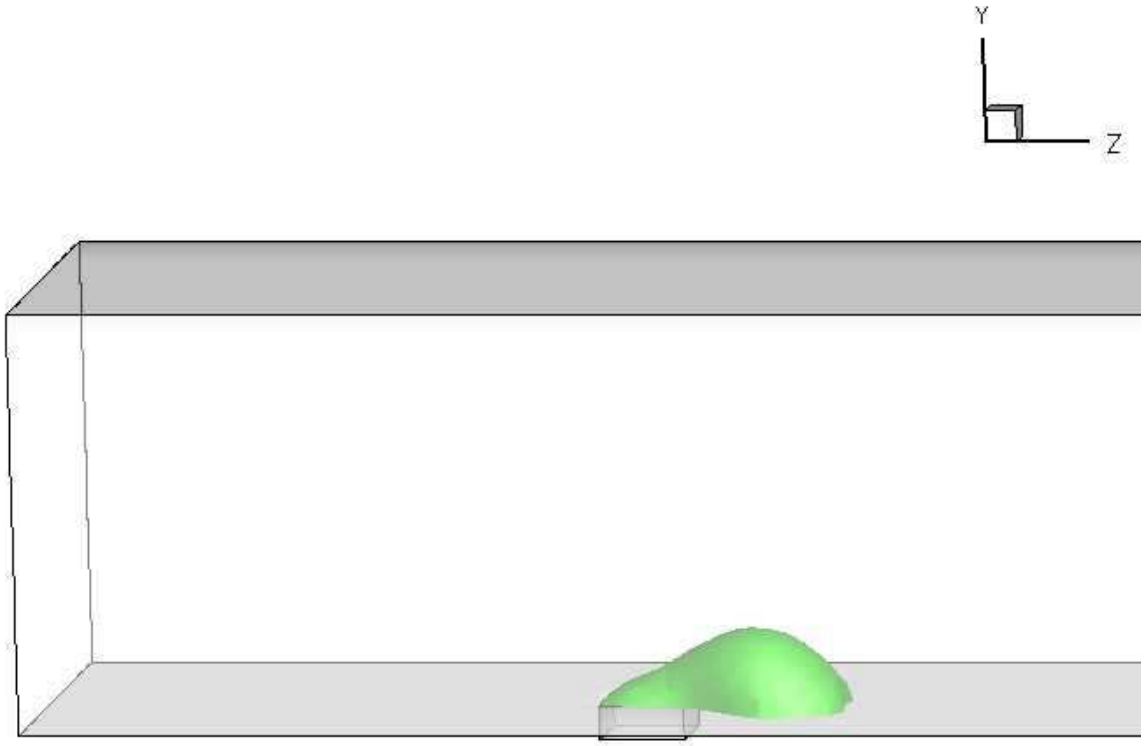

Figure 44: Phase boundary dynamic contact angle, 2cm/s water injection, 10m/s air speed at a time of 3.2ms, water droplet emerging from a pore

The droplet forms a tail as it separates from the pore. The main droplet has a similar profile as a droplet falling in freefall, as it separates with a rounded head and a tapered body indicative of strong shear force effects induced by the air flow. When comparing figures 43 and 44 the difference is clearly visible. The elongated droplet at the time of shedding is consistent with the trend seen in experimental data, again proving the advantage of the dynamic contact angle formulation.

The final phase boundary comparison, at the above stated boundary conditions, for static versus dynamic contact angle is shown at a further time step. Figure 45 shows the static case at 5ms where an interesting phenomenon arises.

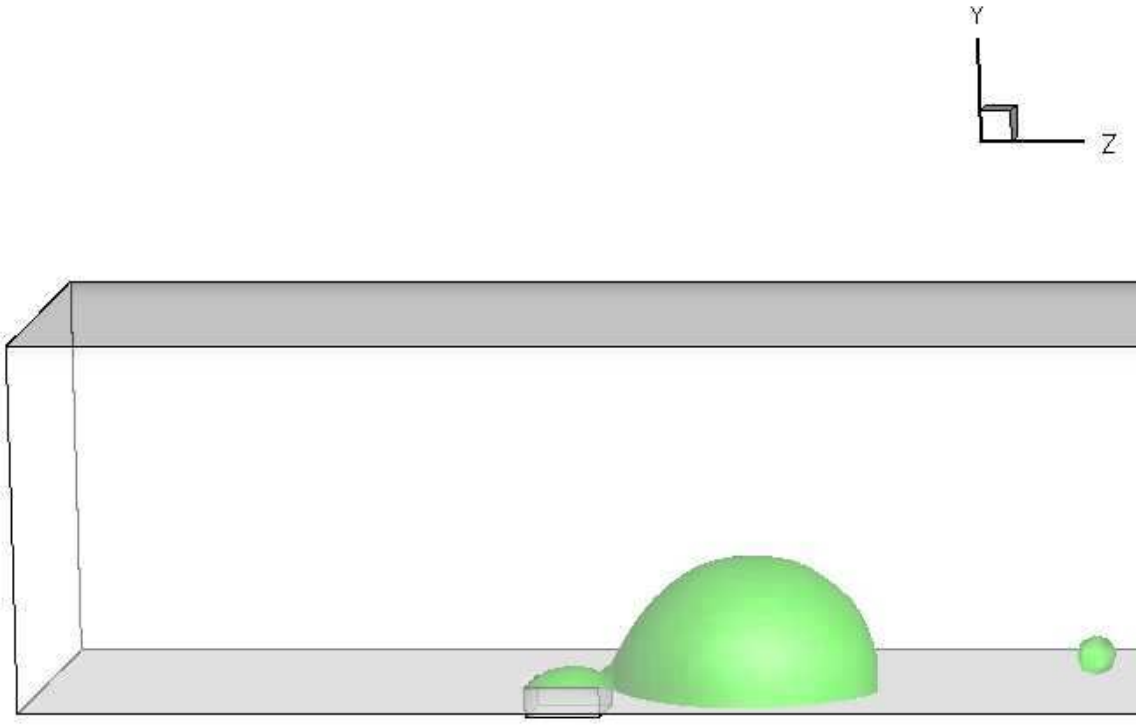

Figure 45: Phase boundary static contact angle, 2cm/s water injection, 10m/s air speed at a time of 5ms, water droplet emerging from a pore

This time step shows the static case just as the droplet detaches for the second time. Note the floating small spherical droplet further downstream. This floating droplet is common in static contact angle volume of fluid simulations. It is a result of the lift over the nearly spherical body shape and the rigid nature of the implementation of the static contact angle. Figure 46 shows the dynamic contact angle model at the same time step.

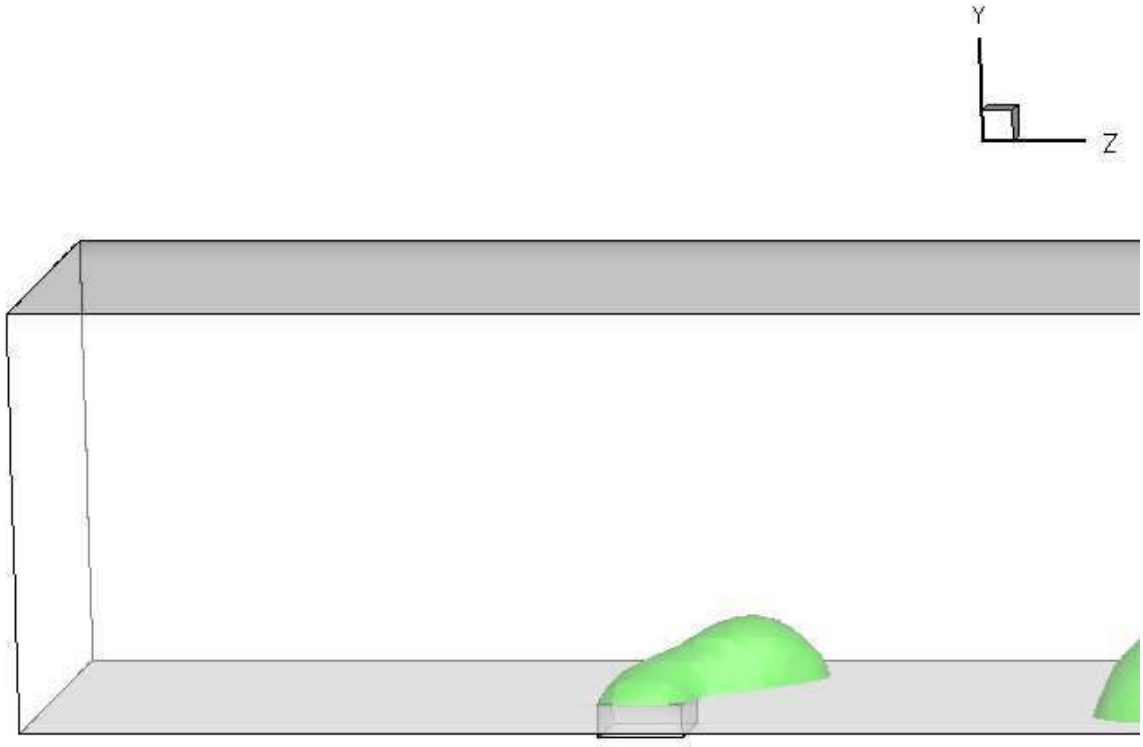

Figure 46: Phase boundary dynamic contact angle, 2cm/s water injection, 10m/s air speed at a time of 5ms, water droplet emerging from a pore

Note the downstream droplet is fully attached and the upstream droplet is elongated, again as experimental data would suggest. Looking at pressure plots as the droplets detach and move downstream in the channel will provide the next method of comparison. Figure 47 shows the downstream pressure profile at a time of one millisecond.

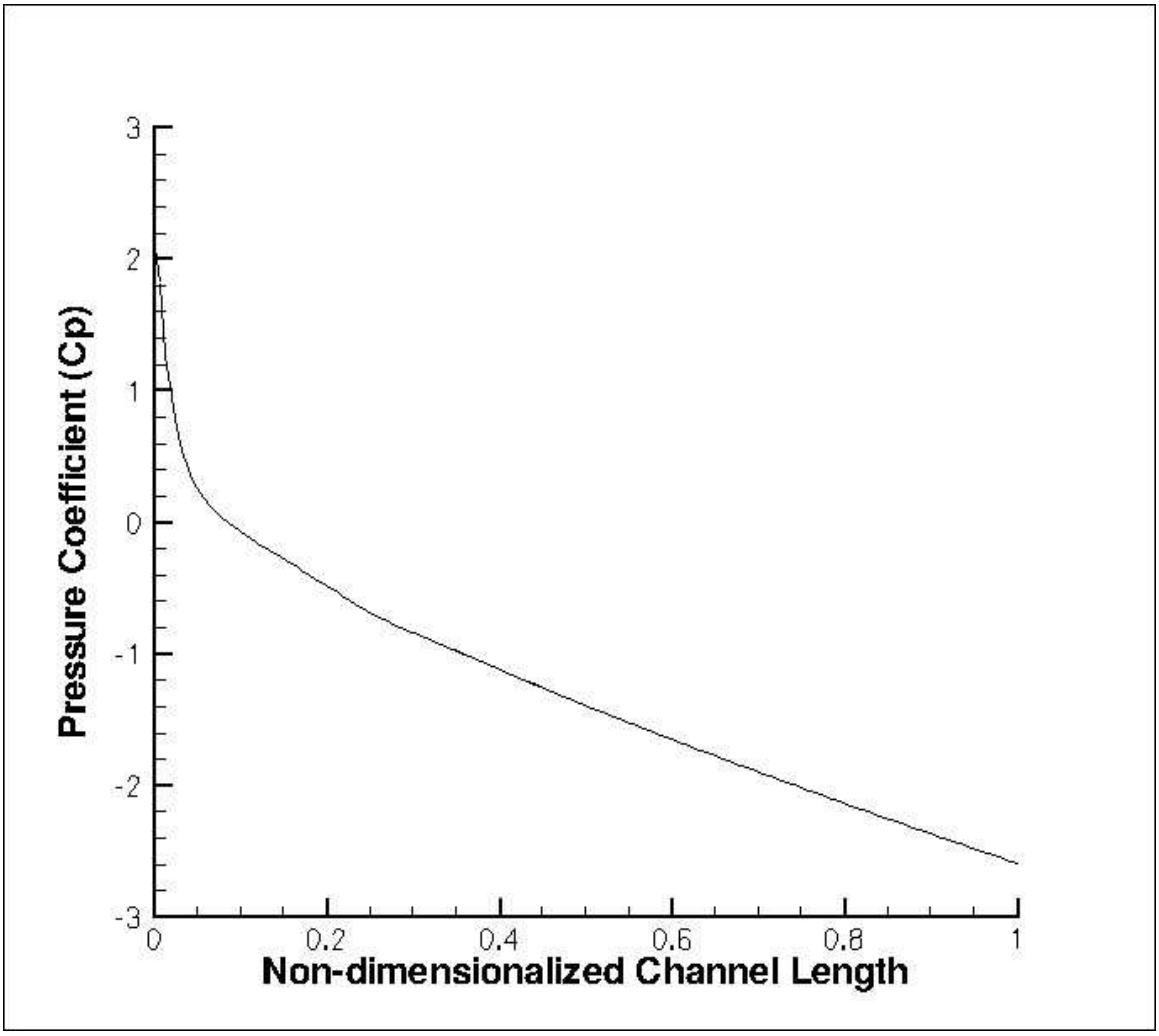

Figure 47: Pressure plot static contact angle, 2cm/s water injection, 10m/s air speed at a time of 1ms.

This plot correlates to single phase flow in a channel and gives an indication of what the pressure profile is like in a channel without a droplet forming. Figure 48 shows the same time step, but is for the dynamic contact angle model.

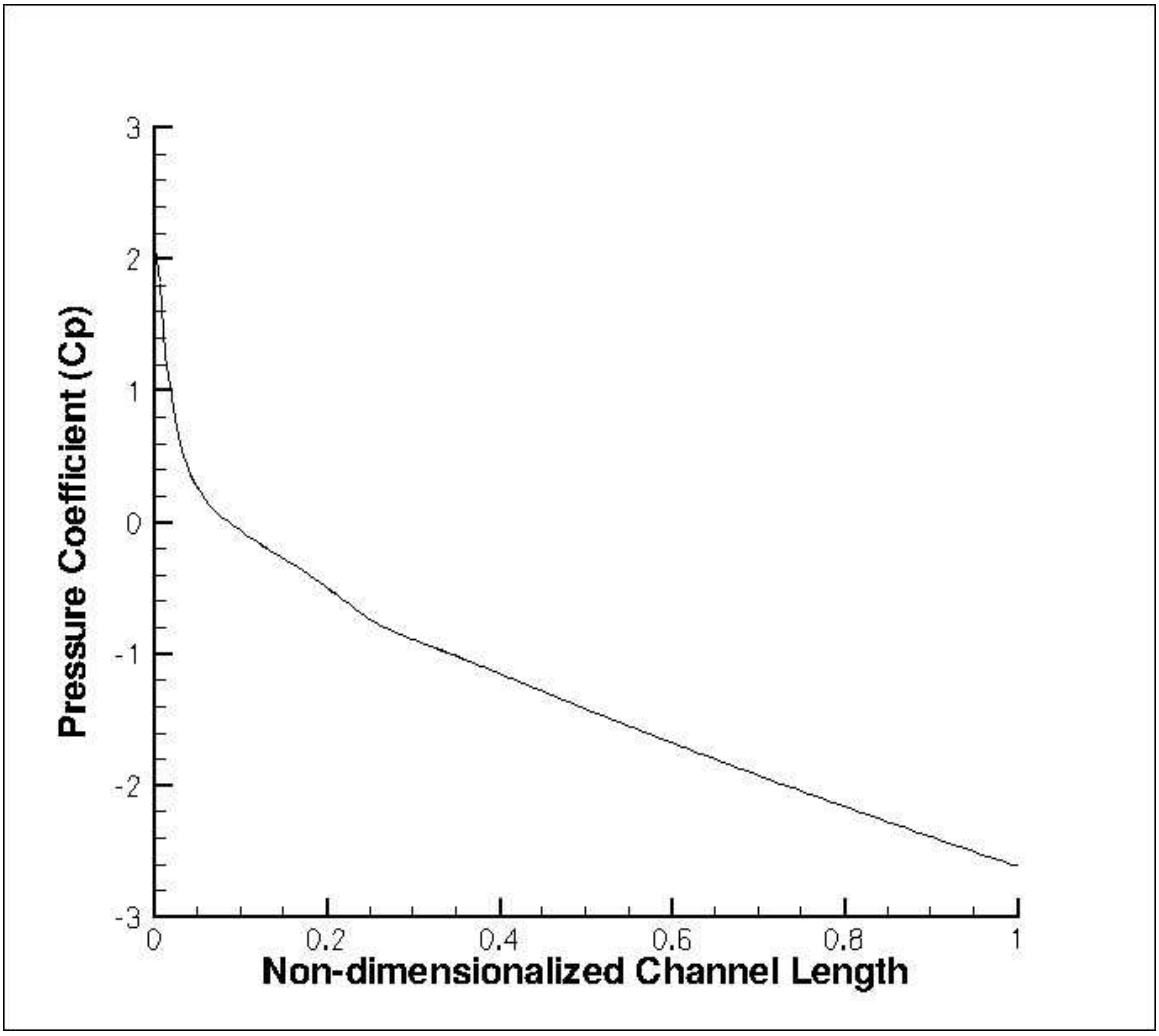

Figure 48: Pressure plot dynamic contact angle, 2cm/s water injection, 10m/s air speed at a time of 1ms.

It can be seen by comparing figures 47 and 48 that the dynamic contact angle code does not disturb the pressure field in the absence of liquid water droplets. This is to be expected as the code is not supposed to have any effect on the airflow besides modifying the droplet shape by altering the contact angle. Therefore, the dynamic contact angle code does not display unwanted effects on the remaining flow field.

To look at the effect of the dynamic contact angle implementation as compared to the static contact angle the pressure plots were observed at the point just before the droplet detaches. Figure 49 shows the pressure plot for the static contact angle model.

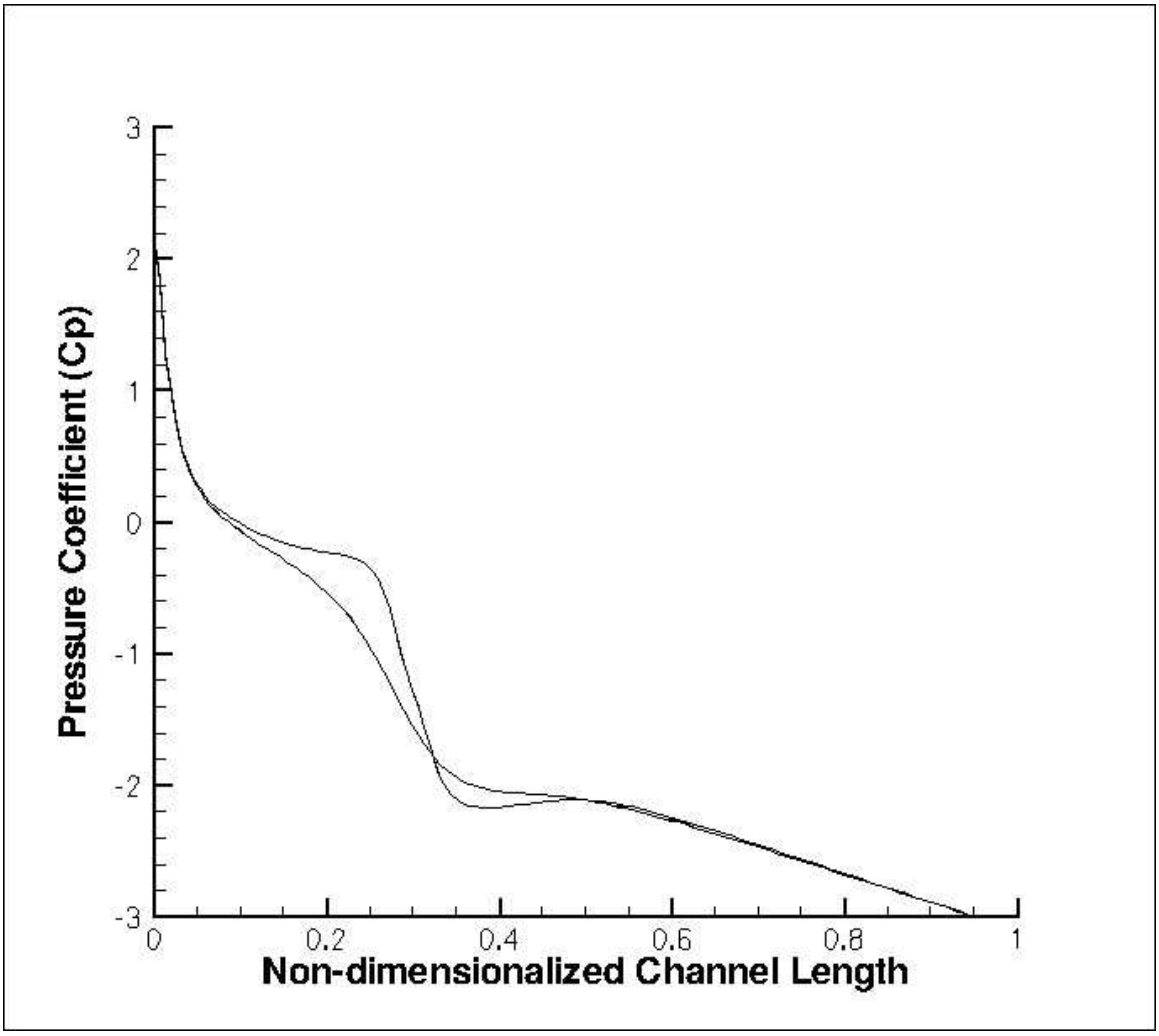

Figure 49: Pressure plot static contact angle, 2cm/s water injection, 10m/s air speed at a time of 3ms.

The two curves represent the maximum and minimum pressure values in the centerline plane as described earlier. Note the s-bend curve created at the location of the droplet. This trend is not what would be expected as the pressure is observed slicing through the droplet. The pressure should spike sharply at the droplet interface due to the surface

tension. Figure 50 shows the pressure plot for the dynamic contact angle model at the same conditions.

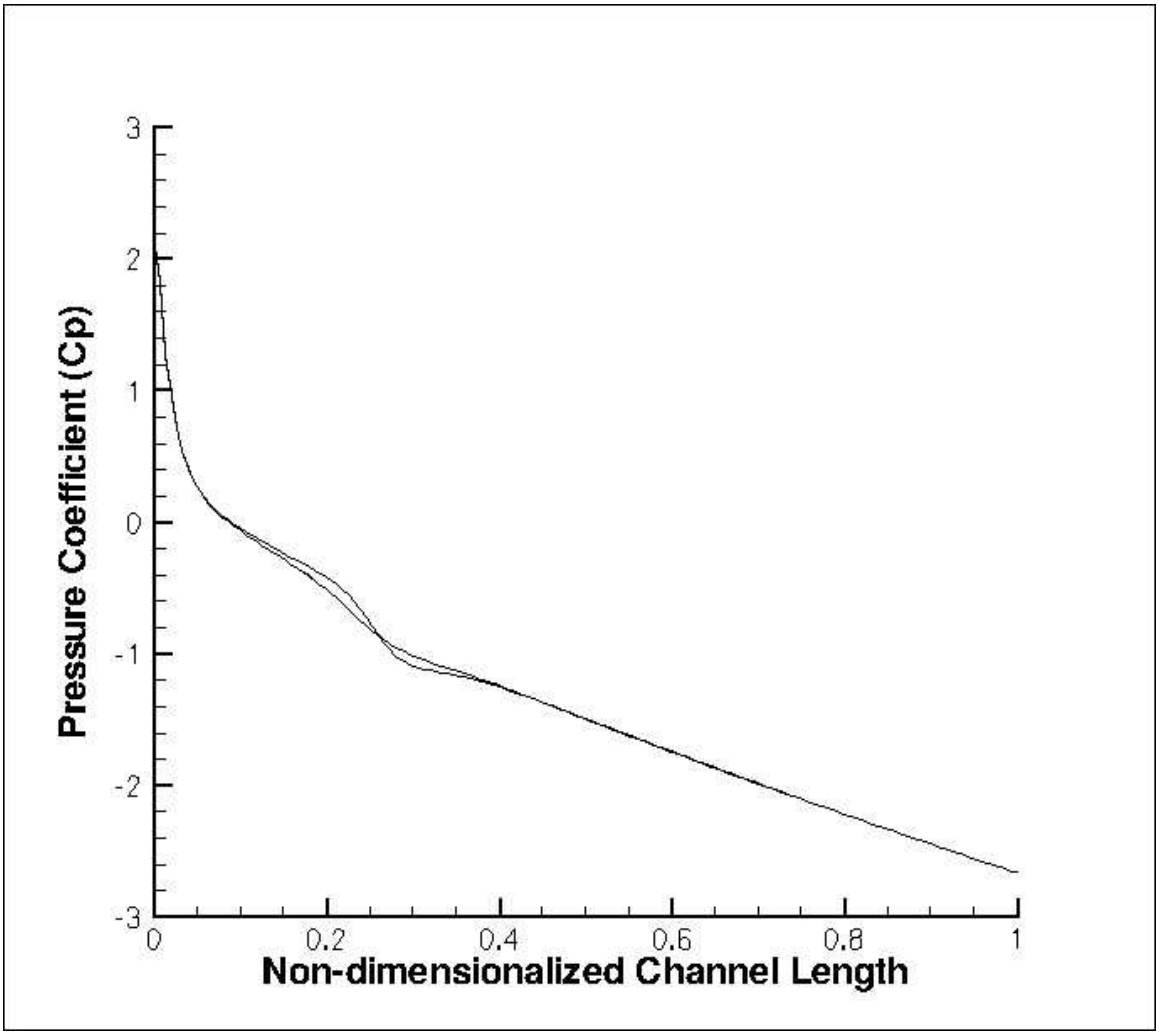

Figure 50: Pressure plot dynamic contact angle, 2cm/s water injection, 10m/s air speed at a time of 3ms.

The clearly identifiable pressure spike is present in the plot. This is the pressure jump as the phase boundary is crossed. The total predicted pressure drop for the dynamic case is again lower than the static case at 285 Pa and 310 Pa respectively.

As in the first base case the data in the second validation case indicate that the dynamic contact angle model provides better agreement with the actual fluid dynamics.

4.2.4 Flow Channel Base Case Three

The third base case has a slower air speed as well as a slower water injection velocity. The third case uses an air speed U= 4m/sec and a water injection velocity V=0.01m/s. This case will test the model for fuel cell operating conditions leading to flooding. The water droplet at this low air velocity grows in the same manner as the higher air speeds but grows to much larger proportions. The droplet at two milliseconds can be seen in figure 51.

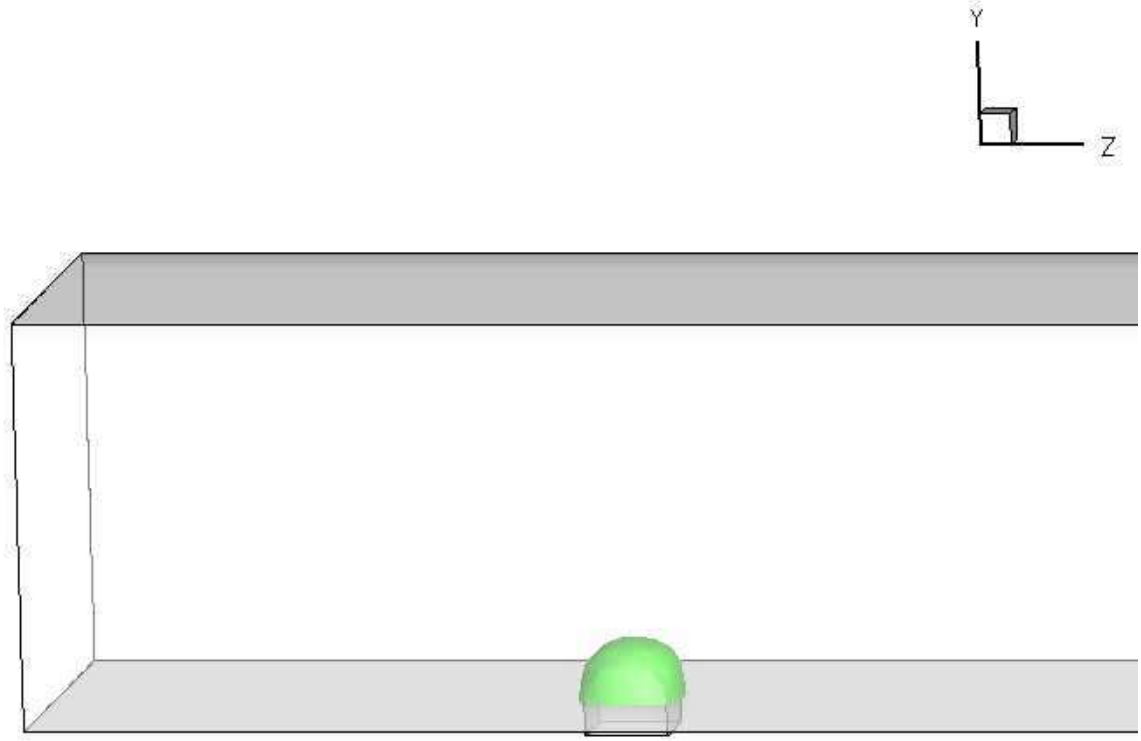

Figure 51: Phase boundary static contact angle, 1cm/s water injection, 4m/s air speed at a time of 2ms, water droplet emerging from a pore

Again the droplet displays the clear spherical shape as it grows from the pore. The pressure plot for this time-step can be seen in figure 52.

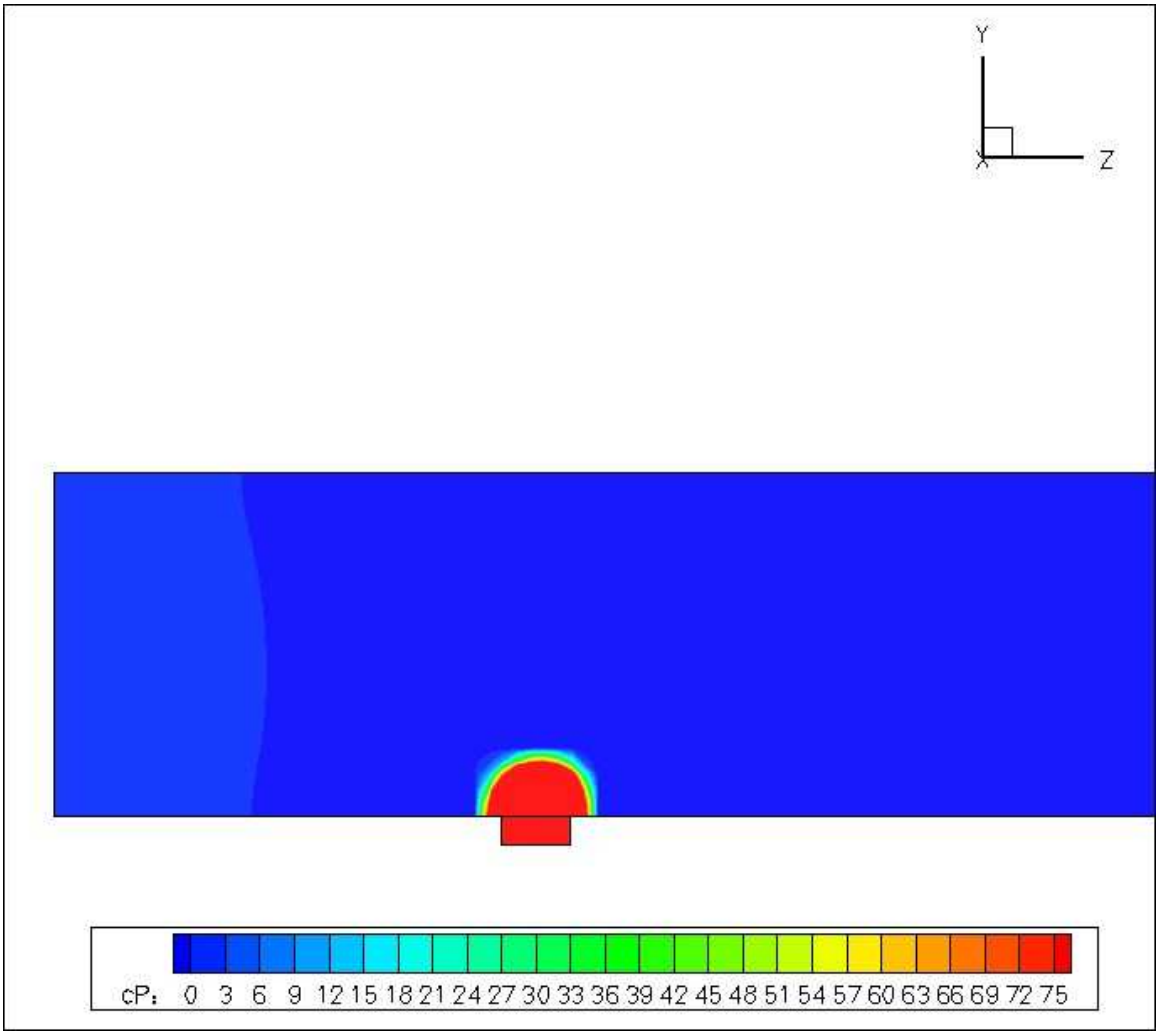

Figure 52: Pressure slice (in Pa) static contact angle, 1cm/s water injection, 4m/s air speed at a time of 2ms, water droplet emerging from a pore

The pressure plot shows pressure oscillations on the leading and trailing edges of the droplet as well as large pressure differentials within the droplet.

In order to provide a comparison the phase boundary for the dynamic contact angle can be seen in figure 53.

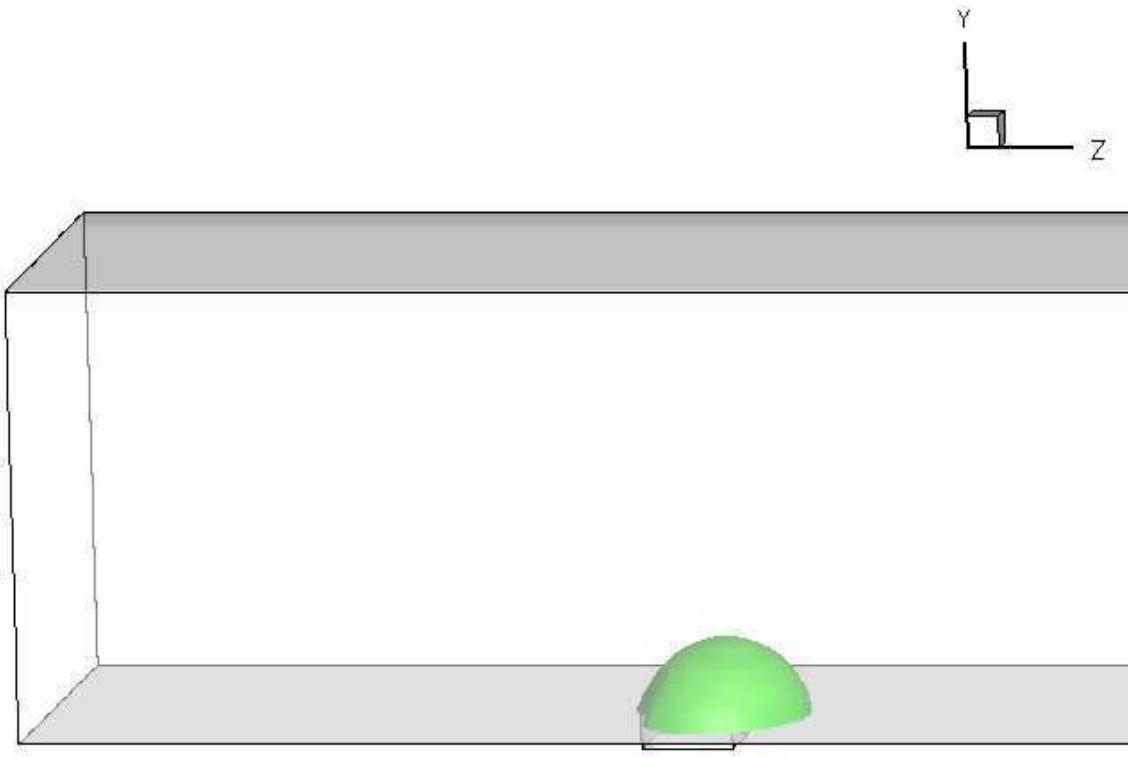

Figure 53: Phase boundary dynamic contact angle, 1cm/s water injection, 4m/s air speed at a time of 2ms, water droplet emerging from a pore

The droplet forms the elongated shape almost immediately, as seen in the other two base cases. The pressure varies in a more uniform and monotonic manner as seen in figure 54.

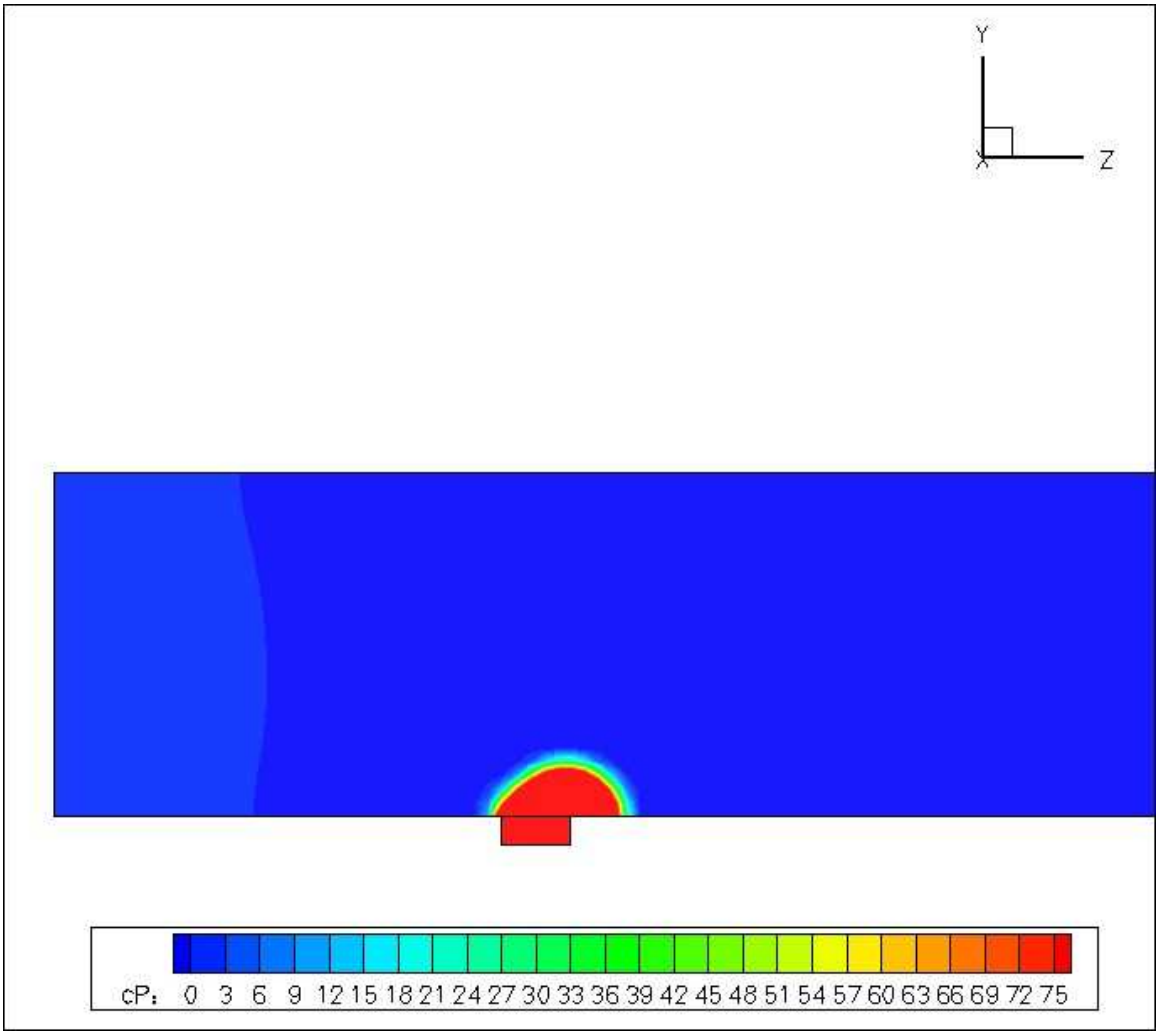

Figure 54: Pressure slice (in Pa) dynamic contact angle, 1cm/s water injection, 4m/s air speed at a time of 2ms, water droplet emerging from a pore

The pressure within the droplet is more uniform than that seen in the static case, shown in figure 52. There is no pressure oscillation around the droplet or a rising pressure field within the pore. Pressure plots for later time steps show the same trend, and for brevity will be omitted for the remainder of the third base case.

Next the models are evaluated at ten milliseconds when the channel is flooded with water. The phase boundary for the static case is seen in figure 55.

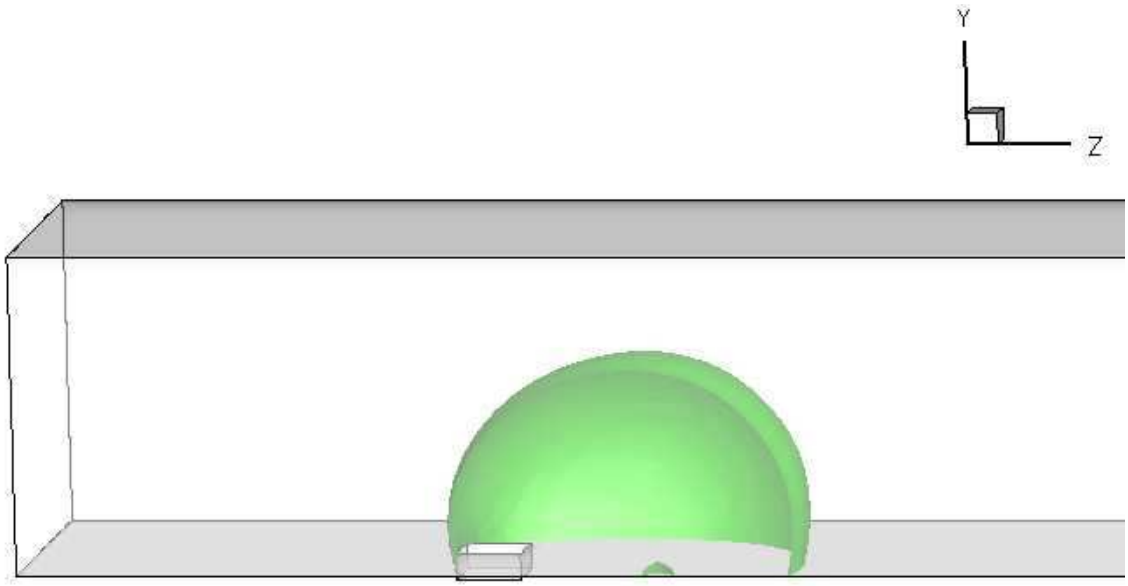

Figure 55: Phase boundary static contact angle, 1cm/s water injection, 4m/s air speed at a time of 10ms, water droplet emerging from a pore

Even at the point of flooding in the channel the droplet still maintains its quasi-spherical shape. The dynamic contact angle model does not produce this shape, as shown in figure 56.

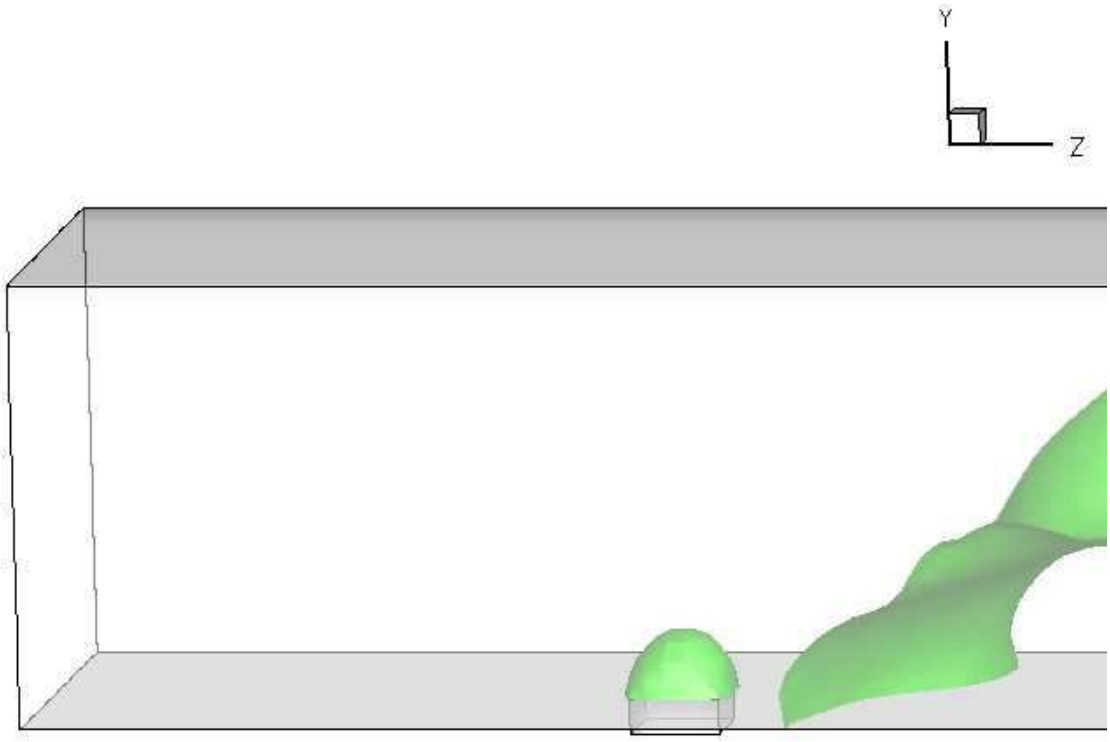

Figure 56: Phase boundary dynamic contact angle, 1cm/s water injection, 4m/s air speed at a time of 10ms, water droplet emerging from a pore

The flooding water produces a saddle shape as it moves through the channel. This trend is congruent with experimental trends, where flooding creates a coating across the surface instead of very large spherical droplets. The droplet at the point of detachment for the static contact angle is seen in figure 57.

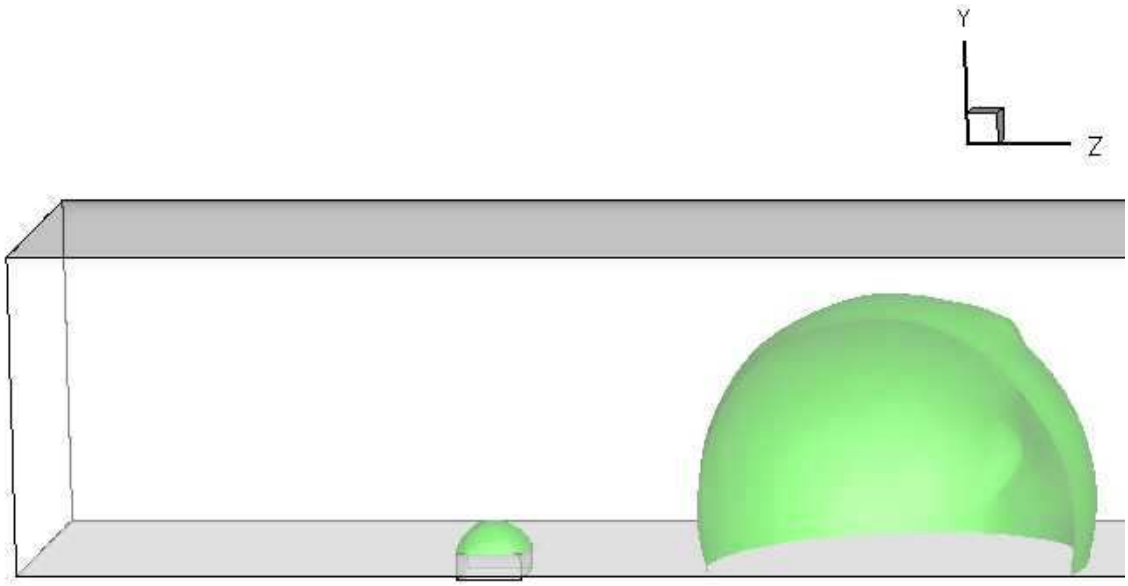

Figure 57: Phase boundary static contact angle, 1cm/s water injection, 4m/s air speed at a time of 13ms, water droplet emerging from a pore

The spherical shape is quite noticeable in figure 57, and is not realistic, showing again the need of a dynamic contact angle model.

Each of the three base cases has shown the droplet evolution and shedding from the pore. In each case, static contact angle simulations result in quasi-spherical droplets and, at times, lifting off and floating from the surface. The dynamic contact angle model, on the other hand, results in elongated droplets that remain attached to the surface. The pressure plots and curves both show unrealistic pressure profiles with the static contact angle, whereas the dynamic contact angle model provides trends matching expectations and available observations. Having established the improved physical representation resulting from the dynamic contact angle model, parametric studies are next presented for the three model inputs.

4.3 Effect of Air Speed

All simulations presented here and in the next two sections are performed using the dynamic contact angle model. The first parameter evaluated is the effect of air speed on the droplet evolution. The air speed into the flow channel is one of the most commonly used tools in the fuel cell designer's toolbox for dealing with water management in a fuel cell. Higher airflow should result in smaller droplet sizes and more frequent shedding. The higher airflow comes at the cost of increased system requirements due to the larger pressure drops, including parasitic losses, in the channel and the higher pumping volume. The two cases to be examined have a static contact angle of 110 degrees and a water injection velocity V=0.02m/sec. The first case uses an air V=10m/sec where the second case uses V=4.4m/sec. The phase boundary for the first case can be seen in figure 58.

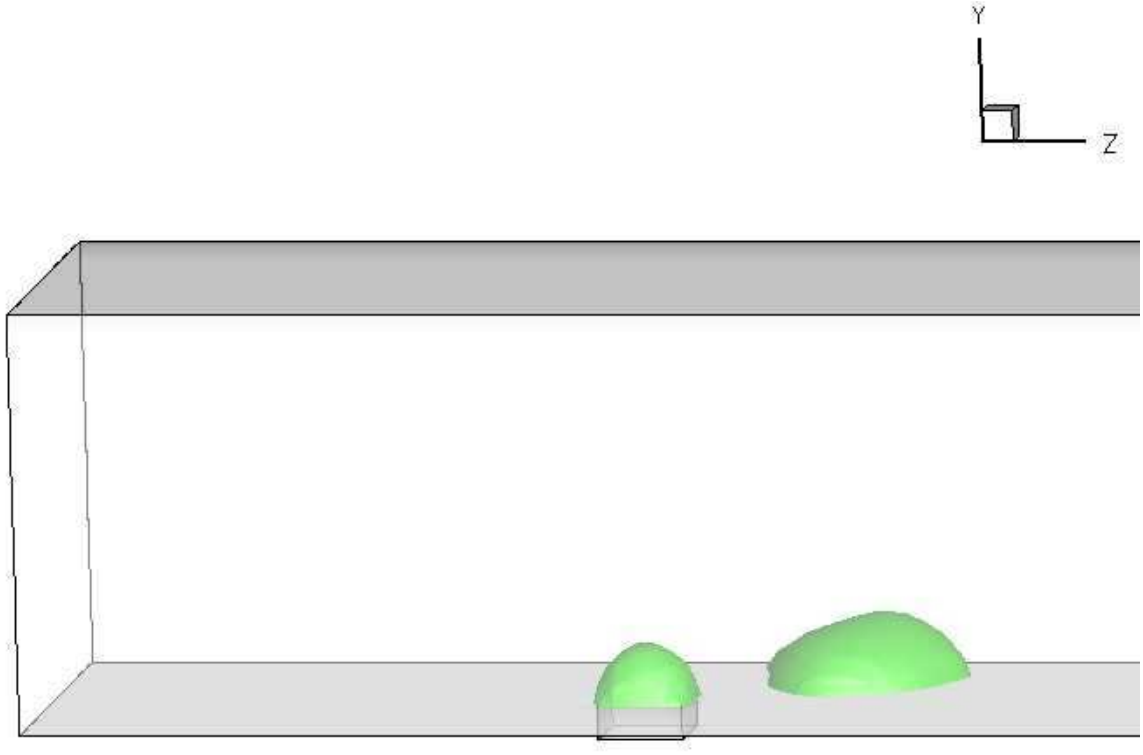

Figure 58: Phase boundary, 2cm/s water injection, 10m/s air speed at a time of 4ms, water droplet emerging from a pore

The phase boundary for the second case, with the lower air speed, is shown in figure 59.

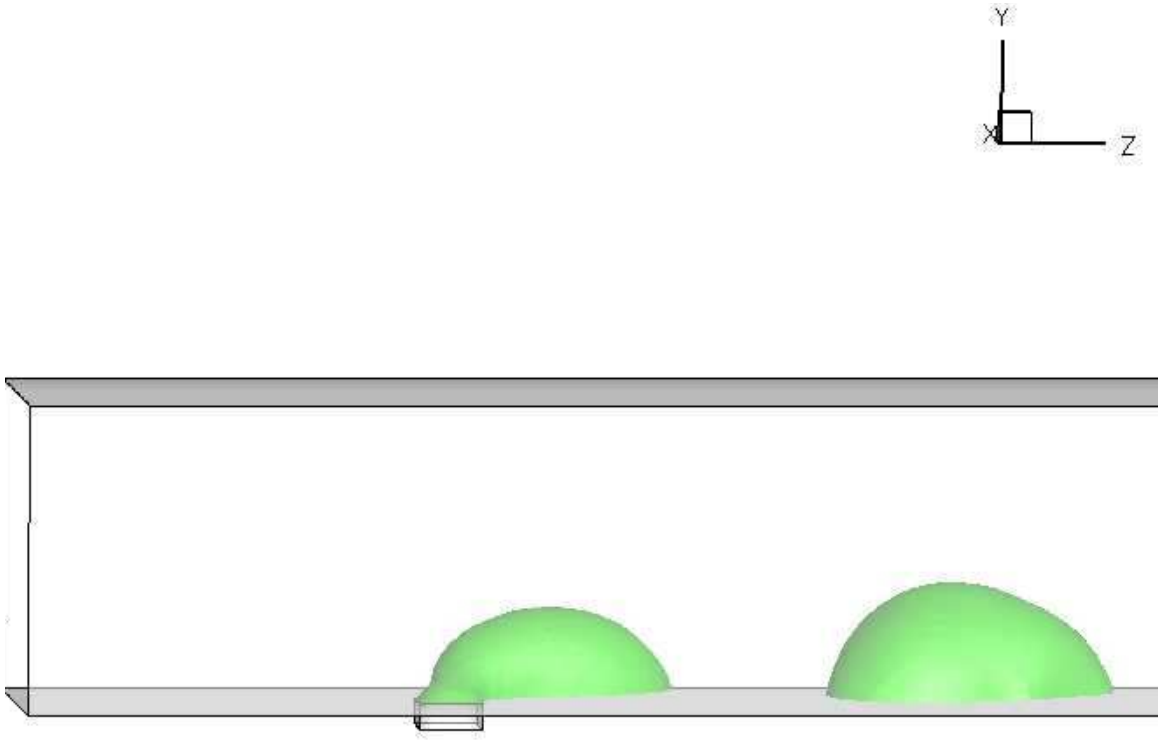

Figure 59: Phase boundary, 2cm/s water injection, 4.4m/s air speed at a time of 4ms, water droplet emerging from a pore

When comparing figures 58 and 59 the effect of the air velocity can clearly be seen. The lower air velocity results in droplet approximately double in size of those produced at the higher air velocity. To further illustrate the differences between the two air velocities, a later time step is examined. Figures 60 and 61 show the two cases at five milliseconds.

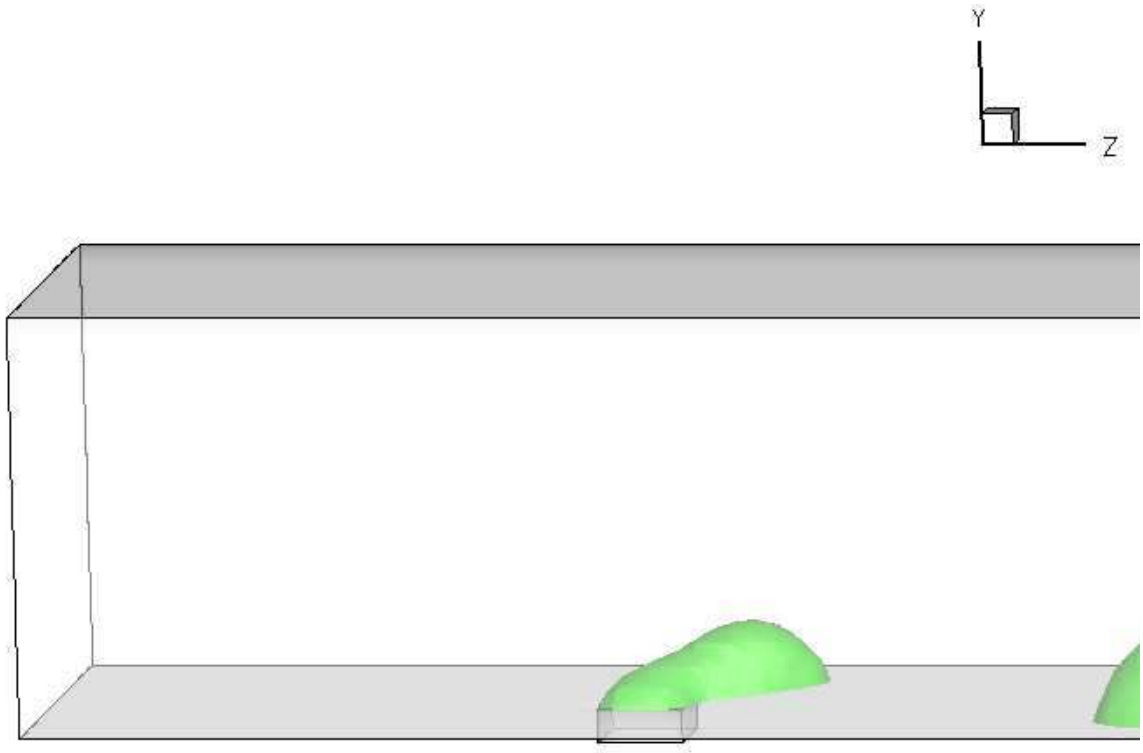

Figure 60: Phase boundary, 2cm/s water injection, 10m/s air speed at a time of 5ms, water droplet emerging from a pore

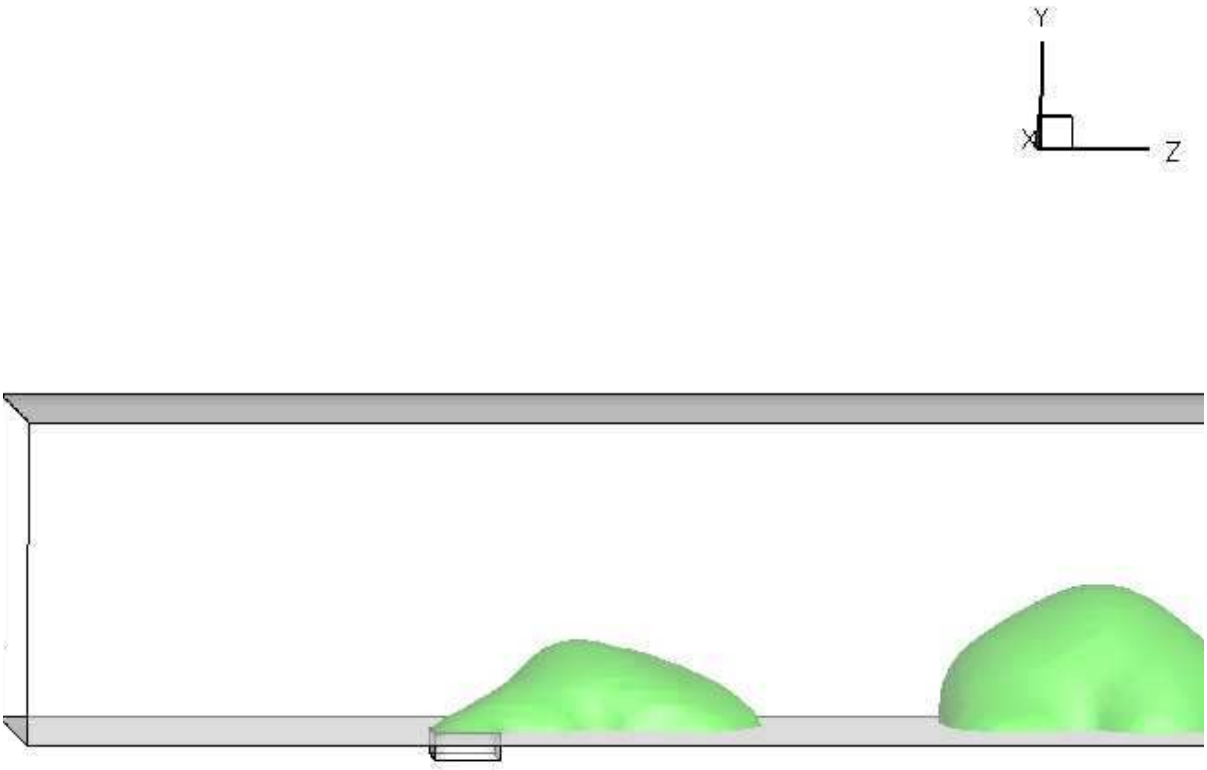

Figure 61: Phase boundary, 2cm/s water injection, 4.4m/s air speed at a time of 5ms, water droplet emerging from a pore

Again the slower air speed case, in figure 61, shows larger water droplets that shed at a lower frequency. The higher air speed case, in figure 60, shows smaller more uniform droplets. It can be seen that at the lower air speed the channel is on the verge of flooding, as the droplet sizes are approaching the dimensions of the channel. The higher air velocity does result in much better droplet removal; however, this effectiveness comes at the cost of an increased pressure drop. The pressure plots for the two cases can be seen in figures 62 and 63.

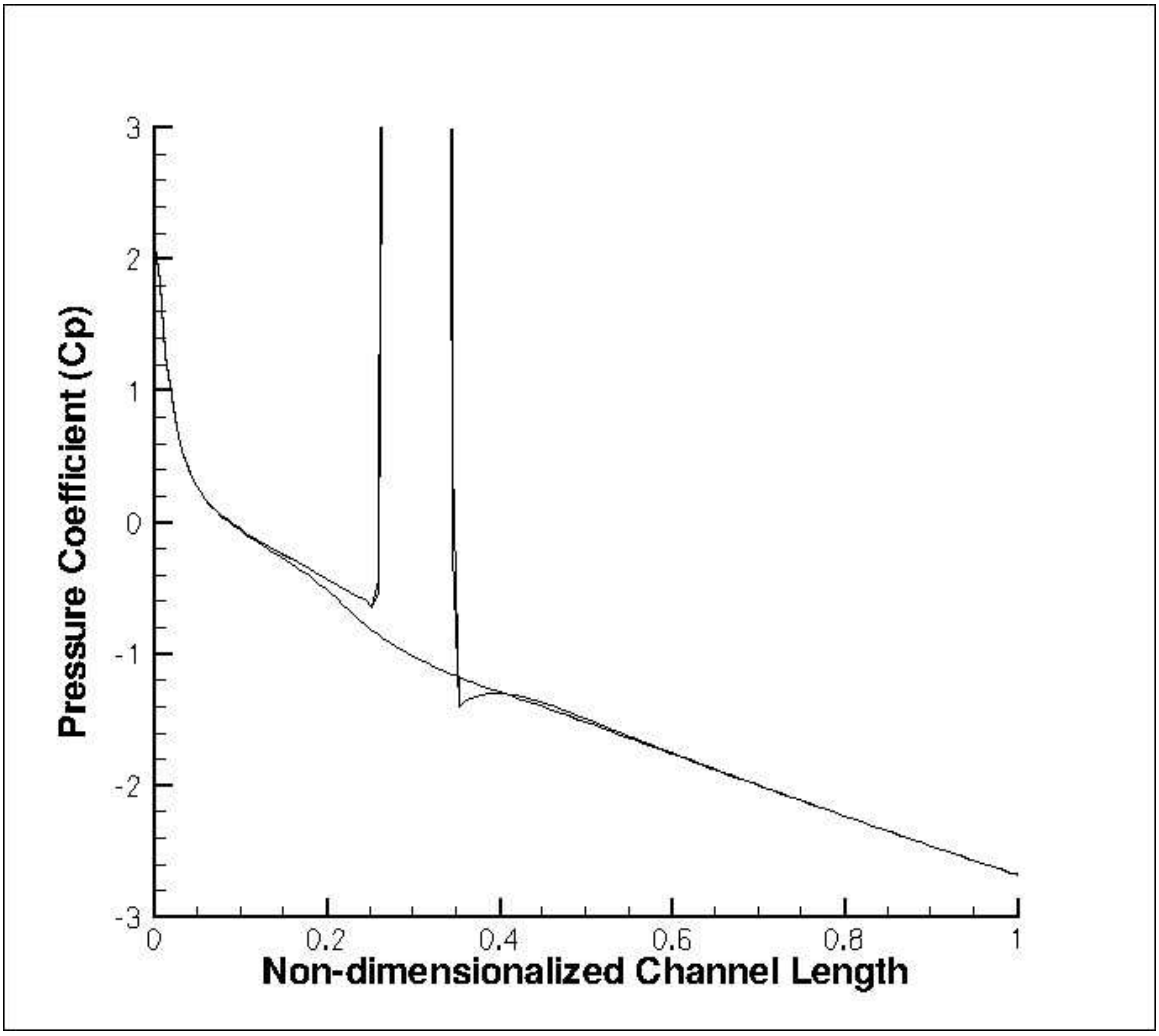

Figure 62: Pressure curve, 2cm/s water injection, 10m/s air speed at a time of 4ms. The two curves represent the max and min values.

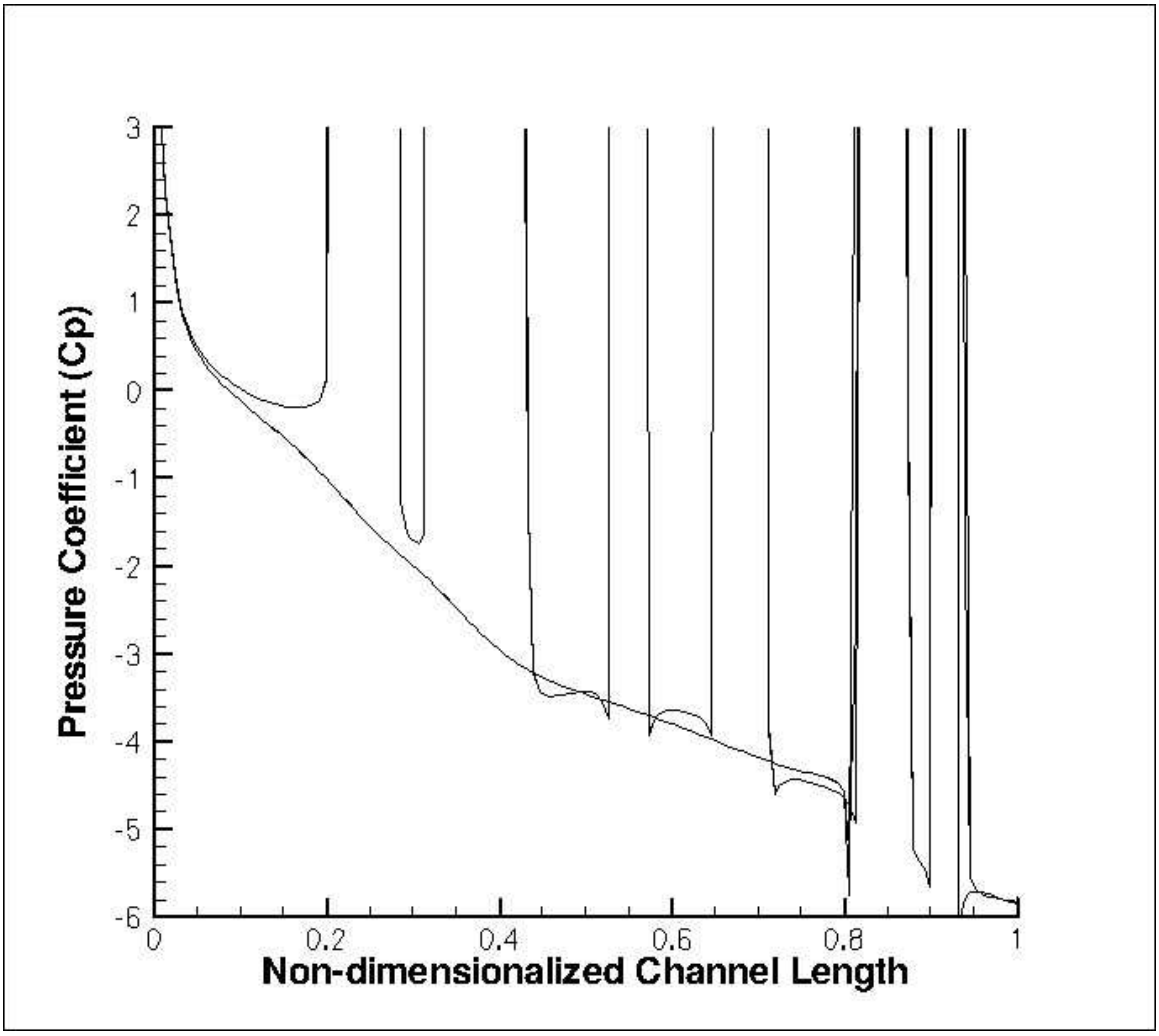

Figure 63: Pressure curve, 2cm/s water injection, 4.4m/s air speed at a time of 4ms. The two curves represent the max and min values.

By comparing the two pressure curves it can be seen that the lower air speed case, in figure 63, produces many more pressure spikes due to the numerous droplets in the flow channel. The high air speed case, in figure 62, shows only one spike because the pressure is only tracked down the channel centerline as discussed previously. The second droplet is offset from the centerline and is therefore not included in the plot. There is one very important item to note from comparing the two cases and that is the estimated pressure drop. Despite the numerous droplets in the flow channel the low air speed case has a

pressure drop of 120Pa. This is drastically less than the pressure drop for the high air speed case where the pressure drop is 285Pa.

As a final evaluation of the effect of the air speed a saturation coverage area comparison was preformed. Figure 64 shows the coverage areas as time progresses.

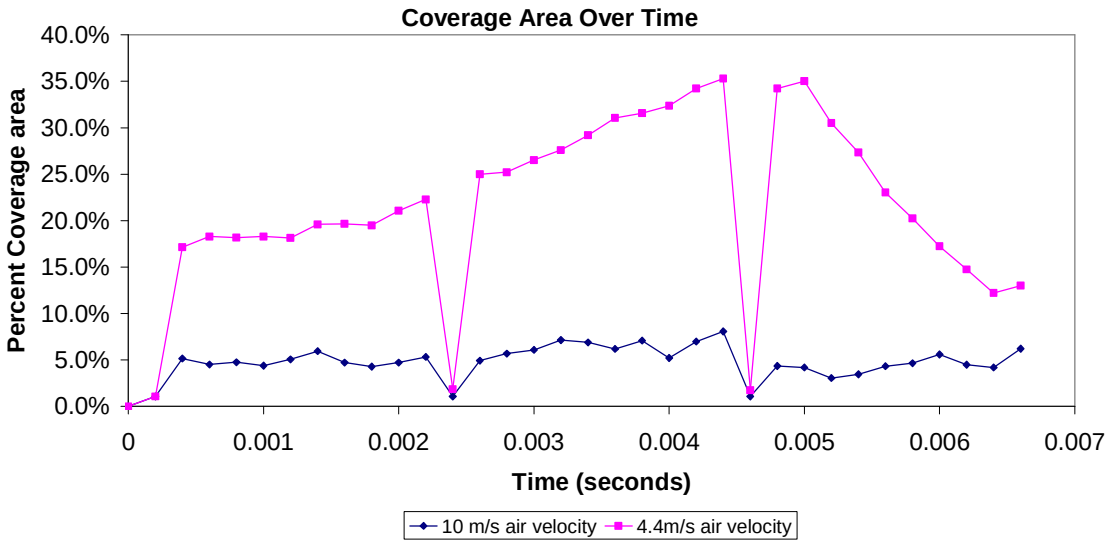

Figure 64: Percent gas diffusion layer coverage area over time for 10m/s and 4.4m/s air velocities, for 2cm/s water injection velocity and 110 degree contact angle.

The figure shows a clear advantage to having a higher air velocity. The coverage area of the gas diffusion layer for the high speed air is less than a third of the coverage area for the slower air velocity.

The trade-off of increasing the air speed is clearly presented in these two cases. The higher air velocity results in smaller more uniform droplets that are shed at a higher frequency. This advantageous shedding characteristic comes at the cost of a drastically larger pressure drop through the channel. The lower air speed case had larger droplets that remained in the channel for longer; however, the pressure drop including these droplet was still less than half that of the fast air speed case. Analysis would have to be

performed on the effects of gas diffusion layer water coverage as compared to reactant flow transport in order to determine the best operating scenario.

4.4 Effect of Water Injection Rate

The next parameter to be evaluated is the effect of the water injection rate on the system. In an operating fuel cell the water entering the channel through the gas diffusion layer would vary as a function of current density. The cases used to observe the effect of the water injection rate have a static contact angle θ_s=110˚, and an air speed U=10m/sec. The higher air speed was chosen because the lower air speed was on the verge of flooding and so the results of the water injection rate alone would not be as easily discernable. Figure 65 shows the phase boundary for the water injection rate V=0.04m/sec at two milliseconds time step.

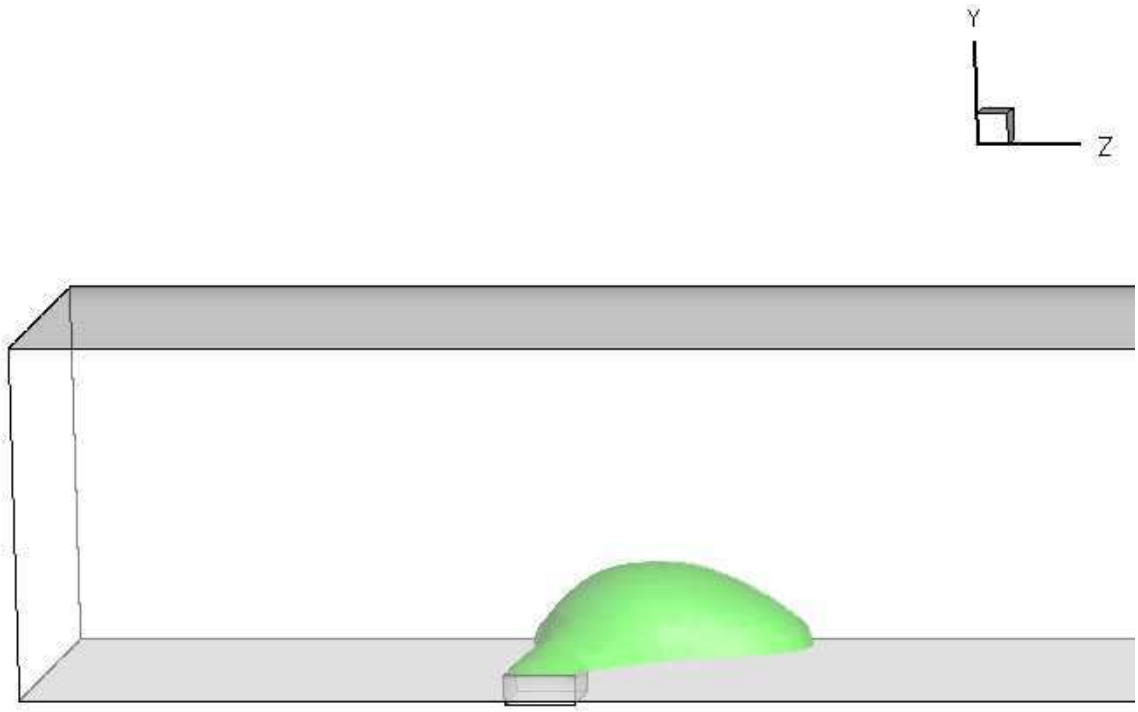

Figure 65: Phase boundary, 4cm/s water injection, 10m/s air speed at a time of 2ms, water droplet emerging from a pore

The phase boundary for the slower injection rate of two centimeters per second is shown in figure 66.

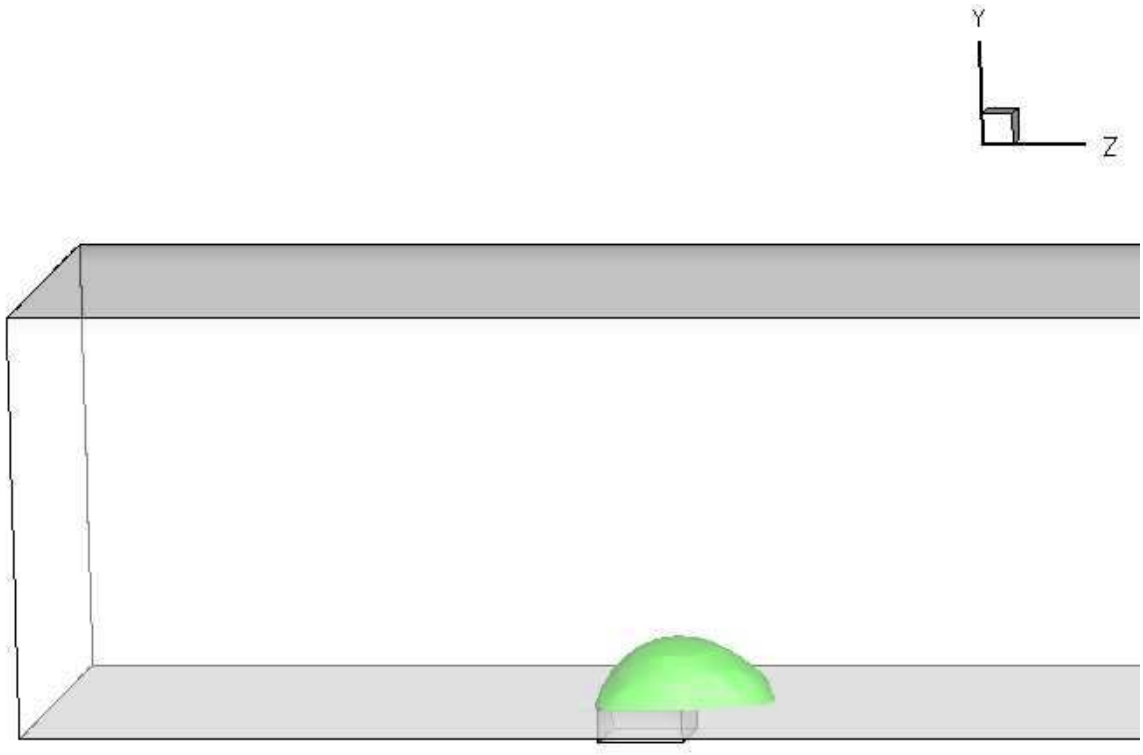

Figure 66: Phase boundary, 2cm/s water injection, 10m/s air speed at a time of 2ms, water droplet emerging from a pore

The differences between the two droplet shapes are easily observed due to the halving of the water injection rate. To examine the droplet shape at a similar volume as the fast injection rate the slow injection rate is observed at 3.2 milliseconds in figure 67. At four milliseconds the water droplet has already been shed in the slower water injection case.

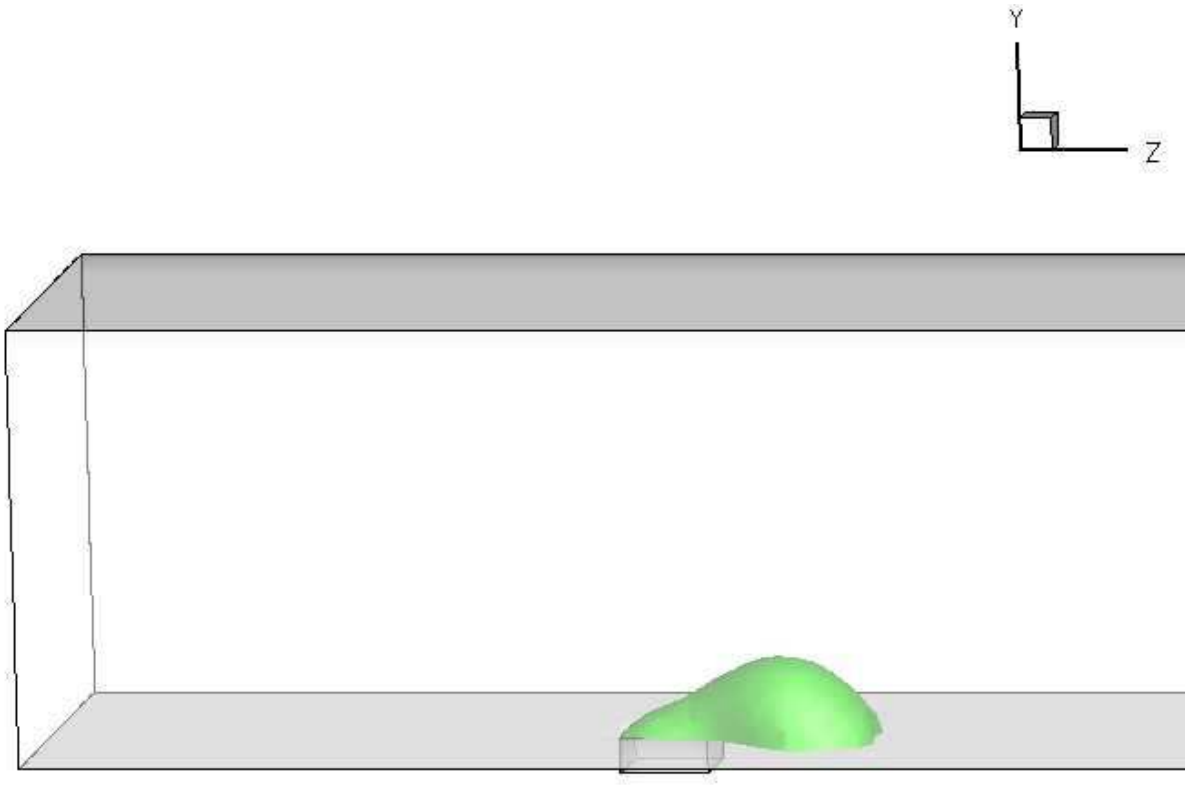

Figure 67: Phase boundary, 2cm/s water injection, 10m/s air speed at a time of 3.2ms, water droplet emerging from a pore

By comparing figures 65 and 67 it can be seen that the droplet shape remains similar, with the droplet leading edge moving downstream leaving a tail attached to the pore. The droplet detachment frequency of the slow water injection velocity (approximately 280Hz) is nearly half that of the higher injection velocity case (approximately 500Hz). Both cases show a slight instability in the droplet position across the channel, with a tendency for the flow to become asymmetric. This is caused by the nature of the dynamic contact angle definition. As the contact line velocity increases the dynamic contact angle increases. The increased contact angle results in a lower resistance to droplet motion and thus the contact line velocity increases. The pressure on the side of the droplet damps these oscillations out as the droplet moves to one side of the channel. This effect is

definitely more prevalent in higher water injection rates due to the higher contact line velocities involved. It should be noted that the tendency to asymmetric flow patterns is also observed experimentally, and is caused by physical perturbations due to the geometry, surface, or inlet flow conditions. The droplet profile for the two cases at a later time step can be seen in figures 68 and 69.

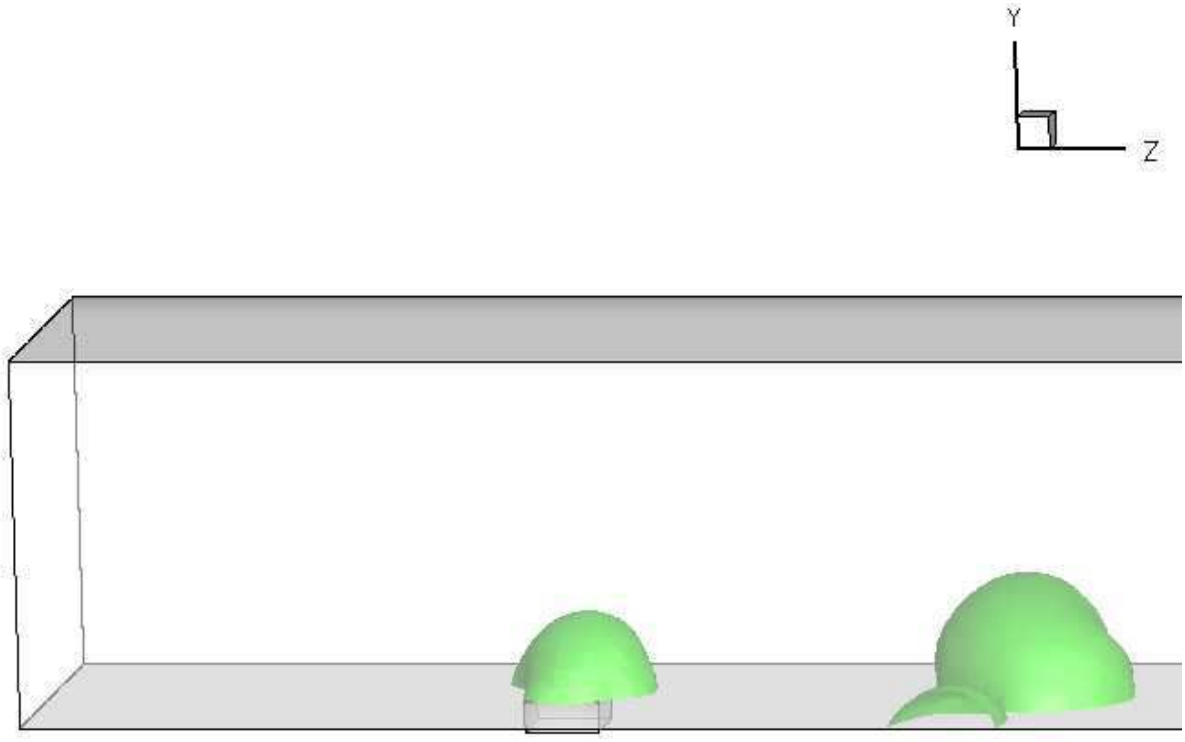

Figure 68: Phase boundary, 4cm/s water injection, 10m/s air speed at a time of 3ms, water droplet emerging from a pore

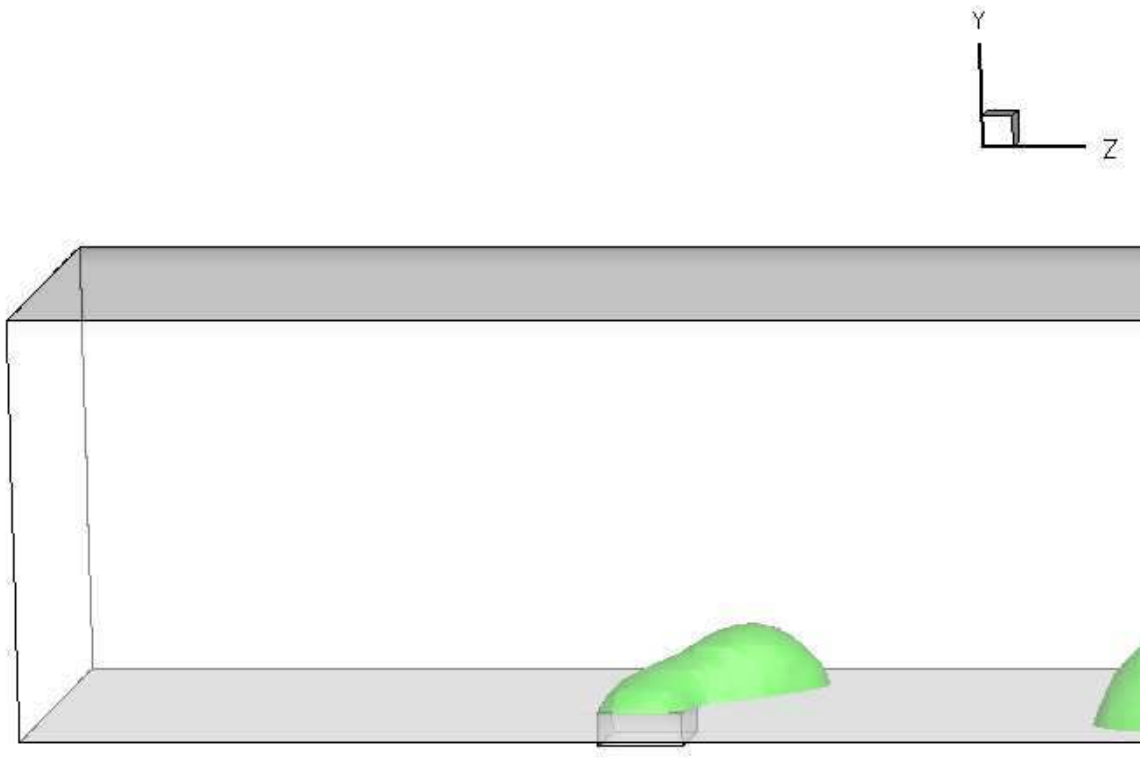

Figure 69: Phase boundary, 2cm/s water injection, 10m/s air speed at a time of 5ms, water droplet emerging from a pore

The higher injection velocity case, in figure 68, shows that the droplets are irregularly shaped and relatively large as they detach. The lower water injection velocity provides smaller more uniform droplets. The two time steps show that the droplet profiles and the shedding characteristics are relatively similar. The pressure curves for the two cases can be seen in figures 70 and 71.

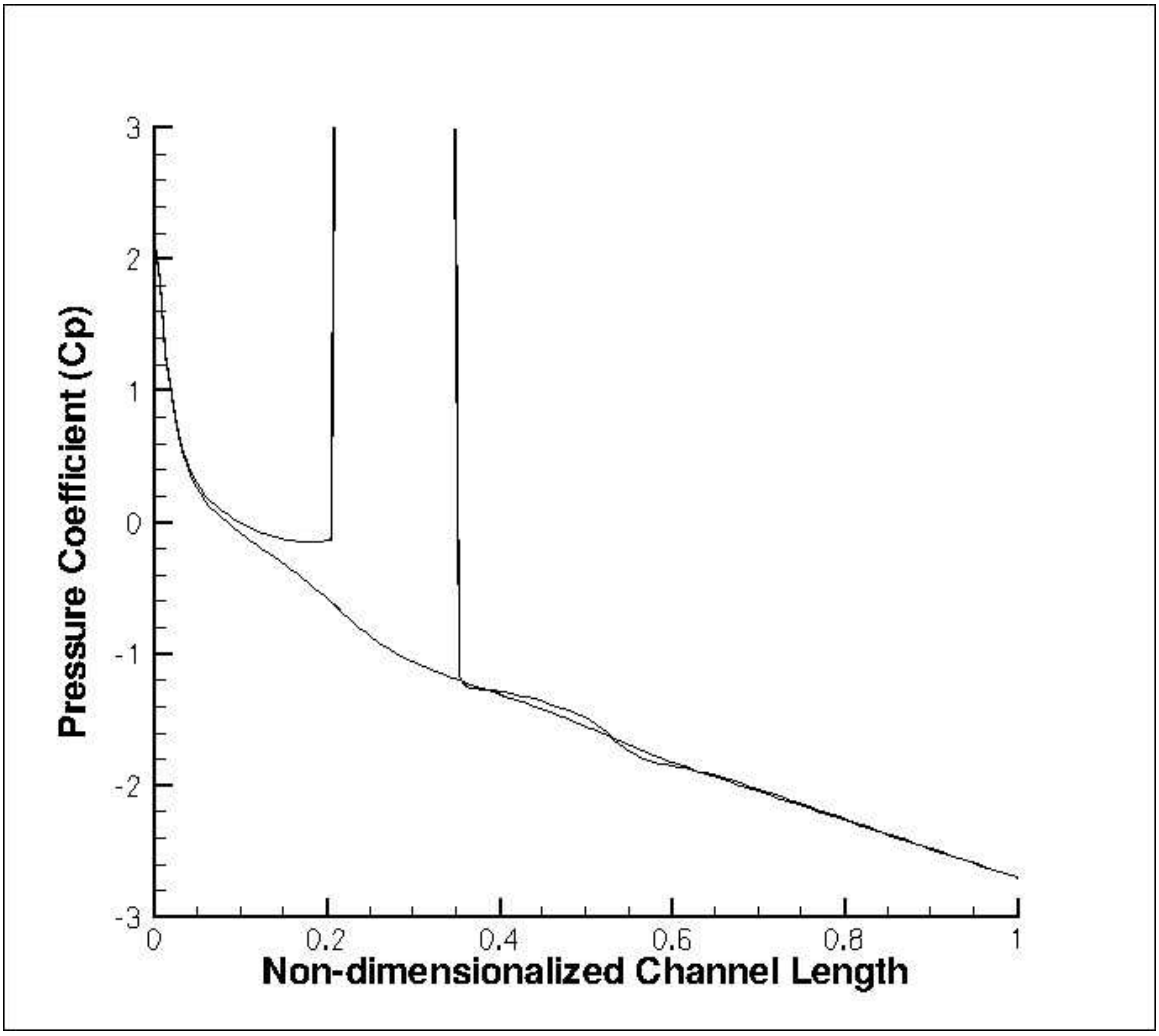

Figure 70: Pressure curve, 4cm/s water injection, 10m/s air speed at a time of 2ms. The two curves represent the max and min values.

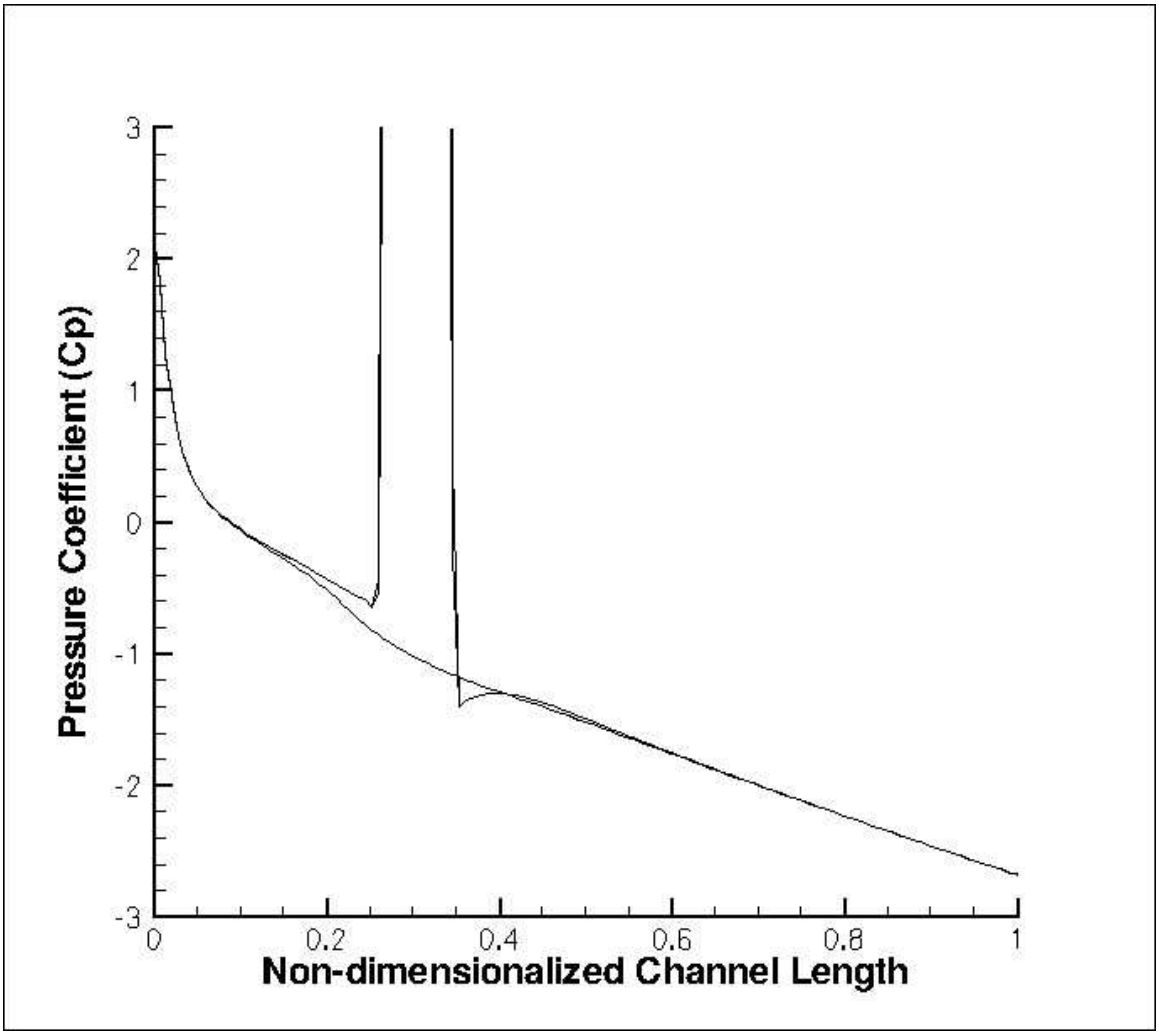

Figure 71: Pressure curve, 2cm/s water injection, 10m/s air speed at a time of 4ms. The two curves represent the max and min values.

The pressure drop through the channel is the same for the two cases, as the droplet shapes and the air velocities at similar droplet stages of evolution are evaluated. This makes intuitive sense because the parameters effecting pressure drop are the air velocity, the profile of any obstacles and overall saturation in the flow channel.

The final evaluation of the effect of the water injection rate, based on the coverage area of the gas diffusion layer, can be seen in figure 72.

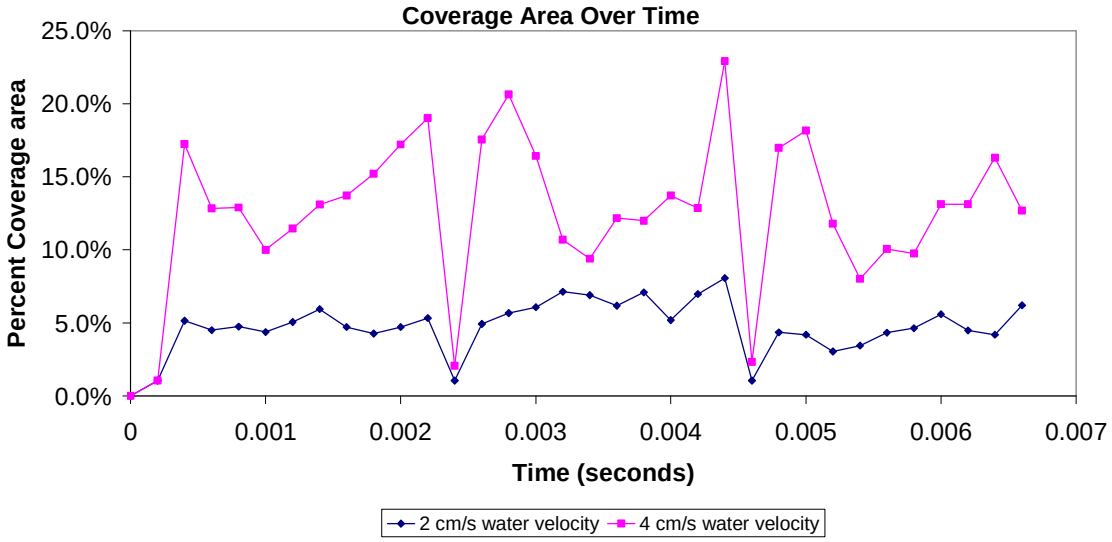

Figure 72: Percent gas diffusion layer coverage area over time for 2cm/s and 4cm/s water injection velocities, for 10m/s air velocity and 110 degree contact angle.

The figure shows that a lower water injection velocity does provide less coverage of the gas diffusion layer. The effect is not as prevalent as the effect of the air velocity as seen in the previous section; however, it does show an improvement.

The evaluation of the two cases leads to the conclusion that the effect of the water injection rate on the droplet dynamics is relatively minor in comparison to the other model parameters. This conclusion agrees with the observations of Theodorakakos et al. [9]. The only noticeable effect is on the water droplet shedding frequency.

4.5 Effect of the Static Contact Angle

The final parameter to be explored is the effect of modifying the static contact angle. We recall that the static contact angle is the basis for determining the dynamic contact angle, as the Hoffman function modifies the static contact angle to the dynamic contact angle through the contact line velocity.

The two cases chosen for comparison have an air flow velocity of U= 4.4 m/sec and a water injection velocity of V=0.02 m/sec. The first case to be explored has a static contact angle of θ_s=110˚, and the phase boundary is shown in figure 73.

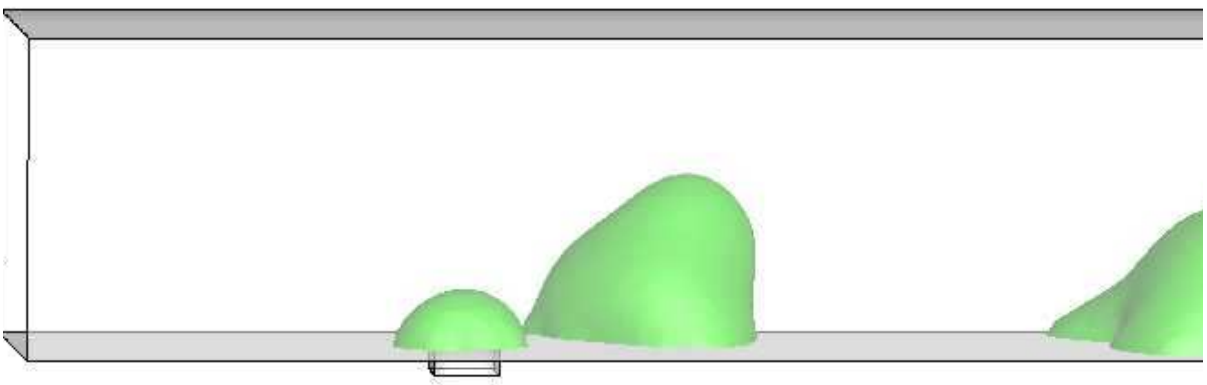

Figure 73: Phase boundary, 110-degree cont. angle, 2cm/s water injection, 4.4m/s air speed at a time of 6ms, water droplet emerging from a pore

It can be seen from figure 73 that the 110-degree contact angle results in a nearly flooded flow channel. The droplets grow to about half the channel size then detach from the pore. The droplets then slowly work their way out of the flow channel. Figure 74 shows the 130-degree contact angle case at the same time step.

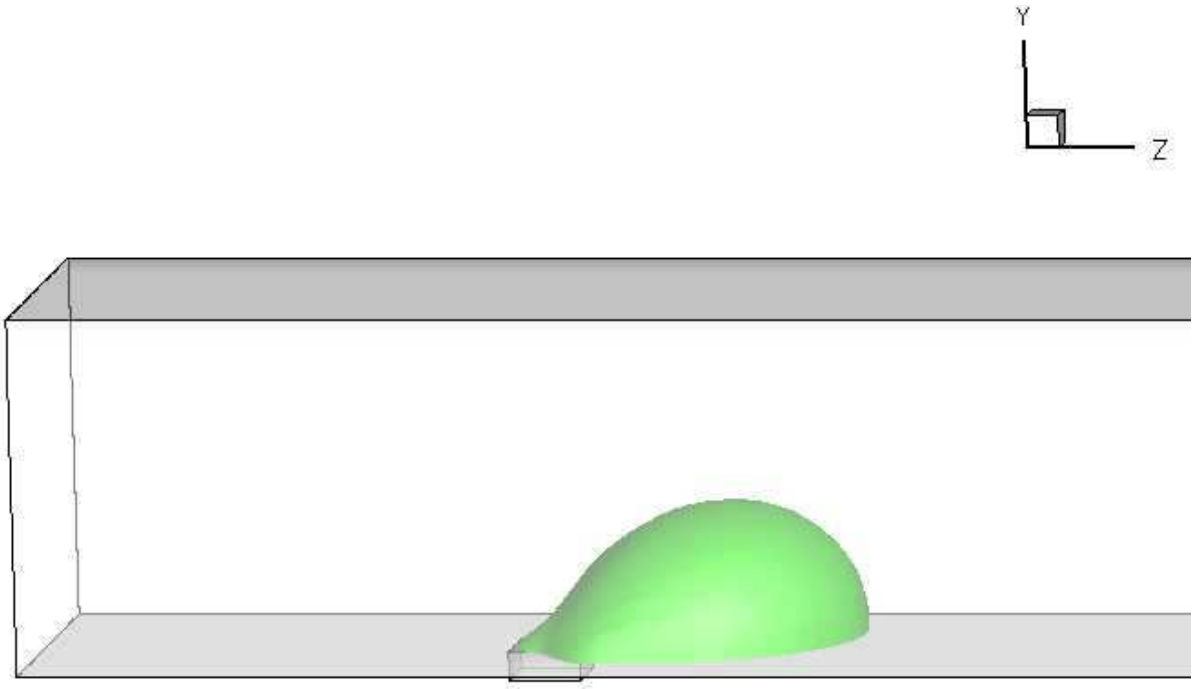

Figure 74: Phase boundary, 130-degree cont. angle, 2cm/s water injection, 4.4m/s air speed at a time of 6ms, water droplet emerging from a pore

The more hydrophobic 130-degree contact angle model shows a much cleaner droplet profile with one oblong droplet forming at the pore. As time evolves the droplet detaches from the pore and moves downstream. The advantage of having a higher contact angle is clear from the model. This result is consistent with experimental work suggesting that higher hydrophobicity results in better droplet shedding. The pressure drop in the higher contact angle model will be lower due to the decreased droplet coverage and decreased pinning force. The plots of the pressure profiles can be seen in figure 75 and 76.

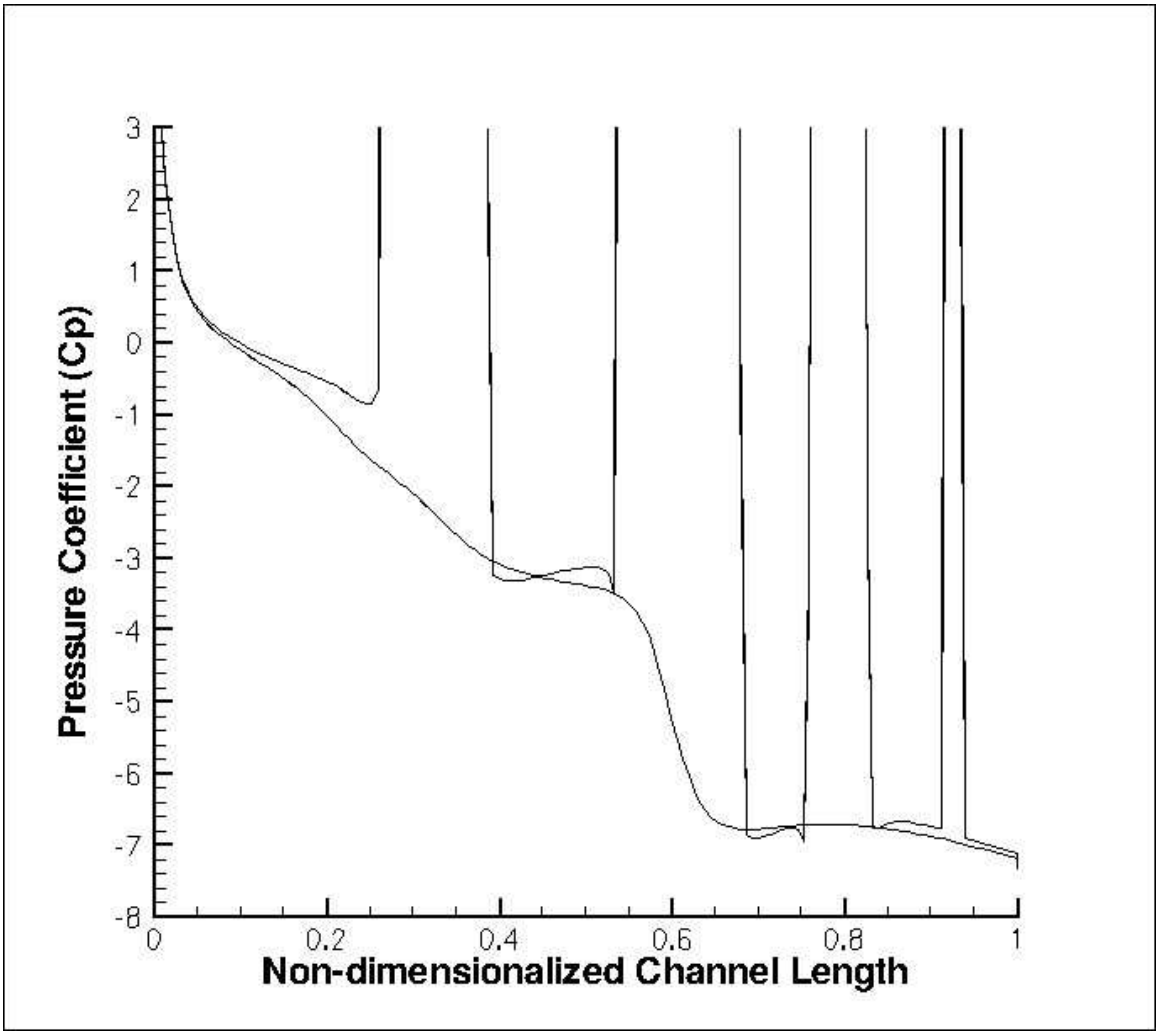

Figure 75: Pressure curve, 110-degree cont. angle, 2cm/s water injection, 4.4m/s air speed at a time of 6ms. The two curves represent the max and min values.

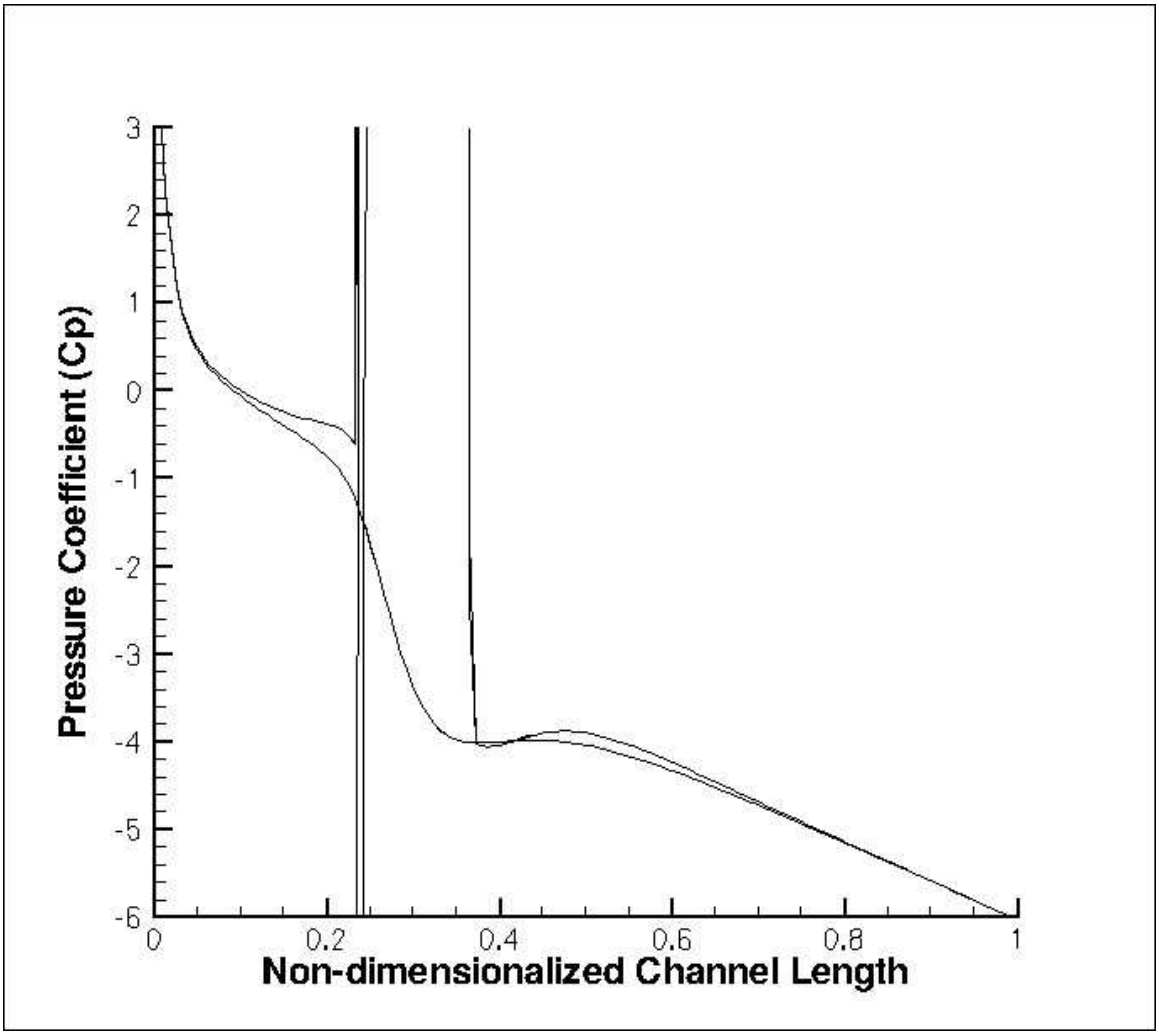

Figure 76: Pressure curve, 130-degree cont. angle, 2cm/s water injection, 4.4m/s air speed at a time of 6ms. The two curves represent the max and min values.

The pressure drop in the 110-degree contact angle model is 136Pa compared to 120Pa for the 130-degree contact angle model. This correlates well with the expected results. The flooding characteristics of the lower contact angle model results in a greater pressure drop in the channel.

The final evaluation will be based on the water coverage area of the gas diffusion layer. Figure 77 shows the effect of the static contact angle on the percent coverage of the gas diffusion layer.

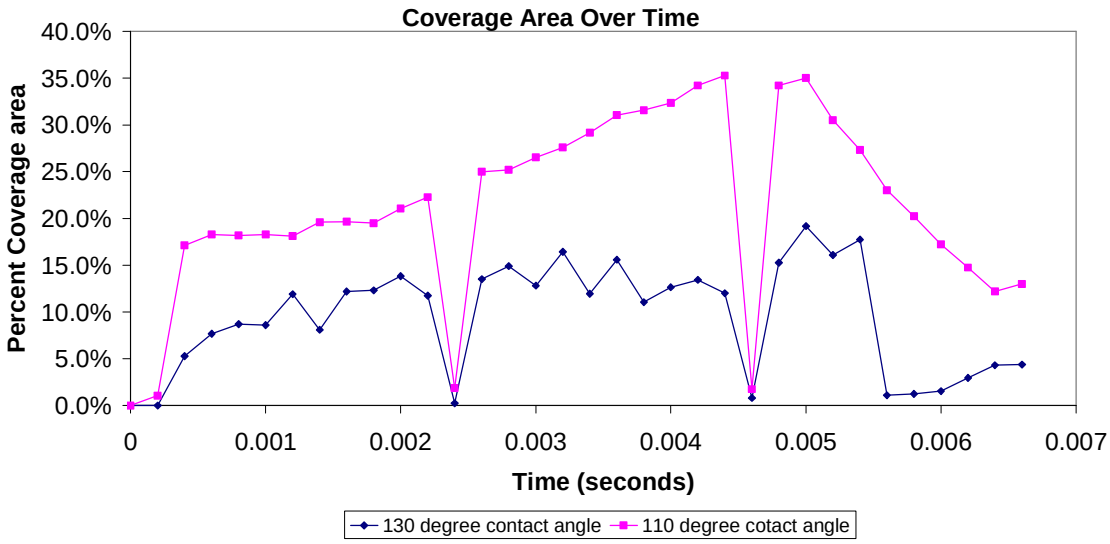

Figure 77: Percent gas diffusion layer coverage area over time for 110 and 130 degree contact angles, for 10m/s air velocity and 2cm/s water injection velocity.

The advantages of having a higher contact angle are clearly visible in the two cases observed. Analysis would have to be performed on the performance loss due to added hydrophobic material in the gas diffusion layer. The decrease in porosity does affect the cell performance, so the balance of performance loss due to decreased reactant transport and the performance gain due to decreased channel flooding would have to be found.

4.6 Flow Circulation within the Droplet

In the experimental work performed by Grant Minor et al. [7] a re-circulating flow field was observed in a droplet subjected to airflow. This effect was also observed in the dynamic contact angle numerical simulations. One such visualization can be seen in figure 75, where the red region represents air and the blue region represents water. The vectors are scaled according to their velocity and are shown as the black arrows.

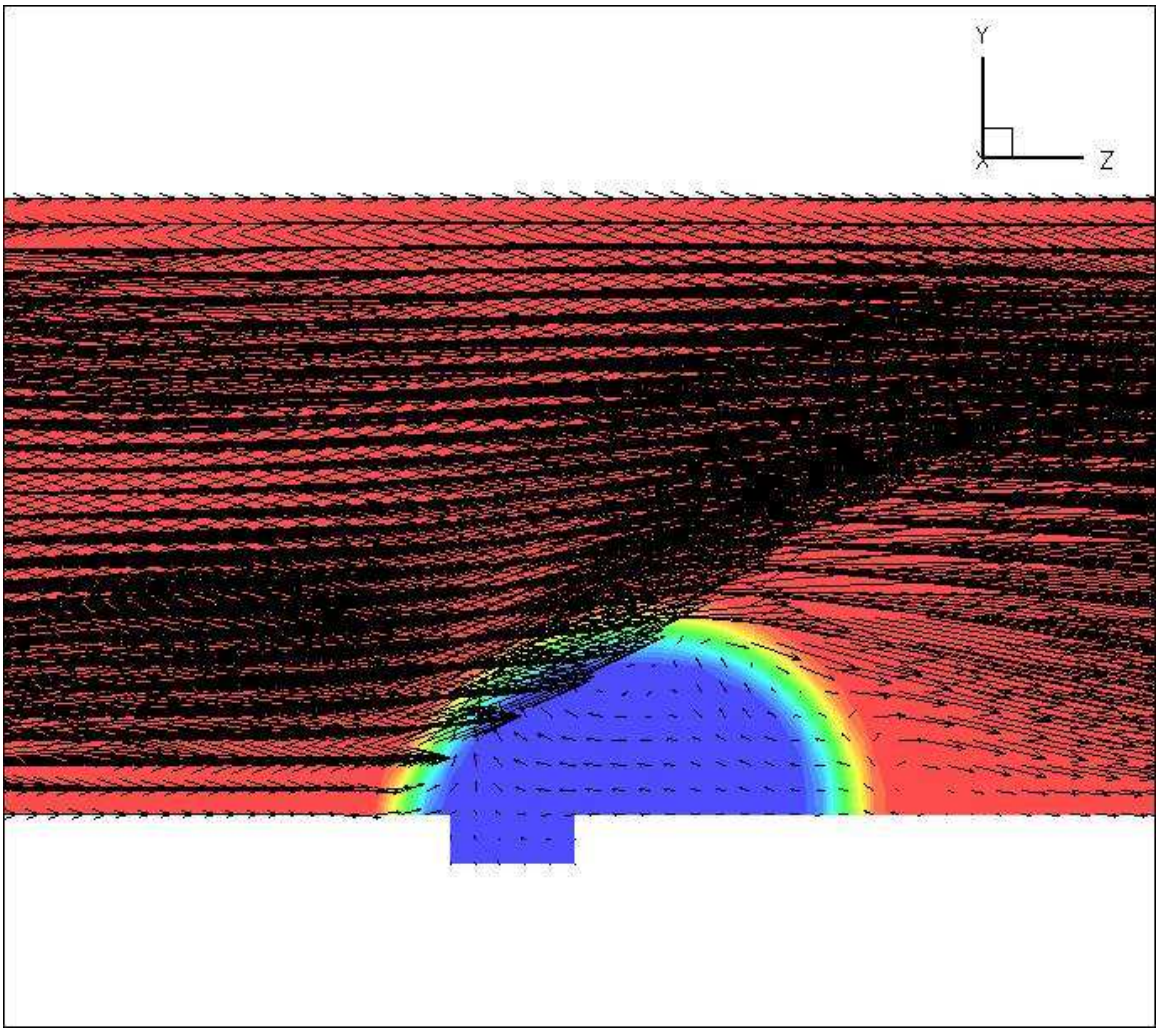

Figure 78: Droplet flow vectors side view, 130 deg. cont. angle, 4.4m/s air vel., 2cm/s water vel. at 6ms

The vectors in figure 75 are scaled according to their flow velocity, making the directions of the vectors in the plot more difficult to see. To see the trend more clearly a vector map is shown in figure 76 with a uniform vector length, indicating only the flow direction.

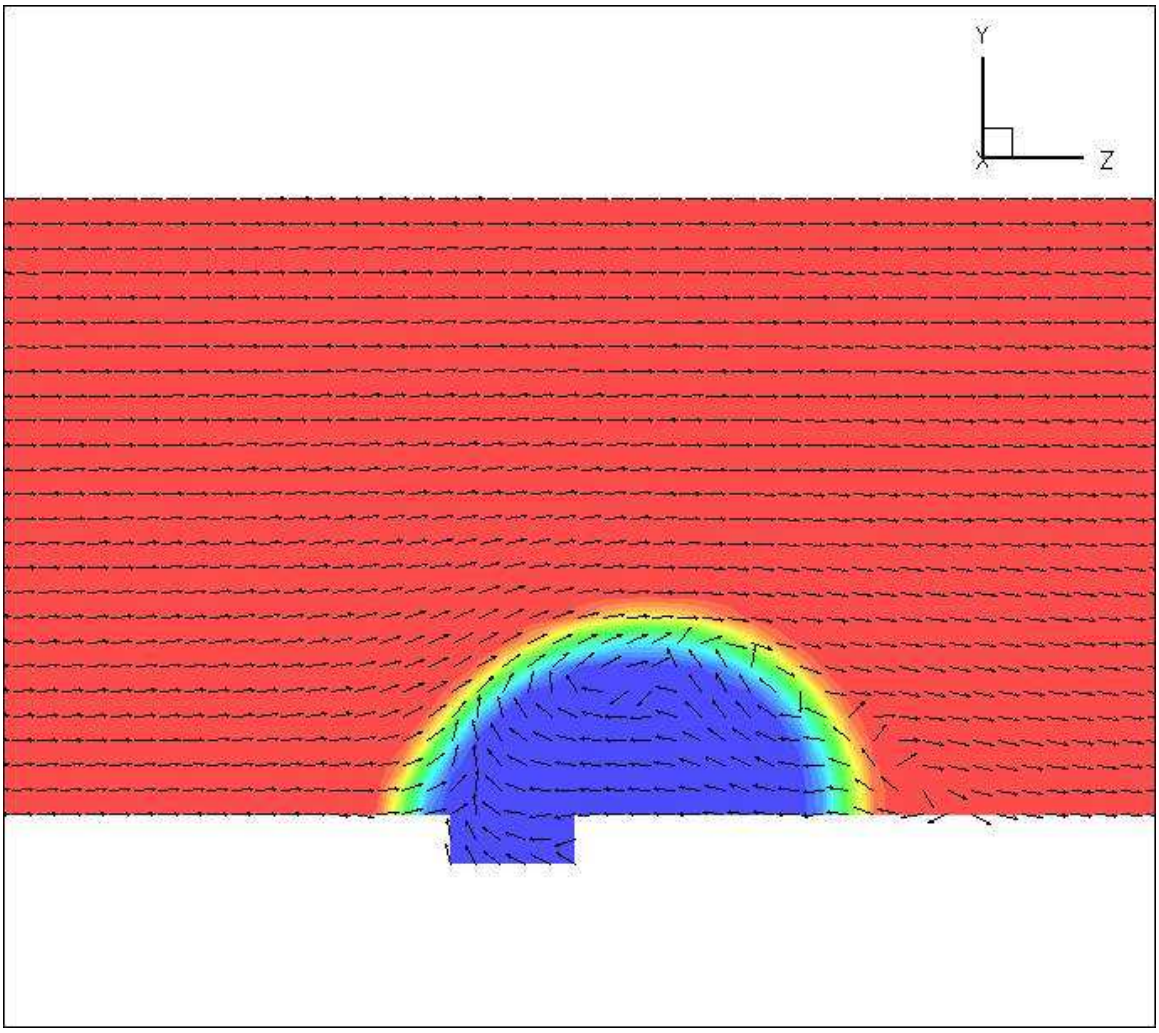

Figure 79: Droplet uniform vectors side view, 130 deg. cont. angle, 4.4m/s air vel., 2cm/s water vel. at 6ms

The re-circulating pattern can clearly be seen. From figure 75 it is shown that though the relative velocity of the water within the droplet is low in comparison to the air speed, it is not negligible. The front view of the same droplet can be seen in figure 77.

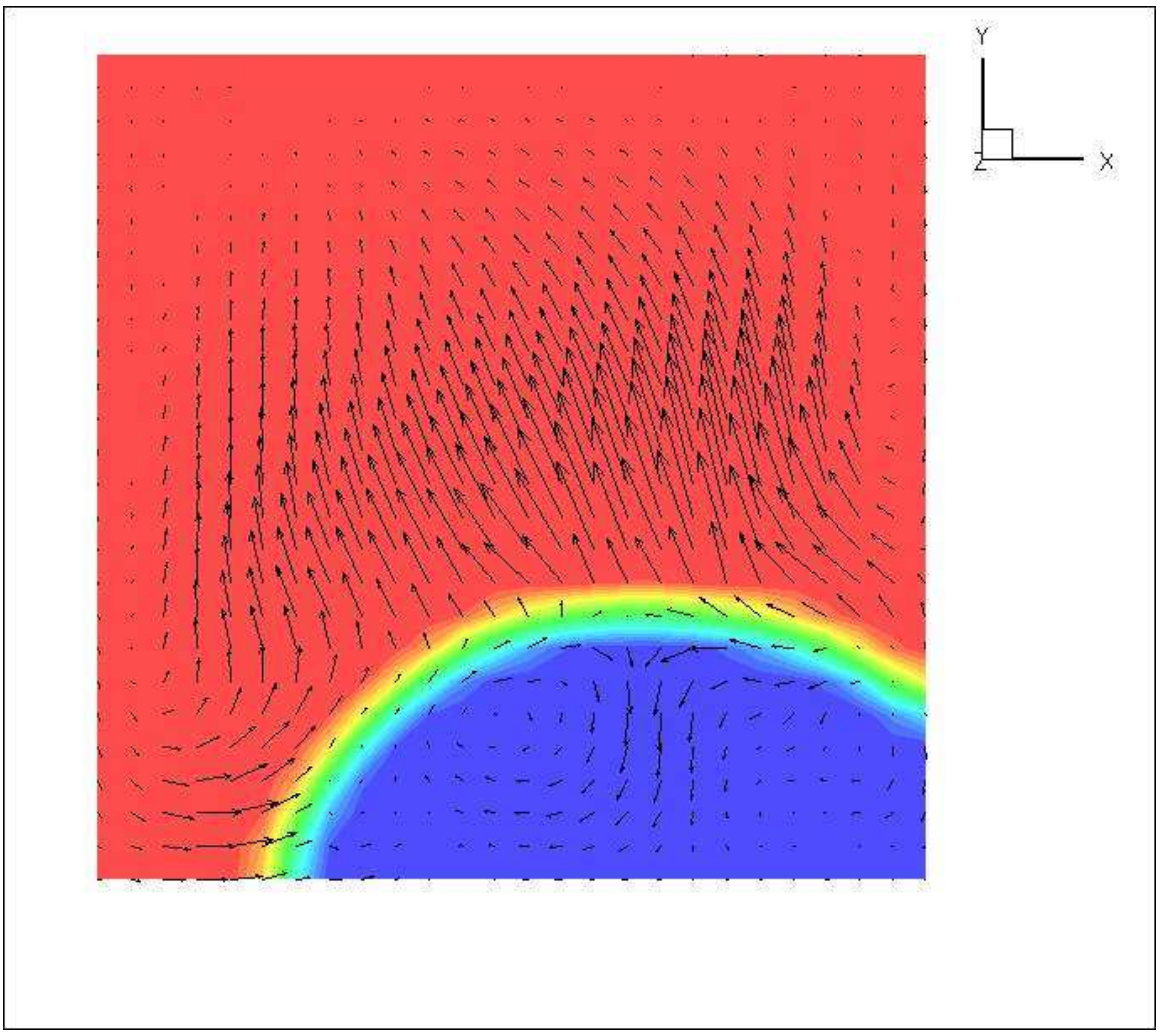

Figure 80: Droplet flow vectors front view (across channel), 130 deg. cont. angle, 4.4m/s air vel., 2cm/s water vel. at 6ms

The twin re-circulating patterns can clearly be seen in figure 77; however, for further clarity on the flow pattern figure 78 shows the same position with uniform vector length.

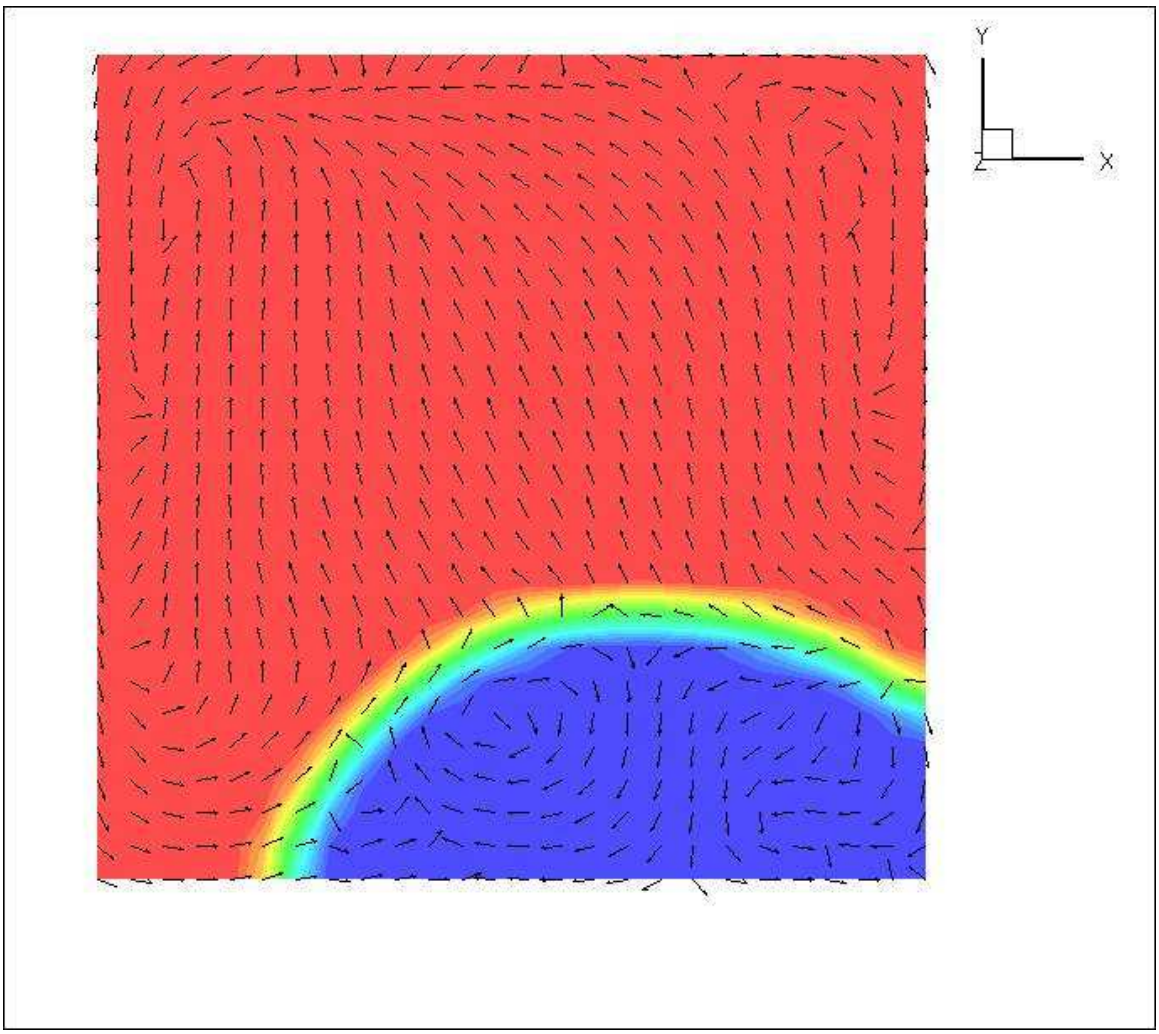

Figure 81: Droplet uniform vectors front view (across channel), 130 deg. cont. angle, 4.4m/s air vel., 2cm/s water vel. at 6ms

The pattern is not perfectly symmetrical about the droplet centerline because the droplet is slightly attached to the one wall. However, the circulation within the droplet does create two distinct circulation cells as the previous works found experimentally [7]. The reproduction of this feature by the dynamic contact angle model points again to the satisfactory physical realism of the model.

5 Summary and Conclusions

An improved representation of the contact line dynamics for two-phase flows was achieved by implementing the dynamic contact angle model of Hoffman [13] into the volume of fluid module of the Fluent commercial CFD code.

The dynamic contact angle model was validated against the experimentally documented case of a droplet impinging on a horizontal surface. The model was also used to examine three base cases of water droplets emerging into a gas flow channel, corresponding to various operating conditions of a polymer electrolyte membrane fuel cell. The fastest flow condition with the maximum air and water injection rates of ten meters per second and four centimeters per second respectively was evaluated to see the model performance in extreme circumstances. The model was also tested in a flooding condition of 4.4 meters per second air velocity and two centimeters per second water injection velocity. In each of the cases, the droplet profiles and the pressure curves show a more realistic representation of the droplet dynamics. The droplets evolve and detach from the pore maintaining an elongated profile. The droplets never become suspended, a common drawback of the static contact angle models. The pressure curves show the expected pressure spike at the droplet location, where the static contact angle model had only a slight perturbation. The validation cases show the advantages of the dynamic contact angle model.

Parametric studies looked at the effects of air speed, water injection velocity and static contact angle. It was determined that the air velocity and the static contact angle have a profound effect on the droplet dynamics. Faster air speed results in smaller more uniform droplet shedding, with no indications of flooding. The higher static contact angle case

results in better water removal as the droplets remains in an oblong shape and do not coat the surface as much as the lower contact angle cases. The variation in water injection velocity yielded little to no difference in the droplet shape and shedding characteristics; however, it did result ina significantly lower gas diffusion layer coverage. The main difference between the water injection velocity cases was the droplet shedding frequency and the coverage area.

The velocity field inside the droplet was observed and compared to the experimental work by Grant Minor [7]. In agreement with experimental observations, it was found that two distinct circulation cells are present in water droplet as the air flows over the droplet surface. The side view shows one large loop swirling clockwise as the airflow promotes the flow. The end view of the droplet shows two cells with the center flow moving towards the bottom of the channel and the outer edge flows circulating towards the top of the droplet.

The dynamic contact angle formulation provides physically representative simulation of liquid water dynamics. The implementation of the code is relatively simple and stable. By adding the dynamic contact angle model to commercial software packages, two-phase fuel cell channel flow dynamics can be simulated more accurately. This added modeling complexity comes with the added cost of increased computational power; however, as the increase in the number of computations required is minimal when the volume fraction is minimal the total change in required computational power for most simulations would be minimal.

Future work on model improvement should be focused on the implementation of the effect of surface roughness on the static contact angle. By determining the spatial map of

the surface roughness for a gas diffusion layer the modification of the model can be effectively implemented. The surface roughness model would allow for closer approximation to the random nature of the gas diffusion layer, without the added complexity of modeling each fibre of the diffusion layer.

6 References

[1] N. Djilali, P.C. Sui, *Transport phenomena in fuel cells: from microscale to macroscale*. International Journal of Computational Fluid Dynamics 22:1(2008) p. 115-131.

[2] E.C. Kumbur, K.V. Sharp, and M.M. Mench, *Liquid droplet behavior and instability in a polymer electrolyte fuel cell flow channel*, Journal of Power Sources 161 (2006) p.333-345.

[3] S. Litster, D. Sinton, and N. Djilali, Ex situ visualization of liquid water transport in PEM fuel cell gas diffusion layers, Journal of Power Sources 154 (2006) p. 95-105

[4] Y. D. Shikhmurzaev, The *moving contact line on a smooth solid surface*, International Journal of Multiphase Flow Volume 19 number 4(1993) p 589-610.

[5] X. Zhu, P.C. Sui, N. Djilali, *Dynamic behavior of liquid water emerging from a GDL pore into a PEMFC gas flow channel*, , Journal of Power Sources 172 (2007) p 287-295.

[6] X. Zhu, P.C. Sui, N. Djilali, *Three dimensional numerical simulations of water droplet dynamics in a PEMFC gas channel*, Journal of Power Sources 181 (2008) p101-115.

[7] G. Minor, N. Djilali, D. Sinton, and P. Oshkai, *Flow within a water droplet subjected to an air stream in a hydrophobic microchannel*, Fluid dynamics Research 41(2009) p.045506.

[8] K. Jiao, B. Zhou, *Innovative gas diffusion layers and their water removal characteristics in PEM fuel cell cathode*, Journal of Power Sources 169 (2007) p296-314.

[9] A. Theodorakakos, T. Ous, M. Gavaises, J.M. Nouri, N. Nikolopoulos, H. Yanagihara, *Dynamics of water droplets detached from porous surfaces of relevance to PEM fuel cells*, Journal of Colloid and Interface Science 300 (2006) p 673-687.

[10] K. S. Chen, M. A. Hickner and D. R. Noble, *Simplified models for predicting the onset of liquid water droplet instability at the gas diffusion layer/gas flow channel interface* , International Journal of Energy Research 29 (2005) p.1113-1132.

[11] C. Fang, C. Hidrovo, F. Wang, J. Eaton, K. Goodson, *3-D numerical simulation of contact angle hysteresis for microscale two phase flow*, International Journal of Multiphase Flow 28 (2008) p 690-705.

[12] K. S. Chen, *Modeling water droplet detachment from GDL/channel interface in PEM fuel cells*, Proceedings of FUELCELL2008-65137

[13] S. Sikalo, H. D. Wilhelm, I.V. Roisman, S. Jakirlic, and C. Tropea, *Dynamic contact angle of spreading droplets: Experiments and simulations*, Physics of Fluids 17-062103 (2005) p. 1-13.

[14] T.D. Blake and Y.D. Shikhmurzaev, *Dynamic Wetting by Liquids of Different Viscosity*, Journal of Colloid and Interface Science 253 (2002) p. 196-202.

[15] http://venus.imp.mx/hilario/SuperComputo/Fluent.Inc…
/manuals/fluent5/ug/html/node540.htm , visited June 3, 2009

[16] Frank M. White, *Fluid Mechanics, 5thedition*, McGraw-Hill, New York, 2003, Table 5.2 p314 and Table A5.

[17] S. Sikalo and E.N. Ganic, *Phenomena of droplet-surface interactions*, Experimental Thermal and Fluid Science 31 (2006) p. 97-110.

[18] S. Berejnor, T.C. Wu and N. Djilali, *Liquid Water Transport in PEM Fuel Cells*, Report submitted to CFD Research Corp., (2009), 22 pages

7 APPENDIX A – Fluent User Defined Program for Dynamic Contact Angle

```
#include "udf.h"
#include "sg_mphase.h"
#include "sg_vof.h"
#include "sg.h"
#include "mem.h"

#define VISCOSITY 0.001
#define SURF_TENS 0.0728
#define MYTRUE 1
#define MYFALSE 0
#define Hoff(x) acos(1-(2.0*tanh(5.16*(pow((x/(1+(1.31*pow(x, 0.99)))), 0.706)))))
#define static_Con_Ang 95.
#define index_source 3


/* This Code computes the normals of the VOF function*/

DEFINE_ADJUST(store_gradient, domain)
{
    Thread *t;
    Thread **pt;
    cell_t c;
    int phase_domain_index = 1;  /* Secondary Domain */
    Domain *pDomain = DOMAIN_SUB_DOMAIN(domain,phase_domain_index);
    void calc_source();

    Alloc_Storage_Vars(pDomain,SV_VOF_RG,SV_VOF_G,SV_NULL);
    Scalar_Reconstruction(pDomain, SV_VOF,-1,SV_VOF_RG,NULL);
    Scalar_Derivatives(pDomain,SV_VOF,-1,SV_VOF_G,SV_VOF_RG,
                Vof_Deriv_Accumulate);


    mp_thread_loop_c (t,domain,pt)
      if (FLUID_THREAD_P(t))
       {
         Thread *ppt = pt[phase_domain_index];

         begin_c_loop (c,t)
         {
           calc_source(c,t);
         }
         end_c_loop (c,t)
       }
    Free_Storage_Vars(pDomain,SV_VOF_RG,SV_VOF_G,SV_NULL);


}
```

```
void calc_source(cell_t cell, Thread *thread)
  {

          real VOF_Val[3], VOF_Mag, source, VOF_Norm[3];
          Thread *phaset;
          phaset= THREAD_SUB_THREAD(thread,1);

          if(C_VOF(cell,phaset)!=0.0 && N_TIME > 1)
           {
                  /* The gradients of the VOF function are found in the x,y and z dir.       */
          if (NULLP(THREAD_STORAGE(phaset, SV_VOF_G)))
               {
                 Message0("N_TIME = %d, ....show-grad:Gradient of VOF is not available \n ", N_TIME);
                    Error("0");
               }
                    VOF_Val[0]=-C_VOF_G(cell,phaset)[0];
                    VOF_Val[1]=-C_VOF_G(cell,phaset)[1];
                    VOF_Val[2]=-C_VOF_G(cell,phaset)[2];

                    /* The magnitude of the VOF gradients is found so it can be normalized            */
                    VOF_Mag=NV_MAG(VOF_Val);
                    if(VOF_Mag!=0.0)
                      {
                              VOF_Mag=NV_MAG(VOF_Val);
                              VOF_Norm[0]=VOF_Val[0]/VOF_Mag;
                              VOF_Norm[1]=VOF_Val[1]/VOF_Mag;
                              VOF_Norm[2]=VOF_Val[2]/VOF_Mag;

                      }
                    else
                      {
                              /* This is to avoid the divide by zero function*/
                              VOF_Norm[0]=0.0;
                              VOF_Norm[1]=0.0;
                              VOF_Norm[2]=0.0;
                      }

                    C_UDMI(cell,thread,0)=VOF_Norm[0];
                    C_UDMI(cell,thread,1)=VOF_Norm[1];
                    C_UDMI(cell,thread,2)=VOF_Norm[2];
            }
          source = 0.0;
          C_UDMI(cell, thread, index_source) = source;
  }

DEFINE_SOURCE(VOF_Norms, cell, thread, dS, eqn)
{
  real source;
  source = C_UDMI(cell, thread, index_source);
  return source;
}
```

```
/* This Define_profile code is designed to provide a dynamic contact angle for the VOF function*/
DEFINE_PROFILE(con_ang, t, pos)
{
        /* First the various pointer variables are created*/
        face_t f;
        cell_t c;
        real feta_d, vel_Val[3], cont_Line_Vel, VOF_Normal[3], cap_Num, static_Con_Rad, x_Bottom,
x_Top, x_Bisect, hoff_Old, hoff_Cur, hoff_New, finish_Cond, inv_Hoff=0.0;
        int notConverged, itNum;
        Thread *t0,*pt;

/* This code is designed to find the zero for the inverted hoffman function by finding the zero    */
/* of the function at which the hoffman function results in the static contact angle               */
        /* First the variables are assigned*/
        notConverged=MYTRUE;
        x_Bottom=0.001;
        x_Top=2.0;
        itNum=0;
        static_Con_Rad=((static_Con_Ang*M_PI)/180.);
        /* A while loop performs the bisection method, a simple but very stable zero finder      */
        while(notConverged)
         {
                /* The variables used in the bisection method are assigned and the hoffman       */
                /* functions are evaluated                                                       */
                itNum++;
                hoff_Old=(Hoff(x_Bottom)- static_Con_Rad);
                hoff_Cur=(Hoff(x_Top)- static_Con_Rad);
                x_Bisect=(x_Bottom+x_Top)/2.0;
                hoff_New=(Hoff(x_Bisect)- static_Con_Rad);
                finish_Cond=fabs(1-(x_Bisect/x_Top));

                /* The loop ends when the relative error is less than 1e-8 and the inverse       */
                /* hoffman value is stored for use later                                         */
                if(finish_Cond<0.00000001 || itNum>10000000)
                 {
                        inv_Hoff=x_Bisect;
                        notConverged=MYFALSE;
                 }
                /* Conditions for the bisection method
        */
                if((hoff_Old*hoff_New)<0.0)
                 {
                        x_Top=x_Bisect;
                 }
                if((hoff_Cur*hoff_New)<=0.0)
                 {
                        x_Bottom=x_Bisect;
                 }

         }
/* Now the main loop goes through all the faces in the boundary                                  */
        begin_f_loop(f,t)
      {
```

```
                /* The cell and phase threads are isolated                          */
                c=F_C0(f,t);
                t0=THREAD_T0(t);
        pt= THREAD_SUB_THREAD(t0,1);
                /* The main formulation is only applied if the VOF is >0            */
                if(C_VOF(c,pt)!=0.0)
                 {
                        /* The velocities are recorded in each direction            */
                        vel_Val[0]=C_U(c,t0);
                        vel_Val[1]=C_V(c,t0);
                        vel_Val[2]=C_W(c,t0);

                        /* The VOF normals are brought in
        */
                        VOF_Normal[0]=C_UDMI(c,t0,0);
                        VOF_Normal[1]=C_UDMI(c,t0,1);
                        VOF_Normal[2]=C_UDMI(c,t0,2);


                        /* The contact line vel. is calc from the dot product of VOF and Vel  */
                        cont_Line_Vel=NV_DOT(vel_Val,VOF_Normal);

                        /* The capillary number is found based on cont line vel.    */
                        cap_Num=fabs((VISCOSITY*cont_Line_Vel)/SURF_TENS);

                        /* The dynamic contact angle is defined then stored in the profile  */
                        if(cap_Num+inv_Hoff<0.0)
                          {
                                cap_Num=inv_Hoff;
                          }
                        feta_d=((Hoff(cap_Num+inv_Hoff))*180)/M_PI;
                        F_PROFILE(f,t,pos)=feta_d;
                 }
                else
                 {
                        F_PROFILE(f,t,pos)=static_Con_Ang;
                 }
      }
          end_f_loop(f,t)
}
```

Droplet initialization code for falling droplet:

```
#include "udf.h"

/* This Define_init code makes a droplet at the origin*/
DEFINE_INIT(Drop_Init,mixture_domain)
{
#if !RP_HOST
          /* First the various pointer variables are created*/
          int phase_domain_index;
```

```
        cell_t cell;
        Thread *t;
        Domain *subdomain;
        real position[ND_ND],distance, dropCen[3],dropRad;

        /* The cells are all looped through                                    */
        dropRad=0.00135;
        dropCen[0]=-1.0*dropRad;
        dropCen[1]=0.0;

        sub_domain_loop(subdomain, mixture_domain, phase_domain_index)
          {
                if (DOMAIN_ID(subdomain) == 3)

            thread_loop_c(t,subdomain)
                  {
                        begin_c_loop_all(cell,t)
                          {
                                C_CENTROID(position,cell,t);
                                distance=sqrt((pow(position[0]-dropCen[0],2.0)+pow(position[1]-
dropCen[1],2.0)));

                                if(distance<dropRad)
                                  {
                                        C_VOF(cell,t)=1.0;
                                        C_U(cell,t)=1.566815184;
                                  }
                                else
                                        C_VOF(cell,t)=0.0;
                          }
                        end_c_loop_all(cell,t)
                  }
          }
#endif
}
```

8 APPENDIX B – User Defined Function Flow Chart

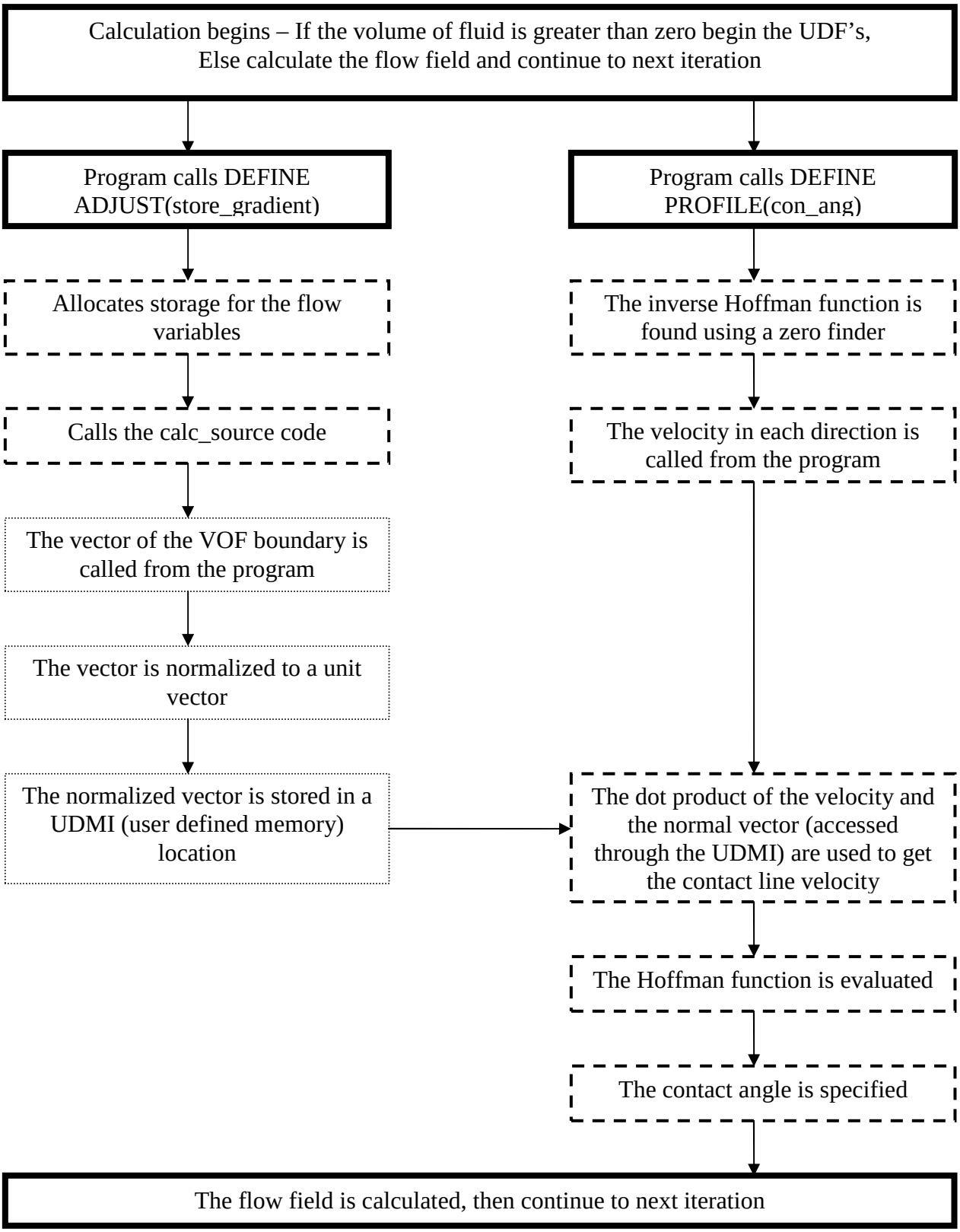

9 APPENDIX C – Improved Droplet Balance Model

1. INTRODUCTION

The water management in a polymer electrolyte fuel cell is a critical issue in ensuring high cell performance. The water production, due to electro-osmotic drag, in the cathode side of the fuel cell leads to liquid water formation in the gas diffusion layer and the reactant flow channel. If this water is allowed to accumulate in the fuel cell the flow of reactants to the membrane assembly will be inhibited and cell performance will suffer. This build up of excess water is referred to as flooding. The opposing design constraint comes from the performance of the membrane assembly. The membrane assembly is designed to operate within an optimal water saturation region. If the membrane has less than the optimal water saturation the conductivity decreases causing a loss in performance. To balance these competing requirements a system must be designed to remove just the excess liquid water, leaving enough water to hydrate the membrane assembly. The design space can be seen in figure 1, where a droplet is emerging from a pore into the gas flow channel.

The tight design requirement of balancing the water at the gas diffusion layer displays a need for accurate water droplet stability models as a fuel cell design tool. The droplet stability model described in the current work is an analytically based model, proposed as a modification to the model presented by Kumbar and Mench [1].

2. MATHEMATICAL FORMULATION

2. 1 Assumptions

The new model will assume the fluids are a continuum. To validate this assumption the Knudsen number was checked. The criterion for assuming continuum is:

$$Kn < 1 \cdot 10^{2} \tag{5}$$

It can be seen that the Knudsen number for a duct is given as:

$$Kn = \frac{L}{D_h}$$

$$Kn = \frac{\left(\frac{\mu\sqrt{\pi}}{\rho\sqrt{2RT}} \right)}{\left(\frac{A_c}{\Gamma} \right)} \tag{6}$$

With air at 300k and a rectangular section:

$$\frac{A_c}{\Gamma} = \frac{hw}{2(h+w)}$$

$$\mu = 1.99 \cdot 10^{-5} \frac{kg}{ms}$$

$$\rho = 1.08 \frac{kg}{m^3}$$

$$R = 287 \frac{J}{kgK}$$

$$T = 300K$$

Based on the above values the criterion is:

$$\frac{1 \cdot 10^{-2}}{1.574 \cdot 10^{-7}} \geq \left(\frac{1}{w} + \frac{1}{h} \right)$$

$$\left(\frac{1}{w} + \frac{1}{h} \right) \leq 63.53 \cdot 10^{3} \tag{7}$$

Based on this criterion the model is valid for flow areas as small as 0.05mm x 0.023mm. So the assumption is a valid one for traditional flow channels.

2. 2 Model Description

The proposed new model uses a different philosophy than the Kumbur model. The force balance will be performed for two different cases. A force balance on the droplet alone will be used to estimate the point of instability for the droplet. A force balance will also

be performed on the control volume around the droplet to estimate the pressure drop over that section of channel.

Shear Stress Forces

The first stage in the model development is to estimate the shear on the droplet section. The analytical representation for the average flow velocity in a rectangular duct is given as [2]:

$$\bar{u} = \left(\frac{\Delta P}{L}\right)\frac{h^2\beta}{4\mu} \tag{8}$$

With:

$$\beta = \left[\frac{1}{3} - \frac{64h}{w\pi^5}\tanh\left(\frac{\pi w}{2h}\right)\right] \tag{9}$$

It can be noted the exact solution to the rectangular duct is given by an infinite sum; however, the solution can be truncated to the first term of the infinite series with minimal induced error [2].

Isolating the change in pressure over the length term:

$$\left(\frac{\Delta P}{L}\right) = \frac{4\bar{u}\mu}{h^2\beta} \tag{10}$$

The average shear stress over the surface can be estimated using:

$$\bar{\tau} = \left(\frac{\Delta P}{L}\right)\frac{A_c}{\Gamma} = \frac{4\bar{u}\mu}{h^2\beta}\left(\frac{A_c}{\Gamma}\right) \tag{11}$$

Integrating the shear stress over the outer surface ignoring the droplet gives a shear force of:

$$F_{shear} = \int_A^B \overline{\tau}\ \Gamma dx$$
$$= \int_0^d \frac{4\overline{u}\mu}{h^2\beta}(hw)dx \tag{12}$$
$$F_{shear} = \frac{4\overline{u}\mu wd}{h\beta}$$

This average shear stress value is integrated over the surface of the channel walls to get the shear stress for that small section of channel to be used in the system control volume force balance.

Next the drag over the droplet will be estimated. The cross-sectional area and perimeter over the droplet cross section, as seen in figure 2, is:

$$A_c = \pi x(d-x) \tag{13}$$

$$\Gamma = 2\pi\sqrt{x(d-x)} \tag{14}$$

Assuming that the density is constant and the transition is smooth the shear stress on the drop is:

$$\overline{\tau}_{Droplet} = \frac{4\overline{u}\mu}{h^2\beta}\left(\frac{\pi x(d-x)}{2\pi\sqrt{x(d-x)}}\right) \tag{15}$$

The droplet average shear stress will act tangent to the surface so the x-direction is isolated using trigonometry.

$$\overline{\tau}_{Droplet-x} = \overline{\tau}_{Droplet}\left(\frac{2\sqrt{x(d-x)}}{d}\right) \tag{16}$$

This shear stress is integrated over the spherical surface to get the shear stress acting in the x-direction. This will be used as an estimate for the drag on the droplet.

$$F_{drag} = \int_0^d \overline{\tau}_{Droplet-x} \Gamma dx$$
$$= \int_0^d \left[\frac{4\overline{u}\mu}{h^2\beta} \left(\pi x (d-x) \right) \left(\frac{2\sqrt{x(d-x)}}{d} \right) \right] dx \quad (17)$$
$$F_{drag} = \frac{3d^3\pi^2\overline{u}\mu}{16h^2\beta}$$

Surface Tension

The next force in the force balance is the surface tension force, as seen in figure 3. Noting that the surface tension acts in the direction of the contact angle an expression for the surface tension force is:

$$dF_{ST-x} = -\gamma_{lv} \cos(\pi - \theta_\alpha) \cos(\alpha) ds$$
$$dF_{ST-x} = \frac{-c\gamma_{lv}}{2} \cos(\pi - \theta_\alpha) \cos(\alpha) d\alpha \quad (18)$$

The contact angle is assumed to vary linearly from the advancing to the retreating angle. The average of the advancing and retreating angle is assumed to be the static contact angle for the surface. Therefore, the contact angle at any angle alpha between zero and π is:

$$\theta_\alpha = \theta_A + \alpha \frac{\theta_R - \theta_A}{\pi} \quad (19)$$

The assumption is also made that the droplet is approximately spherical in shape. Using the geometry of the problem the differential form of the surface tension is:

$$dF_{ST-x} = \frac{-c\gamma_{lv}}{2} \cos\left[\pi - \left(\theta_A + \alpha \frac{\theta_R - \theta_A}{\pi} \right) \right] \cos(\alpha) d\alpha \quad (20)$$

Taking advantage of trigonometric identities

$$dF_{ST-x} = \frac{c\gamma_{lv}}{4}\lambda d\alpha$$
$$\lambda = \cos\left[\theta_A + \alpha\left(\frac{\theta_R - \theta_A}{\pi} + 1\right)\right] + \cos\left[\theta_A + \alpha\left(\frac{\theta_R - \theta_A}{\pi} - 1\right)\right] \quad (21)$$

Integrating around half the circle and doubling the result gives the surface tension force projected onto the x axis.

$$F_{ST-x} = \frac{-\gamma_{lv}c}{2}\left(\sin\theta_A + \sin\theta_R\right)\left[\frac{\pi}{\theta_R - \theta_A - \pi} + \frac{\pi}{\theta_R - \theta_A + \pi}\right] \quad (22)$$

Pressure Force

Finally the pressure drop is estimated using a control volume force balance. The drag force on the droplet and the shear force on the walls are counter-acted by the pressure drop across the droplet.

$$A_c\Delta P = \overline{\tau}_{wall}\Gamma L + \frac{C_D\rho\overline{u}^2 A_f}{2} \quad (23)$$

Where L is the length of the droplet section, which in this case is the droplet diameter.

The co-efficient of drag over a droplet is given as [3]:

$$C_D = \frac{24}{\mathrm{Re}_d}\left(1 + 0.1925\,\mathrm{Re}_d^{0.63}\right) \quad (24)$$

Inserting the appropriate values the pressure drop across the droplet section is:

$$\Delta P = \frac{4\overline{u}\mu d}{h^2\beta} + \frac{3\overline{u}\mu\pi d}{hw}\left[1 + 0.1925\left(\frac{\overline{u}\rho d}{\mu}\right)^{0.63}\right] \quad (25)$$

Multiplying the pressure drop by the frontal area of the drop produces the total pressure force in the x-direction of:

$$F_{Px} = \frac{\bar{u}\mu\pi d^3}{h^2\beta} + \frac{3\bar{u}\mu\pi^2 d^3}{4hw}\left[1 + 0.1925\left(\frac{\bar{u}\rho d}{\mu}\right)^{0.63}\right] \tag{26}$$

Placing all of the terms into the droplet force balance yields:

$$F_{Px} + F_{Drag} - F_{ST} = 0$$

$$\left\{\begin{array}{l} \dfrac{\bar{u}\mu\pi d^3}{h^2\beta} + \dfrac{3\bar{u}\mu\pi^2 d^3}{4hw}\left[1 + 0.1925\left(\dfrac{\bar{u}\rho d}{\mu}\right)^{0.63}\right] + \dfrac{3d^3\pi^2\bar{u}\mu}{16h^2\beta} - \\ \dfrac{\gamma_{lv}C}{2}\left(\sin\theta_A + \sin\theta_R\right)\left[\dfrac{\pi}{\theta_R - \theta_A - \pi} + \dfrac{\pi}{\theta_R - \theta_A + \pi}\right] \end{array}\right\} = 0 \tag{27}$$

Because the model has too many variables some empirical relations were derived. The contact angle as a function of PTFE content was estimated using a parabolic curve fit:

$$\begin{array}{l} -0.0766045548\left(PTFE\right)^2 + \\ \qquad 3.02277\left(PTFE\right) + 135 = \theta \end{array} \tag{28}$$

The contact angle hysteresis was estimated in a similar fashion:

$$\left[\begin{array}{l} -0.008\left(PTFE\right)^2 + \\ 0.36\left(PTFE\right) + 2.4 \end{array}\right]\bar{u} = \theta_R - \theta_A \tag{29}$$

The final relation used is for the surface tension:

$$\frac{\left[\begin{array}{l} -0.0000388\left(PTFE\right)^2 + \\ 0.001606\left(PTFE\right) - 0.03222 \end{array}\right]}{\cos\left(\theta\right)} = \gamma_{LV} \tag{30}$$

Each of the above relations was a parabolic curve fit to experimental data presented by Kumbur [1].

The surface tension is based on an average solid-liquid and solid-vapour surface tension value.

$$\frac{[0.020]}{\cos(\theta)} = \gamma_{LV} \tag{31}$$

3. RESULTS

3.1 Model Validation

The experimental data from Kumbur and Mench was used to verify the model. First the droplet height relative to flow velocity was compared at a 5% PTFE Coating. As can be seen in figure 4, the Kumbur model predicts instability after it has occurred. The new proposed model predicts instability just before instability occurs. At higher Reynolds numbers the new proposed model predicts instability more accurately than the Kumbur model. The results for a PTFE coating of 20% can be seen in figure 5. Summaries of the error at various data points are given in tables 1 and 2. It can be seen that the average error over the range of model applicability is reduced from the Kumbur model.

3.2 Parametric Study

These two validation cases were for a fixed channel size. To see the effects of adjusting the channel dimensions a parametric study was performed. The effects of modifying the height and the width of the channel can be seen in figures 6 and 7. It can be observed that the two curves match as would be expected for an identical flow area. As the channel area is decreased the droplet becomes unstable at a smaller diameter, resulting in quicker detachment of the droplet.

The final parametric study was performed based upon the PTFE content of the diffusion media and the results can be seen in figure 8. It can be seen that the effect of PTFE coating plateaus close to zero and 20% PTFE coating. As the PTFE content increases the droplet size for instability decreases as expected. From these results an optimal PTFE coating would be approximately 16% as larger PTFE coatings result in

minimal droplet height improvements but will result in a lower electrical and thermal conductivity.

4. CONCLUSIONS

Through validation against experimental data the proposed model was verified to be an accurate predictor of instability for a liquid droplet emerging from a pore into a gas flow channel. The model better predicts the instability curve when compared against the Kumbur model. Through parametric studies it was determined that increasing the PTFE content to approximately 16% maximizes water droplet removal, where higher contents provide minimal gains in water removal. It was also surmised that a smaller flow channel area results in smaller droplet diameters at the onset of instability. Using these design parameters optimal flow channel designs can be developed.

ACKNOWLEDGEMENTS

The authors wish to acknowledge the insightful input and guidance of Ned Djillali and Majid Bahrami throughout this work.

NOMENCLATURE

A_c	Cross-sectional area, m^2
A_f	Flow area, m^2
c	Chord length of droplet, m
C_D	Drag co-efficient
d	Droplet diameter, m
D_h	Hydraulic diameter, m
F_{drag}	Drag force, N
F_{st}	Surface tension force, N
L	Length, m
GDL	Gas diffusion layer
Kn	Knudsen number
P	Pressure, Pa
Per	Perimeter, m
Re_d	Reynolds number (based on diameter)
R_u	Universal gas constant, 8.314 J/mol-K
T	Temperature, K
t	Time, s
$\vec{u}$	Bulk fluid velocity, m/s
x	X-coordinate (Along the channel)
y	Y-coordinate (perpendicular to GDL)

Greek

θ_A	Advancing angle, radians
θ_R	Receding angle, radians
γ	Surface Tension, N/m
Γ	Perimeter, m
μ	Dynamic viscosity, kg/m-s
ρ	Mass density, kg/m^3
$\bar{\tau}$	Shear Stress tensor, N/m^2

Subscript

wall	The GDL and channel wall surfaces
l	Liquid
s	Solid
v	Vapour

REFERENCES

1. E.C. Kumbur, K.V. Sharp, and M.M. Mench, *Liquid droplet behavior and instability in a polymer electrolyte fuel cell flow channel*, Journal of Power Sources 161 (2006) 333-345.
2. M. Bahrami, M.M. Yovanovich, and J.R. Culham, *Pressure Drop of Fully-Developed, Laminar Flow in Micro channels of Arbitrary Cross-Section*, Journal of Fluids Engineering 128 (2006) 1036-1037
3. R. Clift, J.R. Grace, and M.E. Weber, *Bubbles, Drops, and Particles,* (1978) 56

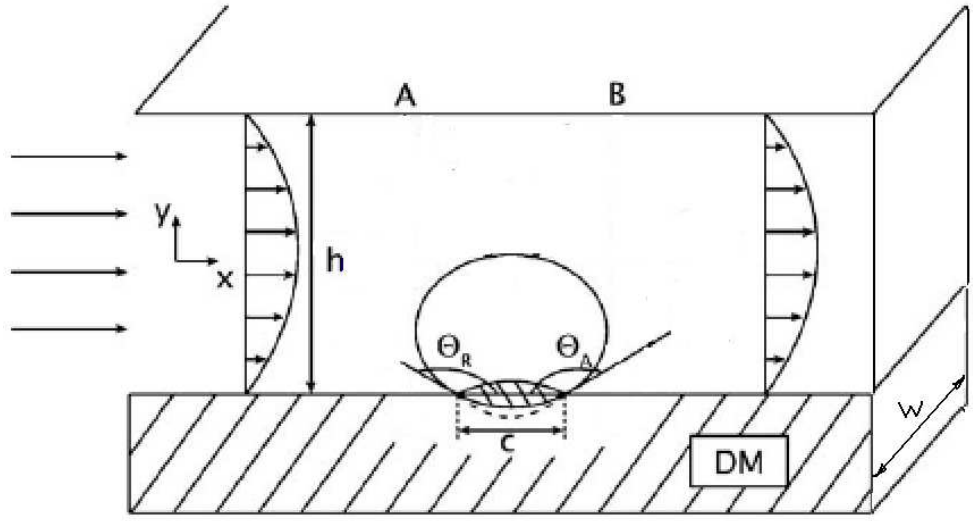

Figure 1: Flow conditions for the droplet – system control volume

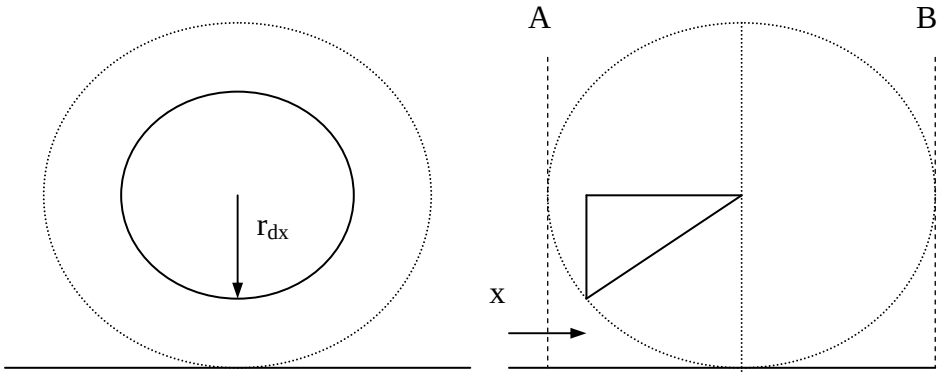

Figure 2: Droplet x-section area and perimeter

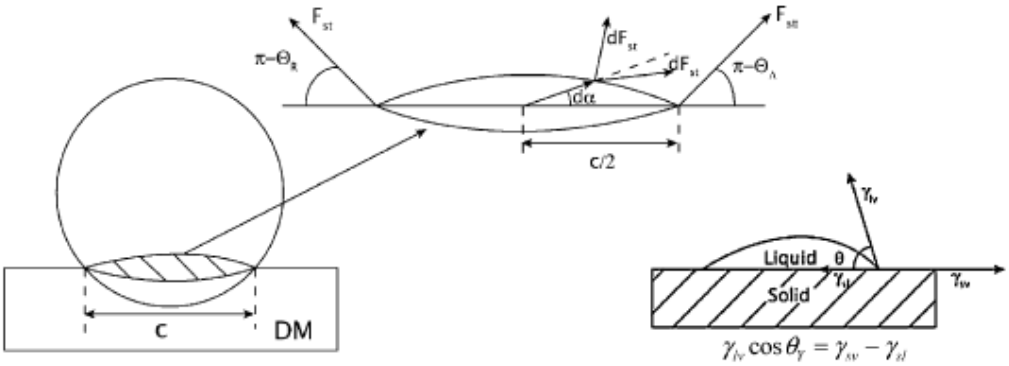

Figure 3: Surface Tension Force [1]

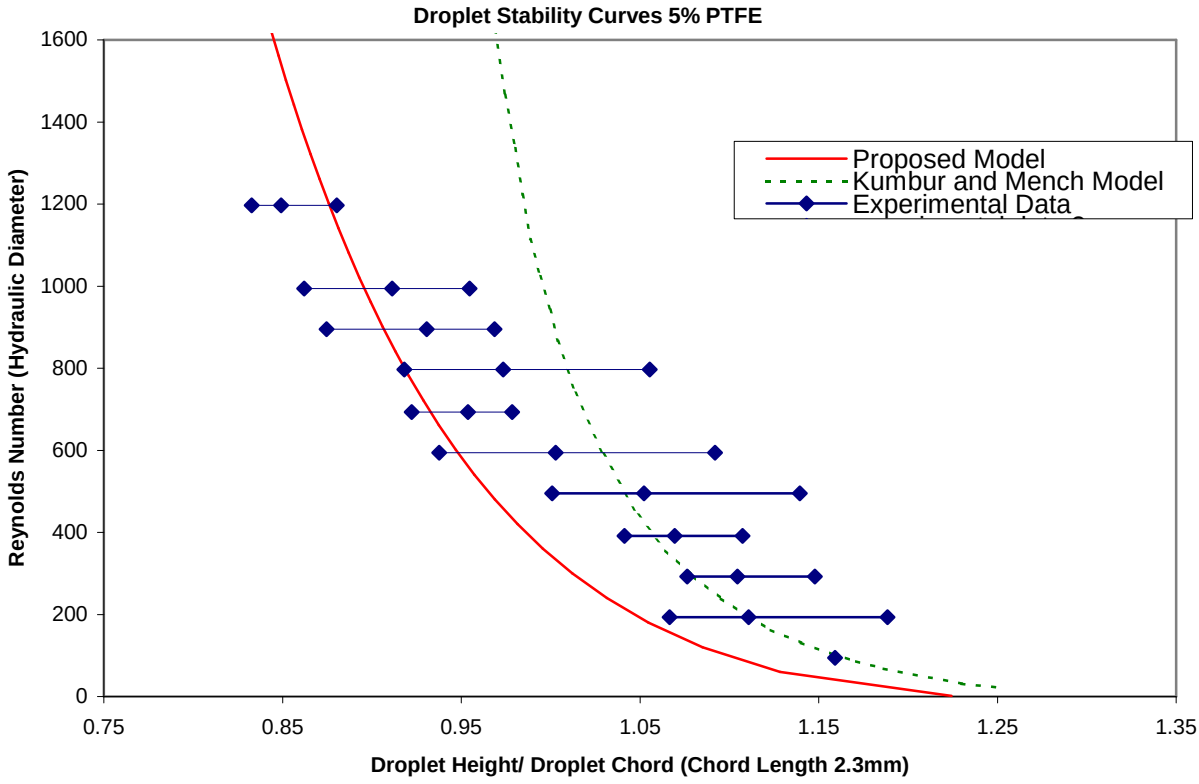

Figure 4: Droplet Stability Curve 5% PTFE

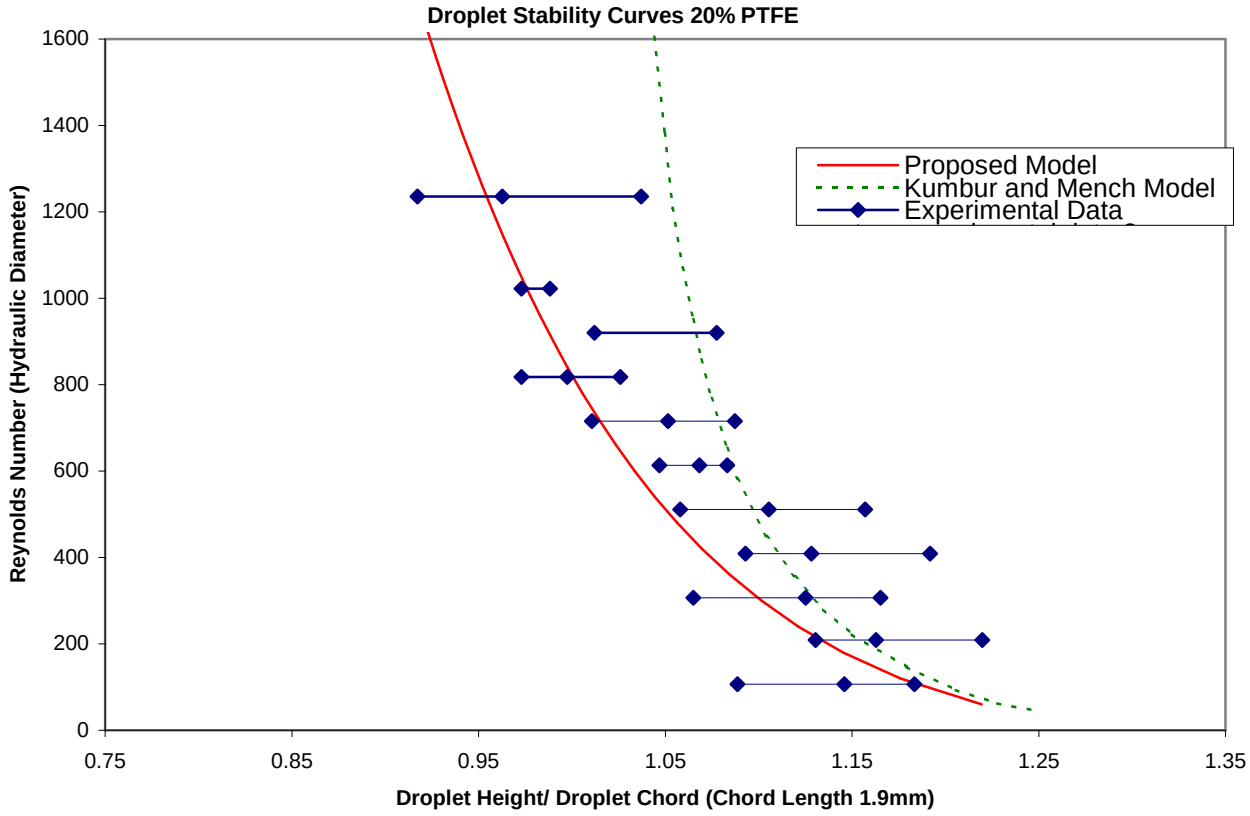

Figure 5: Droplet Stability Curve 20% PTFE

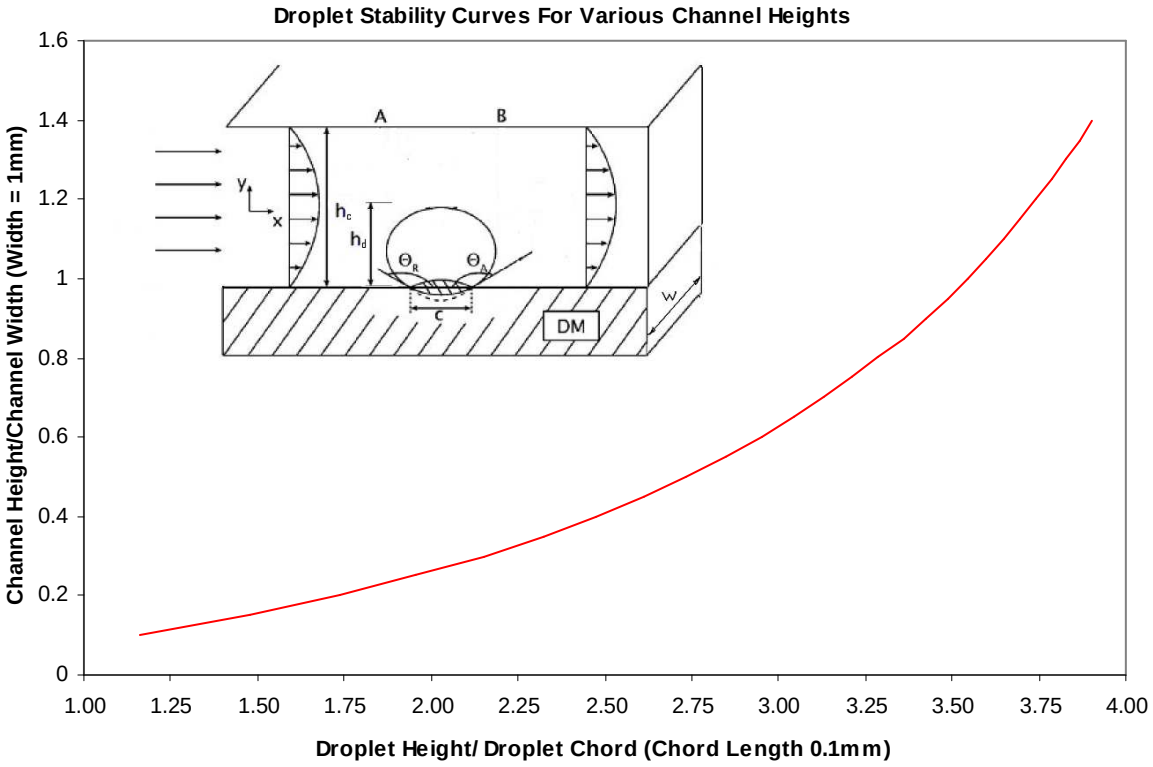

Figure 6: Effects of modifying the channel height

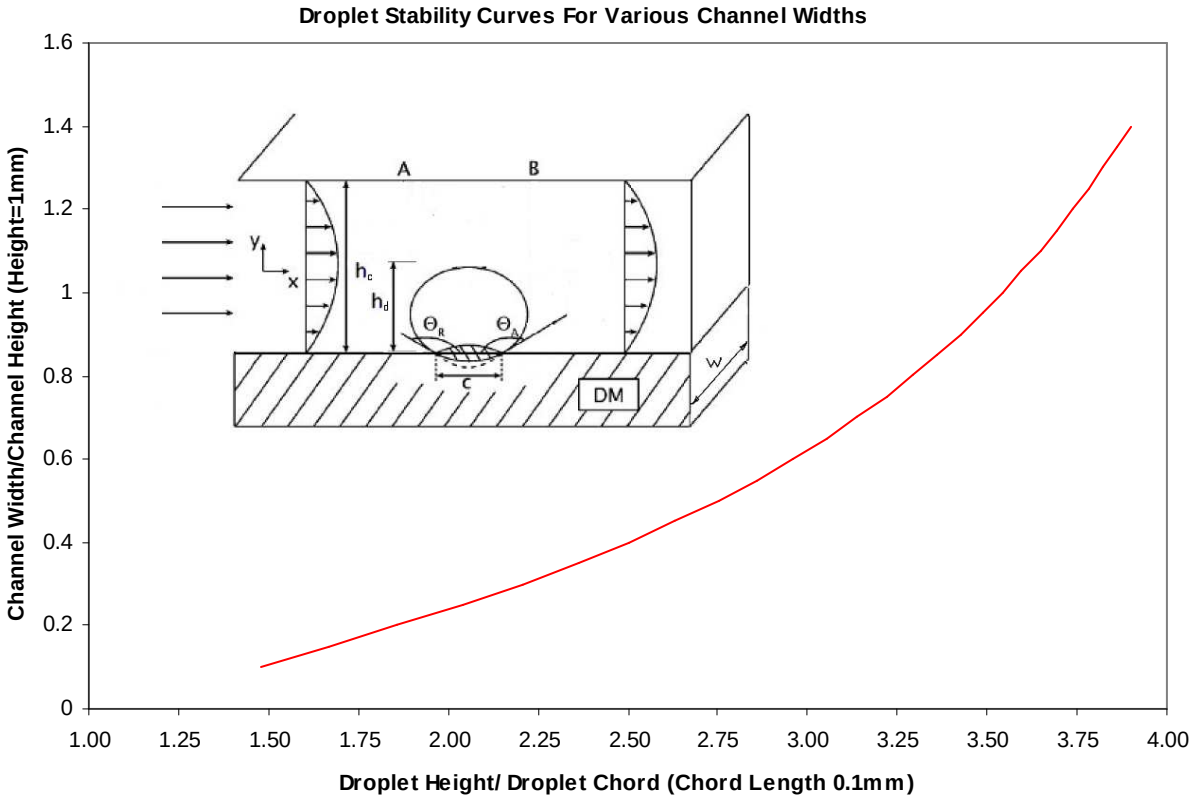

Figure 7: Effects of modifying the channel width

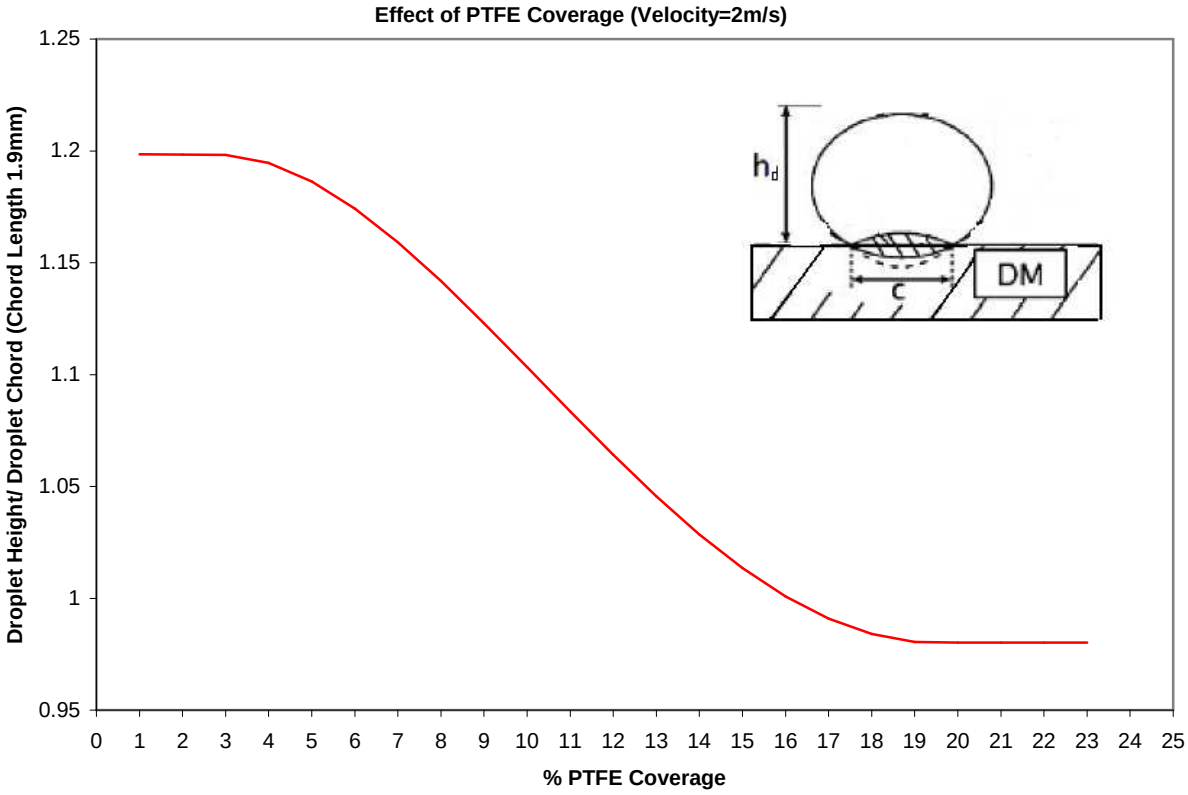

Figure 8: Effects of PTFE Coverage

Table 1: Error Estimates for 5% PTFE Content

RE	Experimental	Model H/C	Error	Kumbur Model H/C	Error
95	1.159	1.101	-5.2%	1.1642	0.4%
194	1.111	1.049	-5.8%	1.1107	0.0%
293	1.104	1.015	-8.8%	1.0798	-2.3%
392	1.069	0.988	-8.2%	1.0581	-1.1%
495	1.052	0.966	-8.9%	1.0419	-1.0%
594	1.003	0.949	-5.7%	1.029	2.5%
693	0.954	0.933	-2.2%	1.0187	6.4%
797	0.973	0.919	-5.9%	1.0095	3.6%
896	0.931	0.907	-2.6%	1.0024	7.2%
995	0.911	0.896	-1.7%	0.9962	8.5%
1197	0.849	0.877	3.1%	0.9854	13.8%

Table 2: Error Estimates for 20% PTFE Content

RE	Experimental	Model H/C	Error	Kumbur Model H/C	Error
107	1.146	1.184	3.3%	1.201	4.6%
209	1.163	1.133	-2.6%	1.149	-1.2%
307	1.125	1.100	-2.3%	1.132	0.6%
409	1.128	1.073	-5.2%	1.103	-2.3%
511	1.105	1.050	-5.2%	1.101	-0.4%
613	1.068	1.032	-3.5%	1.086	1.6%
716	1.051	1.015	-3.5%	1.078	2.5%
818	0.997	1.001	0.4%	1.072	7.0%
920	1.045	0.988	-5.7%	1.063	1.7%
1022	0.981	0.976	-0.4%	1.0592	7.4%
1236	0.963	0.955	-0.8%	1.0561	8.8%